4957-8-F FINAL REPORT

February 1, 1963 to February 1, 1964

DERIVATION OF AEROSPACE ANTENNA COUPLING-FACTOR INTERFERENCE PREDICTION TECHNIQUES

by

P. J. Khan
W. R. DeHart
R. M. Kalafus
A. I. Simanyi
R. B. Harris
W. S. Heath
D. M. Oliver

Approved by JAM Lyon by BHB

John A. M. Lyon

for

COOLEY ELECTRONICS LABORATORY
Department of Electrical Engineering
The University of Michigan
Ann Arbor

Contract No. AF 33(657)-8178
Air Force Systems Command
Aeronautical Systems Division
Wright-Patterson Air Force Base, Ohio

April 1964

TABLE OF CONTENTS

LIST OF TABLES

LIST OF ILLUSTRATIONS

LIST OF ILLUSTRATIONS (Cont.)

ABSTRACT

This final report describes the results of extensive analysis and measurement of antenna coupling factors. The purpose of these studies is to supply information essential to the adequate prediction of the interference between one electronic communication system and one or more other electronic communication systems. All antennas involved in these studies, with two exceptions, are flush mounted antennas such as would often be utilized on aerospace vehicles of either manned or unmanned types. One exception is the study of the quarter wave monopole erected perpendicularly to a common grounding surface. The coupling of a given type of antenna to a quarter wave monopole supplies all of the information necessary to give the power coupling from one antenna to another antenna of the same type. In this way information was obtained for spiral-to-spiral coupling. This information can also be used to obtain the coupling between two antennas of unlike types. The flexibility of this general approach is worthwhile in the consideration of the many combinations possible. The second nonflush mounted antenna type studied has been the dielectric rod. These studies are discussed later.

The report is divided into several sections according to types of antennas. In some of these sections intensive analysis is given as well as experimental data. In other sections the coverage is limited to analysis. The most complete coverage is given to the coupling from one rectangular slot to another. This coverage includes slots arranged in a cylindrical or spherical surface. The rectangular slot studies are representative of resonant antenna coupling.

Additional extended coverage is given to the coupling of one Archimedean spiral to another. The Archimedean spiral is considered to be a good example of a traveling wave antenna widely used for aero-space vehicles.

An analysis is given for the square spiral based upon the premises of a uniform phase constant and stepped attenuation. These assumptions are confirmed experimentally.

In the selection of examples for power coupling, both resonant and traveling wave antennas are used. It is interesting to note that these antennas yield different types of polarization. In the case of the resonant slot, linear polarization is involved. In the case of either the circular or square Archimedean spiral, circular polarization is involved. It is apparent that an idealized Archimedean spiral is not available. Two spirals, presumably of identical manufacture do not have the same radiation properties. During the course of the work on the Archimedean spirals, attempts were made to remove the causes of any observed anomalies. This has not always been possible to do. Of course, a pure axial mode is often desired from a circular Archimedean spiral; however, there is always some contribution from a second mode. Also, reflections and feed radiation cause additional contributions making the antenna depart from a pure traveling wave structure.

A theoretical analysis is presented for horn antennas. The influence of the distribution of effective aperture current is described by a series of curves. The radiation characteristics of horns in a ground plane are similar to those of horns in free space, and use a comparable analytical approach. Further extensions of the coupling studies described in this report would most certainly include experimental work on the coupling of rectangular horns as well as analytical and experimental work on circular horns.

The coupling between two dielectric cylindrical rod radiating elements is ascertained by simplified analysis yielding consistent results for spacings as close as two free space wavelengths for radiators two wavelengths long and six wavelengths long. No experimental confirmation has been attempted. The analytical approach can be used for a variety of other cases. Extension of the dielectric rod studies is not contemplated at present.

1. ASPECTS OF COUPLING AND INTERFERENCE

The antennas of a system play a key role in radio-frequency interference (RFI). Interference may come from within a system, between systems, or from distant transmitters. Even though design frequencies of neighboring antennas are spread apart, the proximity may cause interference from well down on the pass-band of a device. Harmonics and spurious oscillations may also cause interference. A great deal can be accomplished by filters, once the system configuration and specifications are known. An awareness of the behavior of antennas can give the system designer an added powerful tool for reducing RFI. By the proper choice of the antenna type, orientation, and location in a system, many cases of RFI can be avoided. Unfortunately, the detailed information necessary is not usually available due to the volume of data needed, and the variance among antennas which are supposedly identical. Also, since antenna radiation is greatly affected by its environment, laboratory patterns can be misleading.

In order to describe the situation adequately, the following data should be available:

1. Radiation patterns, system power levels, and polarization information for the transmitting and receiving antennas over an appreciable frequency band, including harmonics.
2. VSWR and efficiency of all antennas over a wide frequency range.
3. Effects of reflections and skin curvature on the behavior of these antennas.
4. Propagation path perturbations.
5. Instantaneous pass-band of receiver circuits, as well as nonlinearities.
6. Harmonic power levels of transmitters.

Most of the attention of this contract has centered on the first considerations. The second is less critical and is usually provided by the manufacturer, or can be adequately estimated. Some attention has been given to curvature effects, since they occur frequently in aerospace applications. Reflections are properly a scattering problem and in many cases

can be estimated using scattering cross-section information for simple geometries. The last three are beyond the scope of this project but are fundamental to the RFI problem, and are listed for completeness.

Some attempts at computer simulation of the problem have been attempted (for example, see Ref. 1), but all are hampered by lack of data. This contract has attempted to give useful information on a few important antenna types, which may prove helpful for estimating coupling for other antennas in these classes. First, some simple models are described, and their use on some practical antennas is demonstrated. A more technical and detailed analysis is then given for several low-to-medium gain types, along with considerable experimental data.

2. SIMPLE MODELS FOR COUPLING OF LOW-GAIN ANTENNAS

Interference between neighboring antennas generally takes place through the sidelobes, and is thus sensitive to changes in frequency and environment. It is often useful to use approximate models for a given antenna, especially when detailed information on the pattern is not known over an appreciable band. To facilitate such estimates, several models are worked out which may be useful to a system designer. Two distinct situations arise: Interference between antennas in the common (convex) skin, such as the fuselage of an airplane, and between isolated antennas. A helpful viewpoint is to consider the major propagation path: If it follows a surface, then the first case applies; if not, the second. Thus the coupling between an antenna in the tail of an airplane and one in a wing, for example, would fall in the second category.

2.1 First Case--Common Ground Plane

The far-field coupling between two antennas on a common conducting ground plane may be calculated as follows:

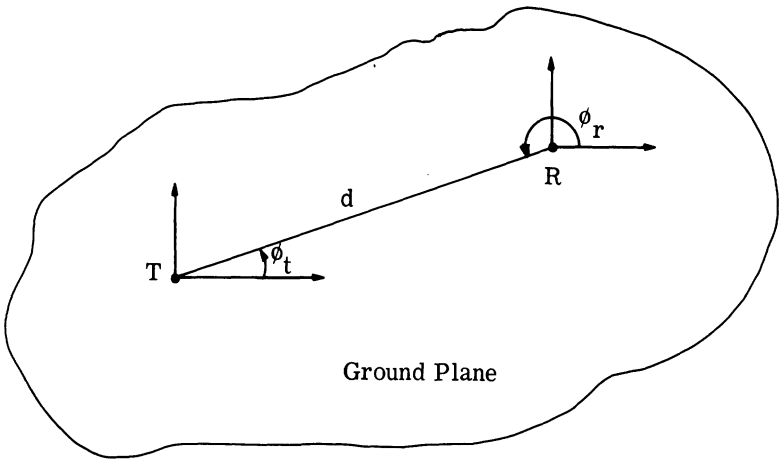

Fig. 1. Coupling geometry for antennas in a common ground plane.

Referring to Fig. 1, it can be seen that the expression for power density at R due to the transmitting antenna T is given by

$$P(d, \phi_t) = \frac{W_t}{4\pi d^2} D_t(\phi_t) \tag{2.1}$$

where

W_t = input power to antenna

d = radial distance from transmitting to receiving antenna

$D_t(\phi_t)$ = normalized pattern factor of the antenna and is given by

$$D_t(\phi_t) = \frac{|\bar{E}(\phi_t)|^2}{\frac{1}{4\pi} \int_0^{2\pi} \int_0^{\pi/2} |\bar{E}(\theta_t', \phi_t')|^2 \sin \theta_t' \, d\theta_t' \, d\phi_t'}$$

where

$\bar{E}$ = electric field in the radiating half-space.

When losses are ignored, the power received at the receiving antenna R is

$$W_r = P(d, \phi_t) \; A_r(\phi_r)$$

$$= \frac{W_t \, D_r(\phi_r) \, D_t(\phi_t)}{64\pi^2 (d/\lambda)^2} \tag{2.2}$$

where

$A_r(\phi_r)$ = aperture of receiving antenna

$D_r(\phi_r)$ = normalized pattern factor, defined like $D_t(\phi_t)$.

The coupling between antennas is the ratio of power received to power transmitted

$$C = \frac{W_r}{W_t} = \frac{D_r(\phi_r) \, D_t(\phi_t)}{64\pi^2 (d/\lambda)^2} \tag{2.3}$$

The factor 64 is used where all energy is confined to geometric half-space as for two flush mounted antennas in a common ground plane. Alternatively, the D factors could have been redefined. The factor 16 is used for two antennas wholly in free space.

The effect of losses in the antennas is considered by multiplying the coupling C

by the appropriate efficiency factors α_r and α_t, where $0 < \alpha \leq 1$. The coupling is related to mutual impedance by (see Appendix A)

$$C = \frac{|Z_{12}|^2}{4 R_{11} R_{22}} \tag{2.4}$$

where

Z_{12} = mutual impedance

R_{11} = real part of input impedance to transmitter

R_{22} = real part of input impedance to receiver.

This formula also applies in the near-field and in free space.

For low-gain antennas, the far-field approximations apply for spacings as close as one wavelength. The relative alignment is automatically taken into account by the ground plane patterns, since the presence of the skin dictates a negligible tangential electric field; only a vertical electric field is involved.

In general, the skin of aerospace vehicles has appreciable curvature, so that coupling takes place via the surface wave along the skin. The effect of curvature of the skin can be readily calculated for a great number of cases (see Section 5).

2.2 Coupling Between Idealized Antenna Models--Common Surface

Several models are considered:

1. Semi-isotropic (isotropic above the plane, zero below) -- [$D(\phi) = 2$ (3 db)]
2. Short monopole -- [$D(\phi) = 3.0$ (4.76 db)]
3. Thin quarter-wave monopole -- [$D(\phi) = 3.28$ (5.15 db)]
4. An antenna circularly polarized on the $\theta = 0$ axis, such that $E_\phi/E_\theta = \cos\theta$, and $E_\theta(\theta, \phi) = 1$ -- [$D(\phi) = 0.37$ (-4.35 db)] .

Coupling as a function of center-to-center spacing is shown in Fig. 2 for several transmitter-receiver combinations. Monopoles show higher coupling than semi-isotropic antennas; the circularly-polarized antenna coupling is lower due to the energy involved in the ϕ-component. Coupling may be obtained for any antennas in a common ground plane by considering the coupling between two semi-isotropic antennas. If this quantity is called C_s, the coupling between antennas T and R is given by

$$C = \frac{1}{4} C_s \, D_t(\phi_t) \, D_r(\phi_r)$$

where

$$C_s = \frac{1}{(4\pi \, d/\lambda)^2}$$

The usefulness of this treatment is now evident. The coupling between two antennas on a ground plane can be found by considering the lower curve of Fig. 2, and multiplying the value obtained there by the appropriate pattern factors of the two antennas. Actually, efficiency and VSWR should be considered as well.

Slots can be treated from these curves. A comparison of a short, thin slot with a short monopole shows that the coupling must be the same for slots broadside-to-broadside. To extend this to other orientations, it is necessary only to consider the relative orientations; thus with reference to Fig. 3,

$$C_{slots} = C_{monopoles} \cos^2 \phi_t \cos^2 \phi_r \quad .$$

This applies as well to thin resonant slots, where the curve for quarter-wave monopoles is used. The error involved in using this form with resonant slots having length-to-width ratios of only 2 to 1 (therefore, not thin) is less than 1.1 db per antenna. This breaks down at the null of the far-field pattern. Slots are treated in more detail in Section 3.1 of this report.

The fourth model listed above is useful for radiators that are circularly polarized along the $\theta = 0$ axis (out in front), such as spirals. The skin dictates that the tangential E field be zero along the ground plane, and thus that the wave there is linearly polarized.

This cross-polarized model can be extended to more highly-directional cases by considering θ-variations of the field of the form $\cos(\alpha \sin \theta)$, as would be the case in a two-dipole array. This is similar in form to the spiral antenna, and can be used for approximating it. Assuming ϕ-symmetry let S be defined by

$$S = \frac{E_\theta(\pi/2)}{E_\theta(0)}$$

i.e., the ratio of ground-plane E-field to axial E-field. Also, let E_ϕ be related to E_θ by

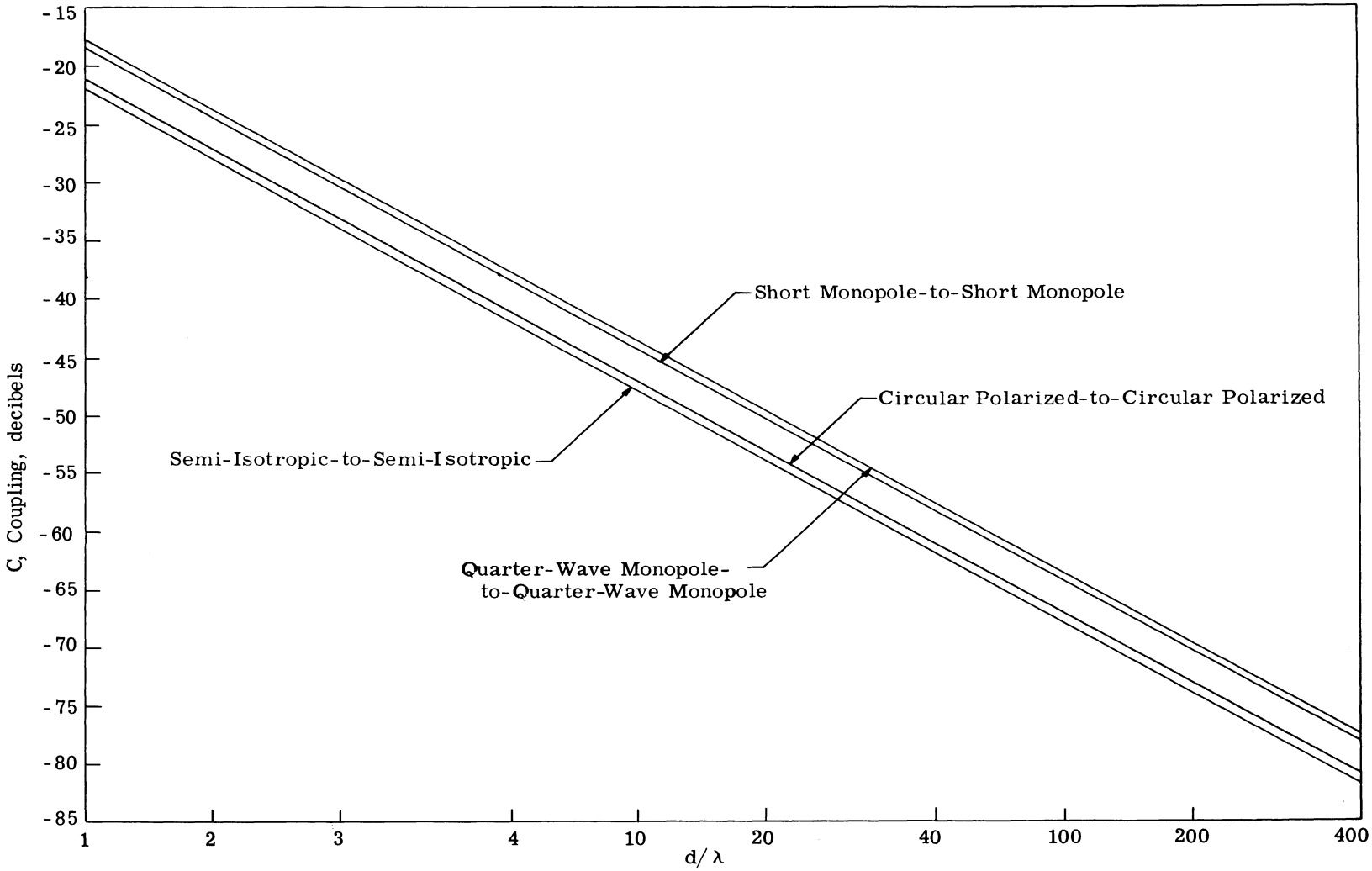

Fig. 2. Coupling vs. spacing for some ideal antennas on a ground plane.

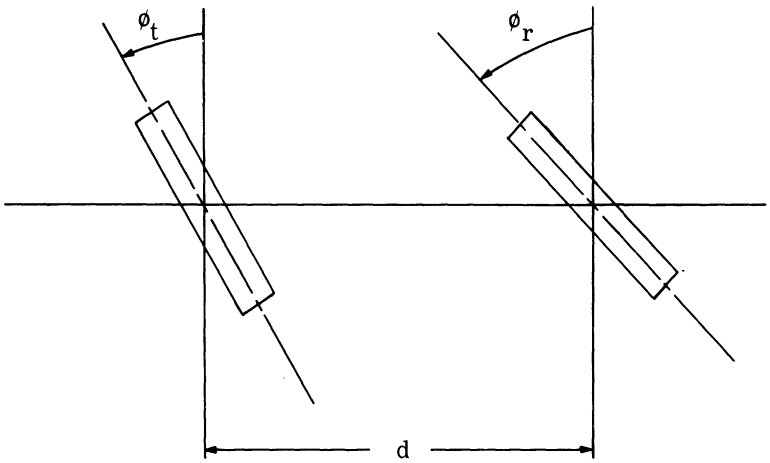

Fig. 3. Coupling geometry for two thin, short slots.

$$E_\phi = E_\theta \cos\theta .$$

Figure 4 shows a set of curves for several values of S expressed in decibels. These curves represent the coupling vs. spacing between such a cross-polarized antenna and a quarter-wave monopole. Fresnel-zone effects are ignored, which is adequate for low-gain antennas.

2.3 Second Case: No Common Surface

In the case where coupling takes place via a ray not bound to a surface, the usual formulas apply. The far-field coupling between two antennas is given by

$$C = \frac{D_r(\theta_r, \phi_r)\, D_t(\theta_t, \phi_t)\, A(T,R)}{16\pi^2 (d/\lambda)^2}$$

where the normalized pattern factor D is given by

$$D(\theta,\phi) = \frac{|\bar{E}(\theta,\phi)|^2}{\frac{1}{4\pi}\int_0^{2\pi}\int_0^{\pi} |\bar{E}(\theta',\phi')|^2 \sin\theta'\, d\theta'\, d\phi'}$$

and

A = alignment factor, depending on the relative polarization.

Table I below is given for convenience. Elliptical polarization effects can be estimated from this table. The low values, such as -25 db, are not to be considered exact but indicative.

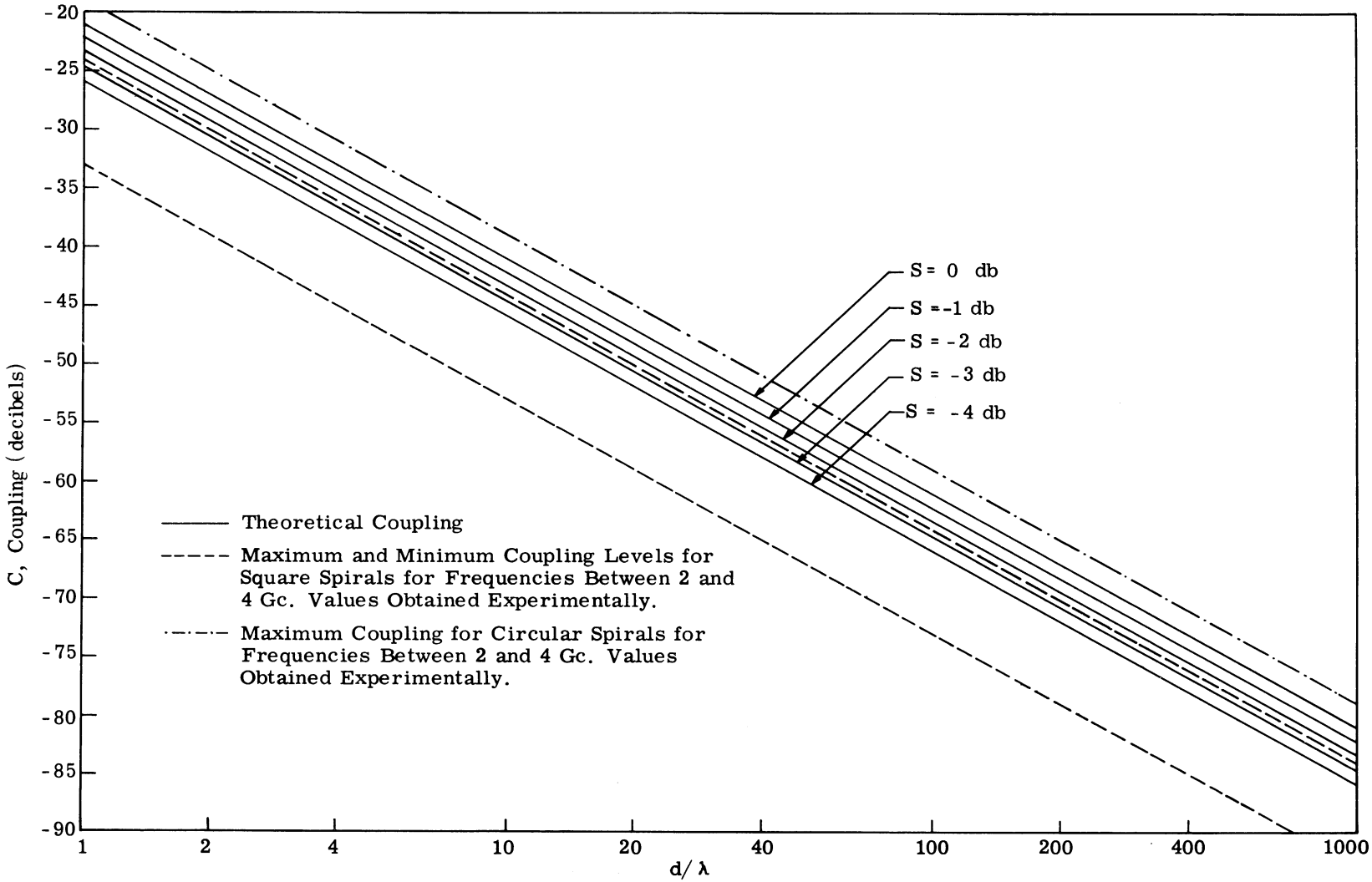

Fig. 4. Coupling vs. spacing for a set of ideal circular-polarized radiators.

Antenna Alignment Factors

Polarization	Horizontal	Vertical	Diagonal	Circular RH	Circular LH
Horizontal	0 (db)	-25	-3	- 3	- 3
Vertical	-25	0	-3	- 3	- 3
Diagonal	- 3	- 3	-3	- 3	- 3
Circular RH	- 3	- 3	-3	0	-25
Circular LH	- 3	- 3	-3	-25	0

Table I

The coupling between two "parallel" isotropic antennas is

$$C_i = \frac{1}{(4\pi\, d/\lambda)^2} \cdot$$

The pattern factor D is defined relative to isotropic, so that

$$C = C_i\, D_t(\theta_t, \phi_t)\, D_r(\theta_r, \phi_r)\, A(T,R)$$

as before. In fact, the same figure (Fig. 2) may be used, if "isotropic" is substituted for "semi-isotropic," and "dipole" for "monopole".

3. DETAILED STUDIES AND EXPERIMENTAL RESULTS

3.1 Coupling Between Rectangular Slots

3.1.1 Introduction. From the simple models of Section 2, the coupling between two broadside slots would be approximately that between two quarter-wave monopoles. For configurations other than broadside, these results must be modified by the gain factors of each slot. With ϕ_r and ϕ_t defined in Fig. 3, the gain factors $G_t(a, b, \phi_t)$ and $G_r(a, b, \phi_r)$ are expressed by:

$$G(a, b, \phi) = \frac{\cos\left(\frac{ka}{2}\cos\phi\right)\sin\left(\frac{kb}{2}\sin\phi\right)}{\left[1-\left(\frac{ka}{\pi}\cos\phi\right)^2\right]\sin\left(\frac{kb}{2}\right)} \qquad (3.1)$$

The far-field coupling formula from Section 2.3 is then:

$$C(db) = -17.7\ db + 20\log_{10} G_t + 20\log_{10} G_r - 20\log_{10}(d/\lambda)\ . \qquad (3.2)$$

Experimentally, a more accurate expression is:

$$C(db) = -19.7\ db + 20\log_{10} G_t + 20\log_{10} G_r - 20\log_{10}(d/\lambda)$$

which differs from Eq. 3.2 by 2.0 db. The discrepancy is primarily due to the approximation to a thin slot. The more accurate formulation of Section 3.1 gives close agreement with experiment. This formula satisfactorily predicts coupling even for moderately close spacings. In the present report a formulation is given which considers near-field terms and yields useful improvement at close spacings. The far-field expression is entirely inadequate, however, for predicting the coupling between slots where one or both lies on the axis of the other. Some interesting results are presented here for this case.

3.1.2 Discussion of Near-Field Formulation and Comparison with Experimental Results. The transmitting slot sets up a field in space which gives rise to a tangential magnetic field $\bar{H}_o$ on the ground plane. When a second slot is cut, the displacement current

thus induced will produce a tangential field $\bar{E}$ in the receiving aperture. However, the field $\bar{E}$ must be consistent with the receiving waveguide boundary conditions as well as with $\bar{H}_o$. It is reasonable to assume a principal mode distribution in the aperture. The received power is then proportional to the Fourier coefficient of $\bar{H}_o$,

$$W_R \sim \left| \int\int H_o \cos \frac{\pi y}{b} \, dy \, dx \right|^2$$

By also assuming a dominant mode configuration in the transmitting guide, one can calculate $\bar{H}_o$. Upon substitution of this $\bar{H}_o$ in the above expression for W_R, the coupling can be found without making far-field approximations. The resulting quadruple integral can be reduced to a double integral for computer evaluation. The mathematical calculations are outlined in Appendix B. The coupling magnitude for the broadside-to-broadside case is given by:

$$C = \frac{ka}{4\pi^2} \left(\frac{a}{b}\right) \frac{1}{(-\delta_1)\sqrt{1 - \frac{\pi^2}{k^2a^2}}} \left[\int_{\frac{\pi(d-b)}{a}}^{\frac{\pi(d+b)}{a}} du \left[\frac{\pi b}{a} - \left| u - \frac{\pi d}{a} \right| \right] \right.$$

$$\left. \int_0^{\pi} \left\{ \left[1 - \frac{\pi^2}{k^2a^2} \right] (\pi - v) \cos v + \left[1 + \frac{\pi^2}{k^2a^2} \right] \sin v \right. \right.$$

$$\left. \left. \frac{\exp\left[-j \frac{ka}{\pi} \sqrt{u^2 + v^2} \right]}{\sqrt{u^2 + v^2}} \right\} dv \right]^2 \qquad (3.3)$$

and a, b, and d are defined in Fig. 3. The coupling falls away from the simple 1/d behavior in the manner shown in Fig. 5. Theoretical and experimental results show close agreement. The coupling is changed merely by the pattern factors of the slots as one or both is rotated, at least until a null is reached on one of the two patterns (see Fig. 6).

When one antenna lies along the axis of the other (i.e., on a pattern null), the far-field terms vanish, and the coupling falls off as $1/d^2$ instead of 1/d. Figure 2 shows this trend even up to close spacings, for slots placed end-to-end. Interesting behavior is exhibited when one slot is rotated away from the end-to-end configuration. Rather than increasing,

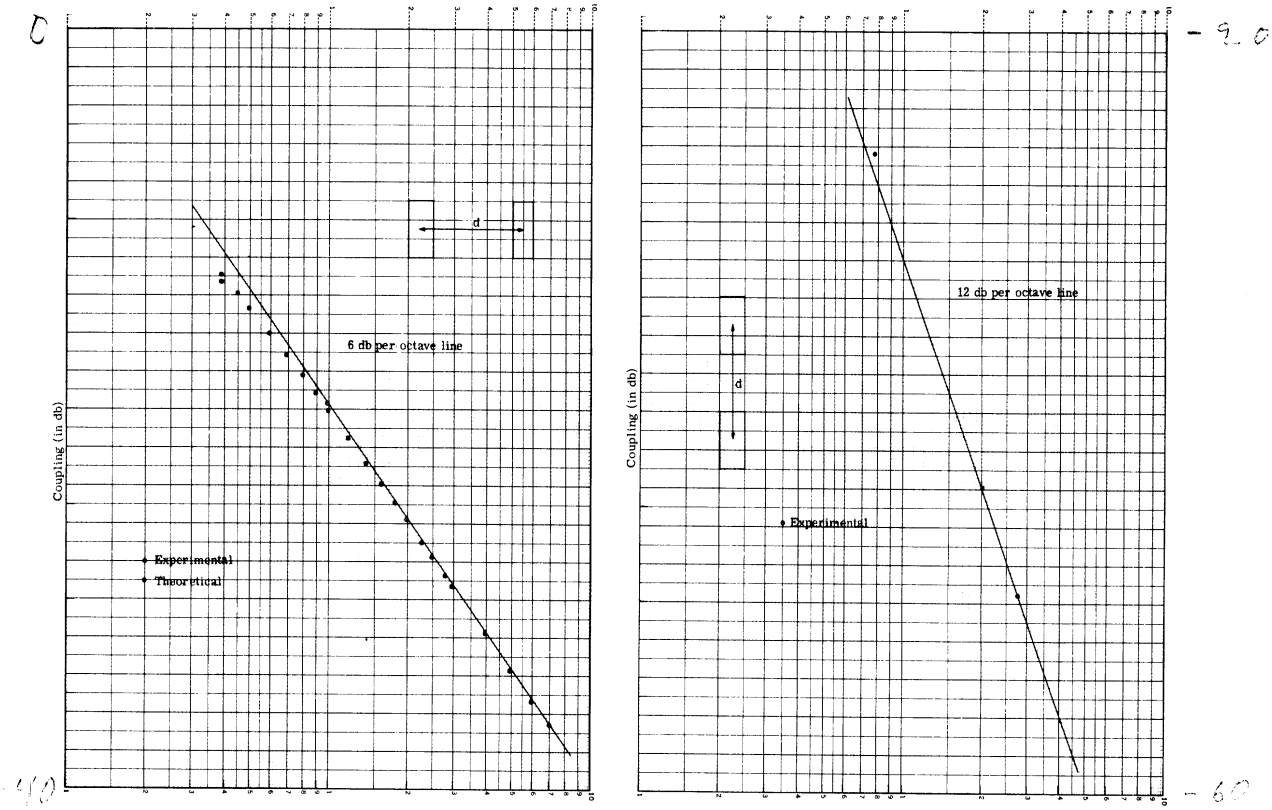

5(a). Broadside

5(b). End-to-end

Fig. 5. Coupling vs. spacing for two slots

the coupling decreases since the far-field has an H-field in the ϕ-direction except along the axis, so that a slot oriented with its length parallel to the transmitted H-field has the strongest TE_{10} excitation. When it is perpendicular, the slot has no H-field along its length. The transmitting field attempts to set up a mode with its E-field across the length of the slot. On the other hand, in the end-to-end configuration the H-field, while belonging to the near-field, is still in the proper direction to excite the TE_{10} mode. The coupling at the end-to-broadside configuration is below the range of the apparatus, i.e., more than -90 db.

3.2 Spiral Antennas

3.2.1 Introduction and Summary of Spiral Properties. The widespread use of flush broadband antennas on aircraft and missiles, both singly and in arrays, has motivated a detailed study of the ground plane fields. The Archimedean spiral is representative of this class, and was thus chosen for further study. It provides a practical way of producing circularly polarized radiation over a wide band of frequencies. It is usually mounted in a

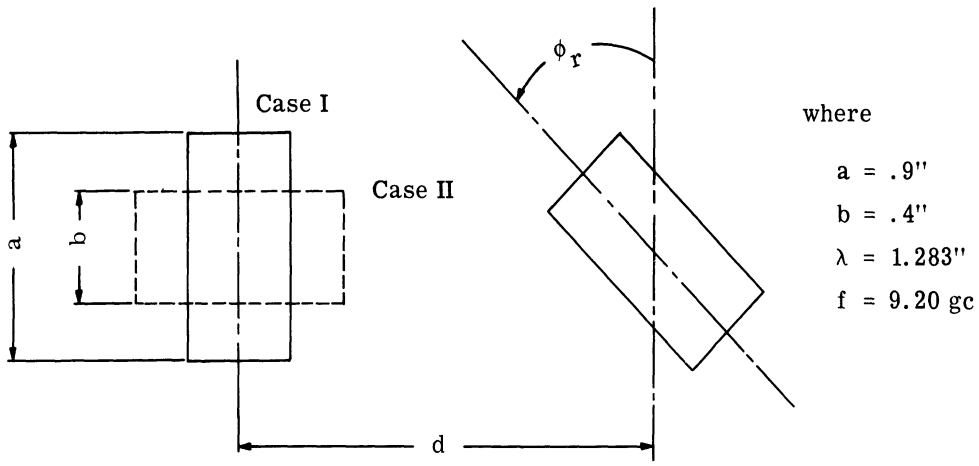

(a) Geometry

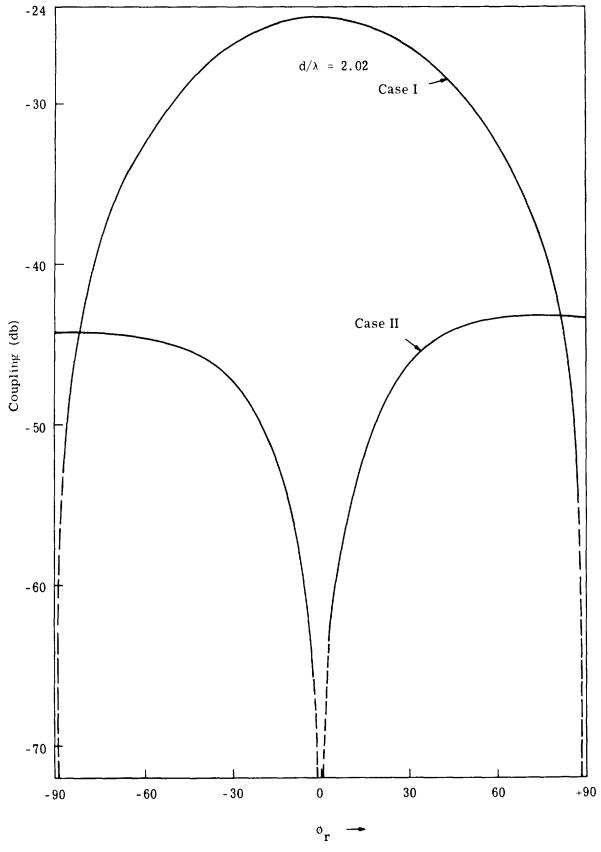

(b) Curve

Fig. 6. Coupling vs. orientation angle of two slots

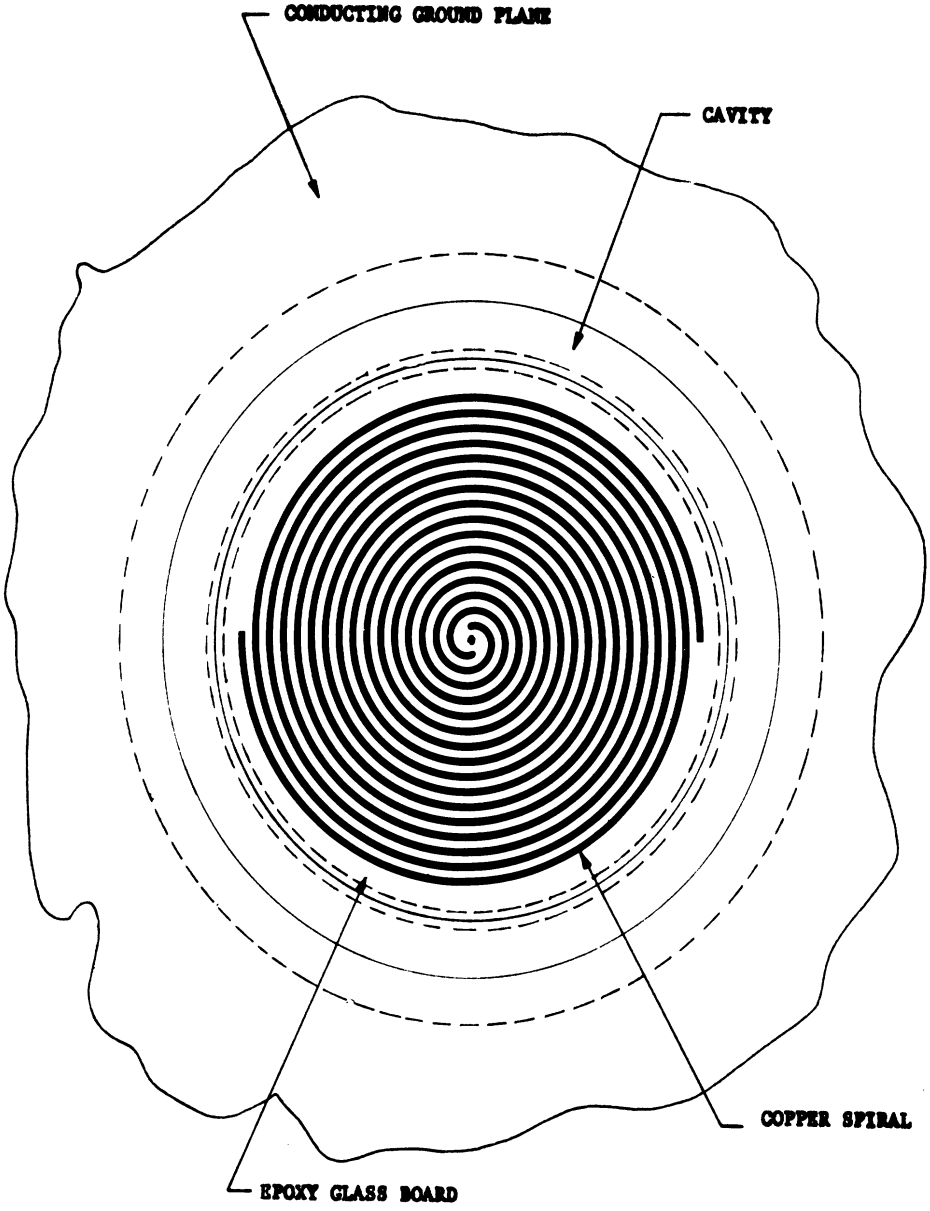

Fig. 7. Spiral face configuration.

conducting ground plane and backed by a cavity.

The square and circular spiral configurations are the most common types. Figure 7 indicates a circular spiral assembly in a ground plane. The square spiral configuration may be seen in Fig. 41(a) of Appendix C. These spirals may be wound either clockwise or counterclockwise depending on the sense of circular polarization desired. Spiral antennas are usually fed out of phase, in order to effect maximum radiation out in front. A balun is used to provide a balanced feed.

The operation of the spiral antenna has been explained qualitatively in a number of papers.[2,3,4] A mathematical approach to the circular Archimedean spiral has been presented by W. L. Curtis.[4] The square spiral is analyzed mathematically in Section 4 of this report. A summary of the operation of the spiral antenna is given here.

As shown in Fig. 7, the antenna can be thought of as a two-wire transmission line which has been wrapped around the origin in such a way as to form a spiral. It is obvious that at any position along this line, the wire lengths differ. Furthermore, this difference in lengths steadily increases for points further removed from the origin. If two out-of-phase waves of current start at the center terminals and travel out along the transmission line, they will eventually become in phase when the difference in the lengths of the line wires becomes $\frac{\lambda}{2}$. It may be shown that the distance from the origin at which this in-phase condition occurs is given approximately by $r = \frac{\lambda}{2\pi} = .159\lambda$. This value is the radius of a ring one wavelength in circumference.

From considerations of this kind, it is generally assumed that most of the radiation from the spiral originates in a region near the one wavelength ring where neighboring current elements have small phase differences. For other regions of the antenna the fields tend to cancel. It is also reasonable to assume that the currents are attenuated in the region of the radiation ring due to radiation damping. If the ring is not too near the outer extremities of the antenna, the current magnitude may be reduced enough so that reflections from the ends of the spiral arms can be neglected.

In a rough way, one can approximate a spiral at one frequency by a similarly shaped loop which carries a traveling wave. Thus, for a circular spiral, consider a circular loop with a circumference of one wavelength. The separation of parallel elements is the diameter $d = \lambda/\pi = .318\lambda$. For a square spiral, this distance is $d = \lambda/4 = .25\lambda$.

This suggests a consideration of two parallel and equal current elements separated by a distance d (see Fig. 8).

This arrangement can be easily analyzed for the pattern, which is found to be proportional to

$$F(\theta) = \cos\left(\frac{\pi d}{\lambda} \sin\theta\right) . \qquad (3.4)$$

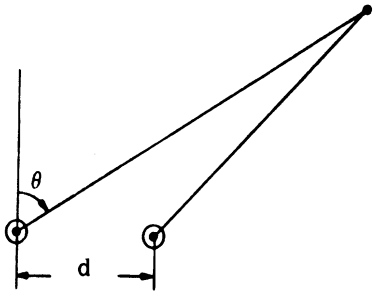

Fig. 8. Two-element array geometry.

Let S(d) be defined by (see also Section 2.3)

$$S(d) = \frac{F(\pi/2)}{F(0)} = \cos \frac{\pi d}{\lambda} . \qquad (3.5)$$

This gives the magnitude of the ground plane radiation relative to the on-axis field of such an antenna. For a circular spiral,

$$S(d) \approx -6 \text{ db} .$$

A comparison of Figs. 9 and 10 show that the above theoretical results are in rough agreement with observed behavior, particularly the difference, 3 db. In general, observed patterns show more gain than predicted by this model due largely to the reflected energy from the cavity, which tends to produce greatest reinforcement along the axis, and to produce less reinforcement near the ground plane.

If dielectric is used extensively near the spiral, e.g., in the cavity, the radiating region will be reduced in size. The effective dielectric constant is not significantly altered until a substantial amount of dielectric is used, in terms of wavelengths. When this occurs, the effective spacing d decreases, which broadens the beam.

Thus the gain of a spiral antenna depends mainly on two factors:

1. The shape of the spiral.
2. The effective dielectric constant surrounding the elements.

A square spiral will have a broader beam than a circular spiral, and thus less gain. Similarly, the effective dielectric constant varies directly with the width of the beam. Thus for maximum gain, a circular spiral should be utilized, using an air-filled cavity, as

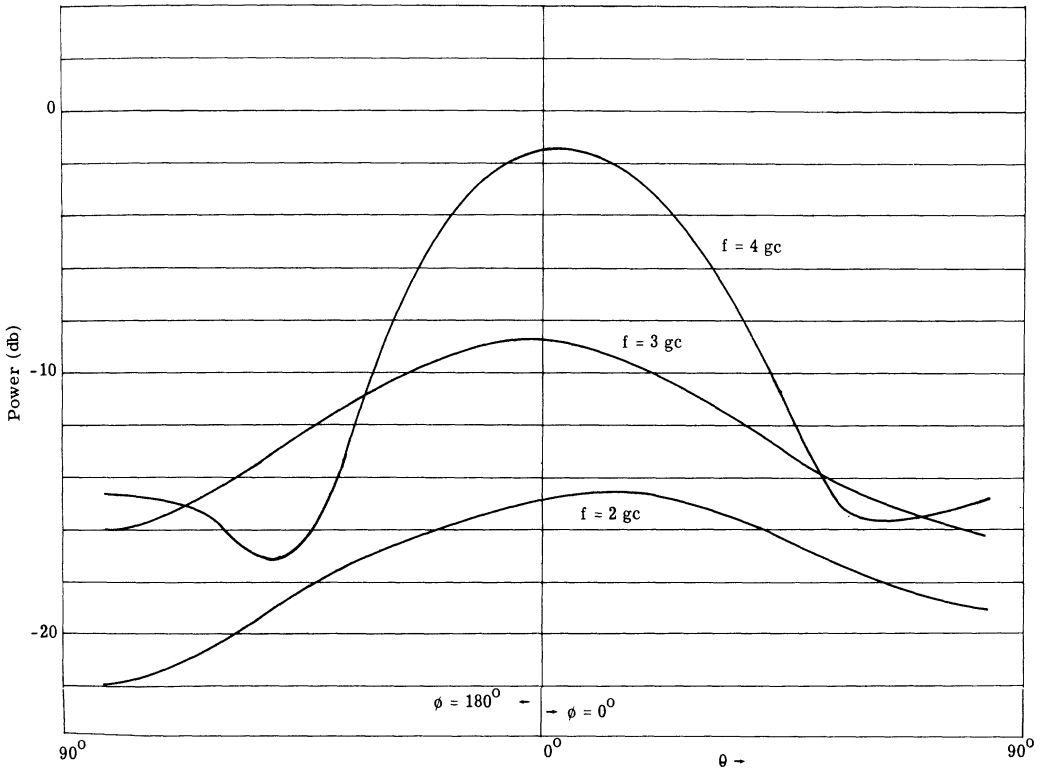

Fig. 9. Radiation patterns for Circular Archimedean Spiral "A".

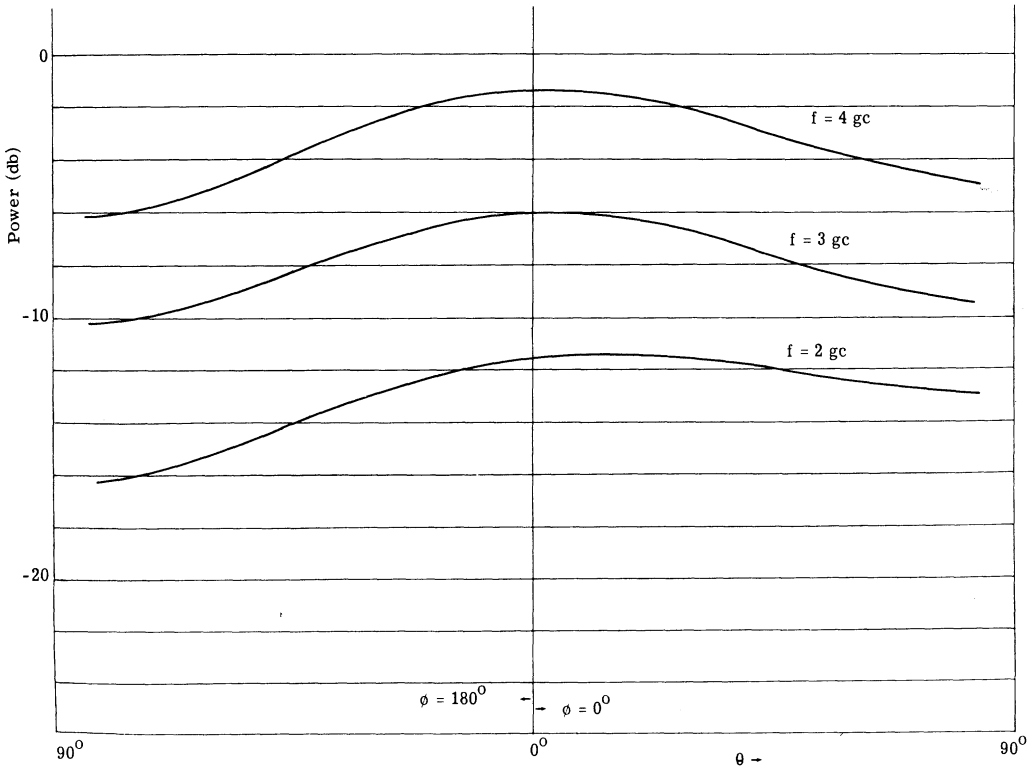

Fig. 10. Radiation patterns for Square Archimedean Spiral "1L".

thin a printed circuit board as possible, and as low a dielectric constant as possible. The above conclusions are borne out by the experimental data and a consideration of the resonant circumference condition.

Interest to date has centered largely around the near-axis, far-field properties, which can be obtained with rather crude approximations to current distribution. However, the interference effects between antennas in a common ground plane depend upon ground plane patterns, which require a more detailed knowledge of current distribution.

An interesting factor of spiral ground plane patterns (see Fig. 11) is their lack of omnidirectionality. However, ϕ-variations are not due to imperfections in spiral construction. Even with a perfectly balanced feed (necessary for the axial mode), and with perfect mechanical symmetry, a coupling variation of several db will occur as the spiral is rotated in the ground plane. With the commercial spirals tested, other effects add to the basic ϕ-variations. These variations stem from the following secondary causes and apply to all antennas in this class:

1. In-phase feed currents and the subsequent redistribution of current on the spiral.
2. Reflections from the ends of the spiral elements.
3. Reflections from the cavity.
4. Distributed, induced reflection by neighboring elements.
5. Direct radiation from the feed and balun.

The effects noted above are more critical in coupling properties than in near-axis properties. While it is difficult to isolate the effects of the several secondary causes, additional information thereon would help in the future design of flush antennas.

Variations in the ground plane coupling pattern are not completely undesirable for they make possible appreciable decoupling by proper orientation. However, the observed ϕ-variations change rapidly with frequency, so decoupling can occur only over a narrow band. For array purposes, it would often be better to have frequency independent ϕ-variations over the band, even at the expense of higher coupling levels.

In the presentation of experimental work which follows, the level of the radiation patterns is not determined, but can be found by relating the end-points ($\theta = 90^{\circ}$) to the coupling data, which are fixed in level. In most coupling patterns, the top line in the pattern is

set at -20 db or, in some cases, at -30 db. The spacing in wavelengths is given with each curve to relate the results to the models discussed earlier and shown in Fig. 4.

3.2.2 Circular Archimedean Spiral. Two similar circular Archimedean spirals obtained from Aero- Geo-Astro Corporation were tested singly and together. Pertinent data follow:

Frequency range:	2 - 4 gc
Number of turns:	13
Width of conductor:	0.62 inches
Width of spacing:	0.62 inches
Balun type:	Roberts, strip-line
Diameter of cavity:	4 inches

In order to test each antenna singly, a quarter-wave monopole probe was used as a transmitter and located 11.3 inches away from the spiral center. A 4 ft. x 4 ft. ground plane using absorbing material all around yielded results within 0.5 db at large couplings (-35 db or higher) and within 2 db at lower levels (-50 db) compared to the values using a 12 ft. x 12 ft. plane in the highly accurate anechoic chamber.

The general problem of coupling between flush antennas in a ground plane is greatly simplified by the fact that the incident field is linearly polarized, since the tangential E-field must be zero at the conductor. This, plus the fact that in the far-field, the field looks like an ordinary plane wave, means the great majority of problems can be solved merely knowing the coupling patterns. The implication that the winding sense of the spiral is irrelevant breaks down in the near-field case because the receiving spiral in a spiral-to-spiral configuration subtends a large enough angle of the other that the phase distribution of the transmitting field over the receiving area is no longer that of a constant-phase plane wave. However, this effect can be noted experimentally by comparing the couplings at large and small spacings.

Figure 11 shows typical coupling patterns between the spiral antenna and a tuned monopole probe. These exhibit sharp nulls near the upper end of the design band for both antennas "A" and "B", due to cavity, balun radiation and second-mode effects. (The second mode is excited by in-phase currents at the feed, and has a null on the axis). Figure 12 shows

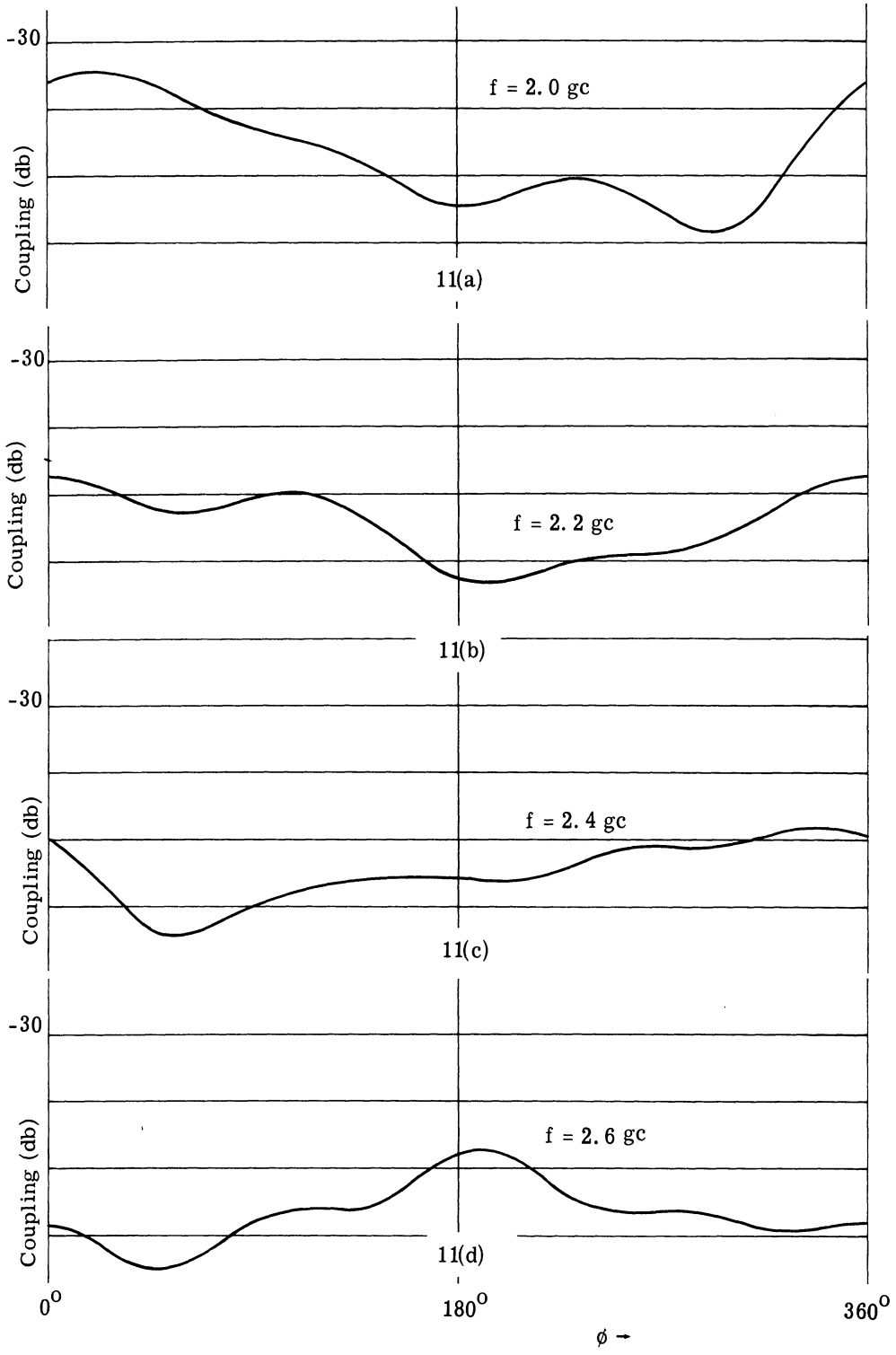

Fig. 11. Coupling patterns for Circular Spiral "A".

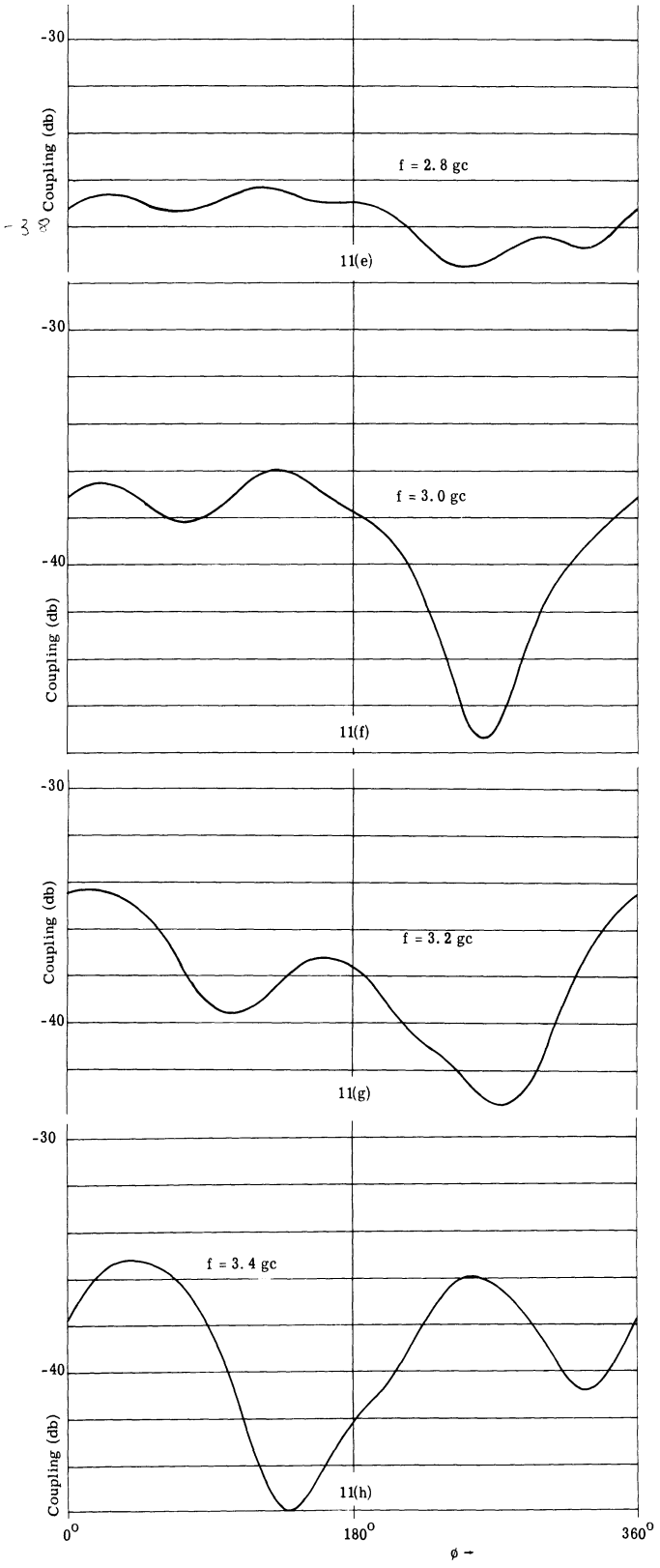

Fig. 11 (Cont.). Coupling patterns for Circular Spiral "A".

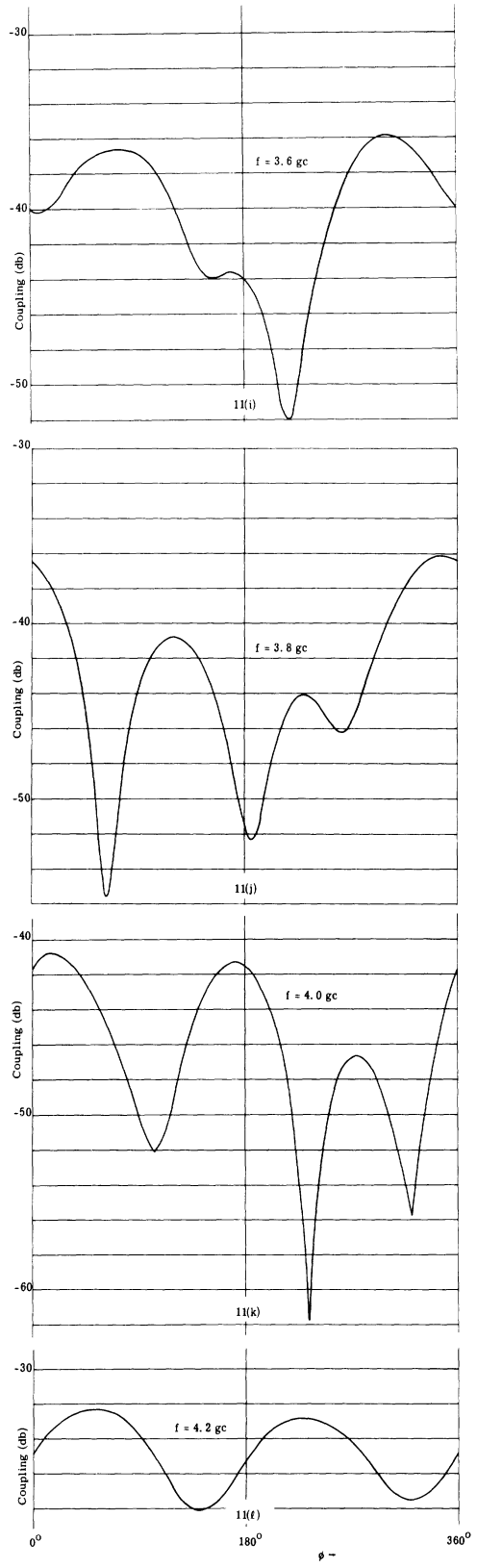

Fig. 11 (Cont.). Coupling patterns for Circular Spiral "A".

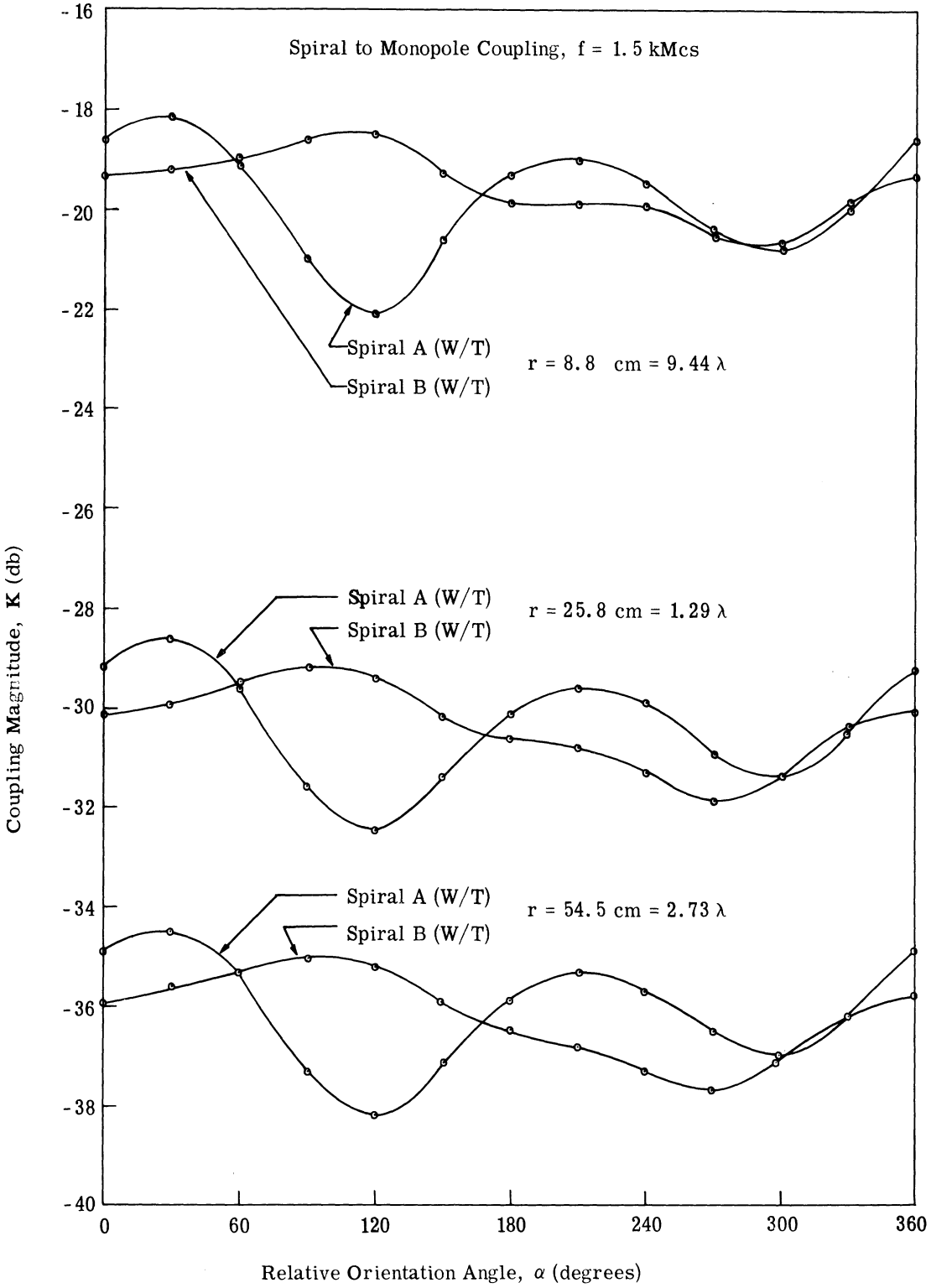

Fig. 12. Coupling patterns at several spacings, center-to-center.

coupling patterns taken at three spacings for two similar circular spirals "A" and "B" at one frequency. At other frequencies the behavior was similar. (These data were taken before the experimental setup allowed continuous coupling patterns.) The patterns are fairly consistent as the spiral-to-monopole spacing is varied even at the extremely close spacings where the probe is 1.5" from the periphery. Even more consistent is the coupling level, which at the pattern maxima follows within 0.5 db of the ordinary 6 db per (distance) octave of frequency variation at distances of 1 wavelength or more. At closer spacings, the level tends to rise somewhat above the 6-db line by up to 1.5 db at 1/2 wavelength (see Fig. 12).

Extensive tests were taken on the coupling patterns, from 1.7 gc to 4.2 gc in 50-Mc increments on spirals "A" and "B". Rather than present all the curves involved, typical patterns are shown in Fig. 11 and reduced data are shown in Figs. 13(a) and 13(b). Figure 16 shows the total variation of coupling as a function of frequency. The actual spacing is held constant so that the electrical spacing, in wavelengths, changes with frequency. For comparison, a uniform coupling curve, inversely proportional to frequency, is also shown.

The coupling decreases noticeably near 4 gc, where simultaneously the radiation pattern is becoming narrower (see Fig. 9). This increase in gain means more power is radiated along the axis, and thus less along the ground plane. The variations are small at lower frequencies and increase to extreme values at the higher frequencies, where sharp nulls occur. Just above the rated frequency band, the coupling increases sharply with small variations. The reason for this is that the second mode, which has a null on the axis of the spiral, becomes predominant. This mode occurs when the feed currents differ appreciably from the out-of-phase condition. There is a large in-phase component when the balun is operated outside its designed band. Furthermore, the second mode has more energy concentrated along the ground plane, which accounts for the rise in the coupling level.

Figure 14 shows the angular position of the maxima as a function of frequency. An expanded angular scale is used for clarity; one should remember that $\phi = \phi + 2n\pi$ in the figures. At the lower end of the band, the maxima and minima shift quite rapidly. This is due to standing waves arising from reflections at the ends of the spiral elements. These standing waves are more predominant at lower frequencies because the current traveling wave is not sufficiently attenuated by radiation damping. The curves of Fig. 14 demonstrate

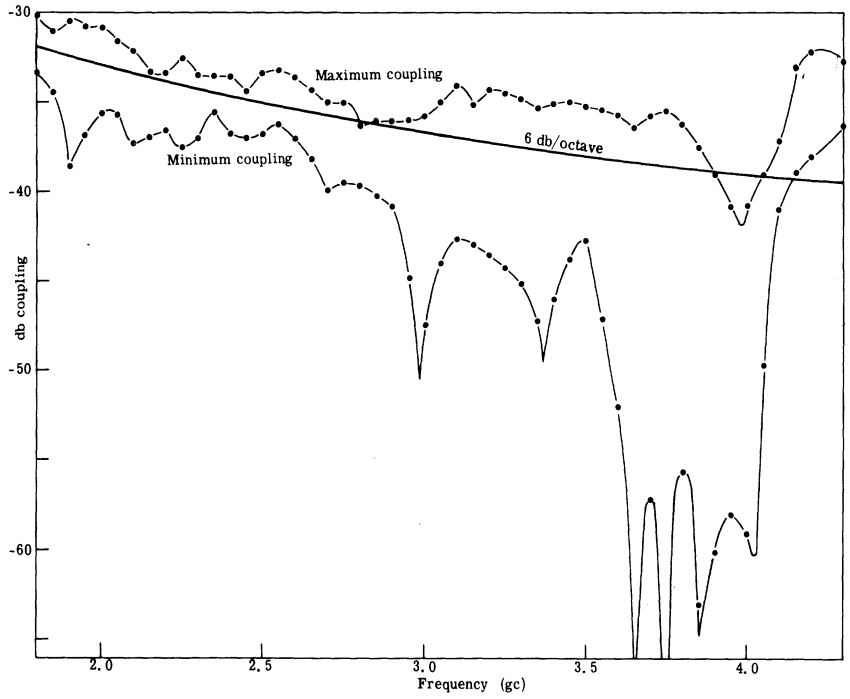

13(a)

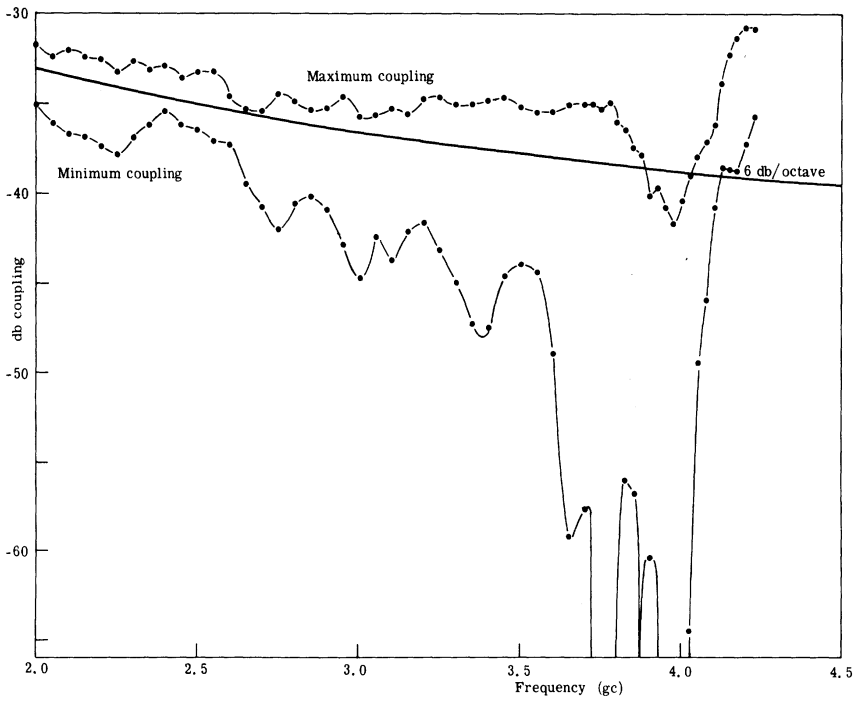

13(b)

Fig. 13. Total variation of coupling vs. frequency (a) for circular spiral "A" (b) for circular spiral "B".

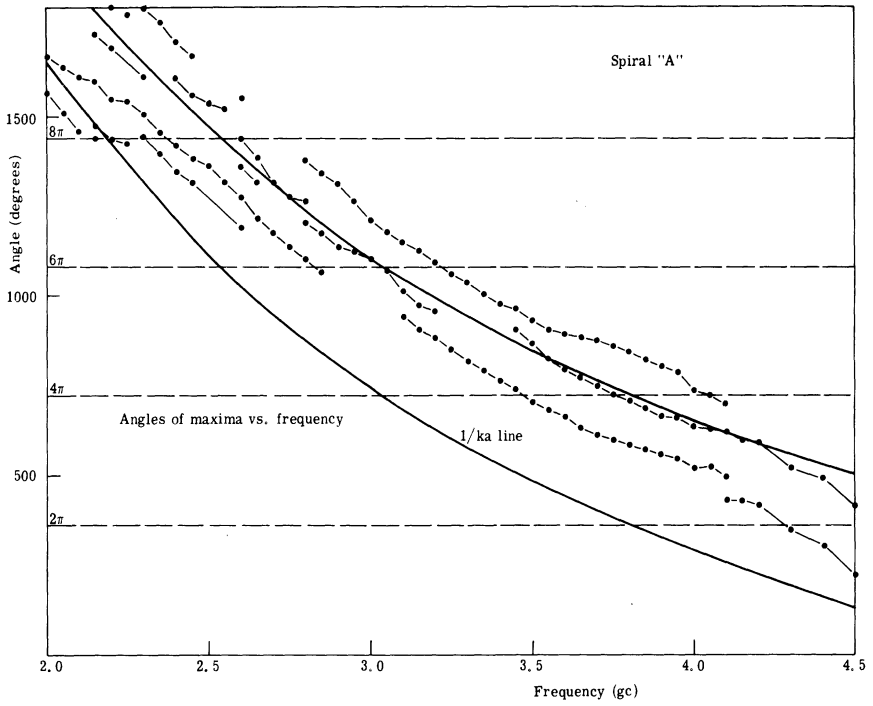

14(a)

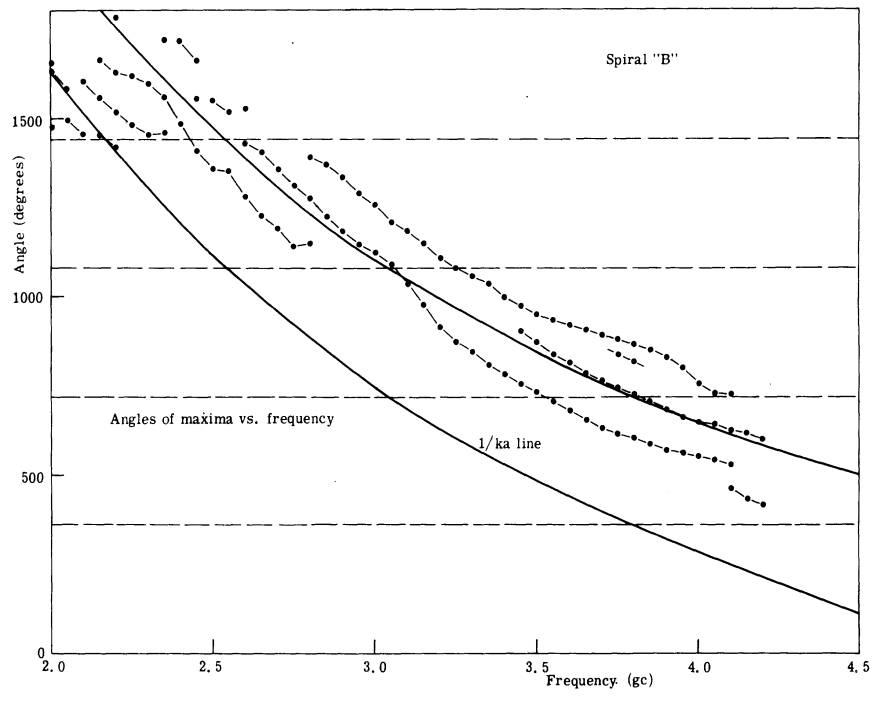

14(b)

Fig. 14. Angles of maxima of coupling vs. frequency, square spiral "IL" (a) for circular spiral "A" (b) for circular spiral "B".

that nulls of the pattern, which move in much the same manner as the maxima, can only be used for decoupling over a narrow frequency band.

3.2.3 Square Archimedean Spiral. Right-hand and left-hand wound square spirals were experimentally tested on the 12 ft. by 12 ft. ground plane in the anechoic chamber. Pertinent data follow:

Type: Cavity-backed, two-arm, twenty turns

Frequency range: 2 - 4 gc

Balun type: strip-line, Roberts, located in cavity

Manufacturer: Advanced Development Laboratories

Model No.: 1 L (left-hand wound)

3 R (right-hand wound)

Overall dimensions (antenna and cavity): 2 in. x 2 in. x 1 in.

Coupling measurements were taken between the square spiral antenna and a quarter-wave monopole. The monopole was perpendicular to the ground plane, and located 11.3 in. from the center of the square spiral antenna. Coupling patterns were recorded for frequencies from 2 to 4 gc at 100-Mc intervals. Typical curves for Spiral 1 L are shown in Fig. 15.

Further study of these coupling patterns reveals a preponderance of maxima at locations radially out from the antenna corners (at ϕ = 0', 90^{o}, 180^{o}, and 270^{o}).

Figure 16 indicates the maximum and minimum coupling between the 1 L spiral antenna and the quarter-wave monopole, normalized such that the spacing between these two antennas is a constant number of wavelengths. These curves indicate:

a) A relatively small variation in coupling as a function of frequency.

b) A relatively constant difference between maximum and minimum coupling levels over the frequency range.

c) A trend toward increased average coupling as the frequency is increased.

indicate:

a) A greater beam width than that observed for the circular spiral.

b) A relatively constant gain over the frequency range of the antenna.

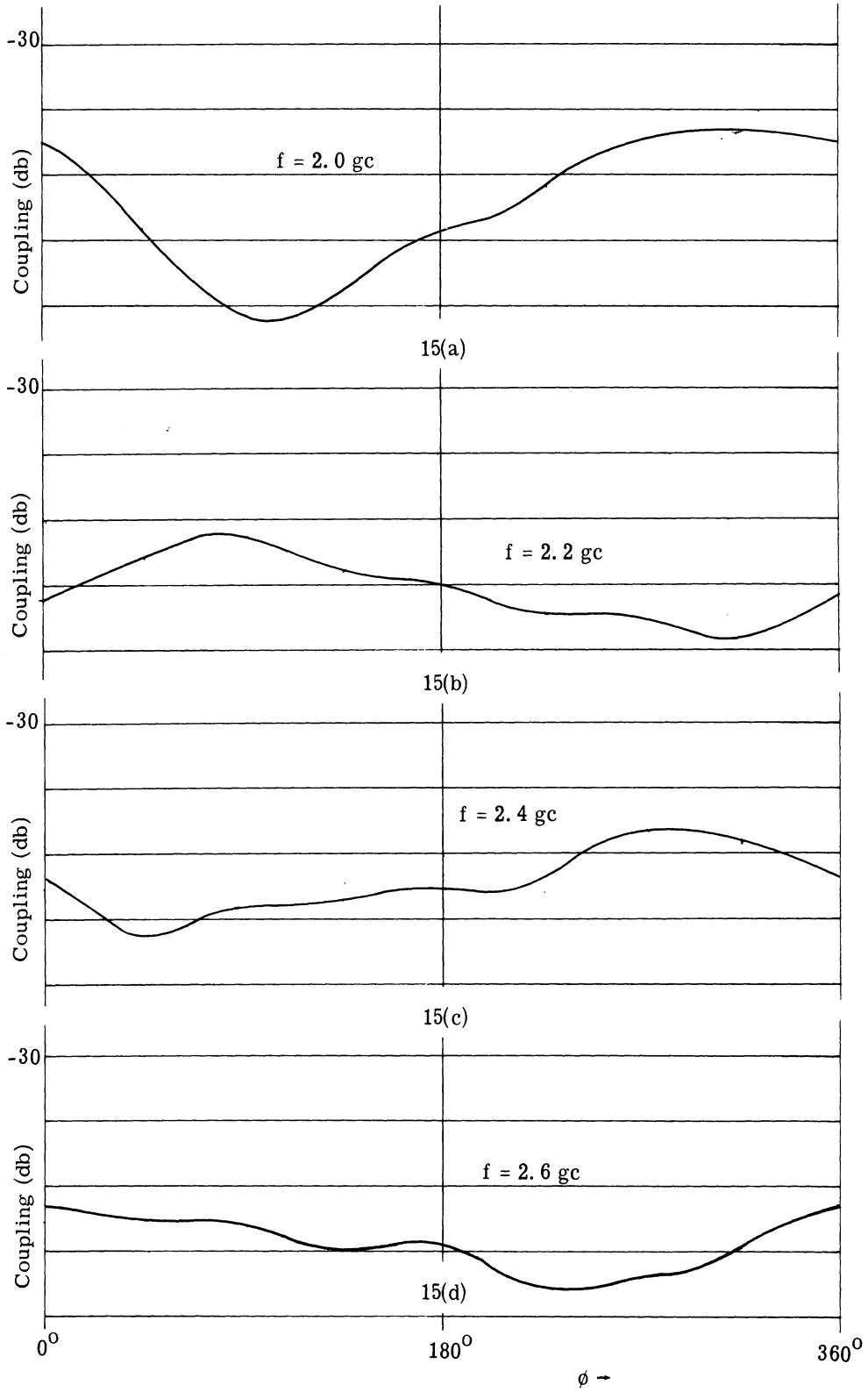

Fig. 15. Coupling patterns for Square Spiral "1L" normalized.

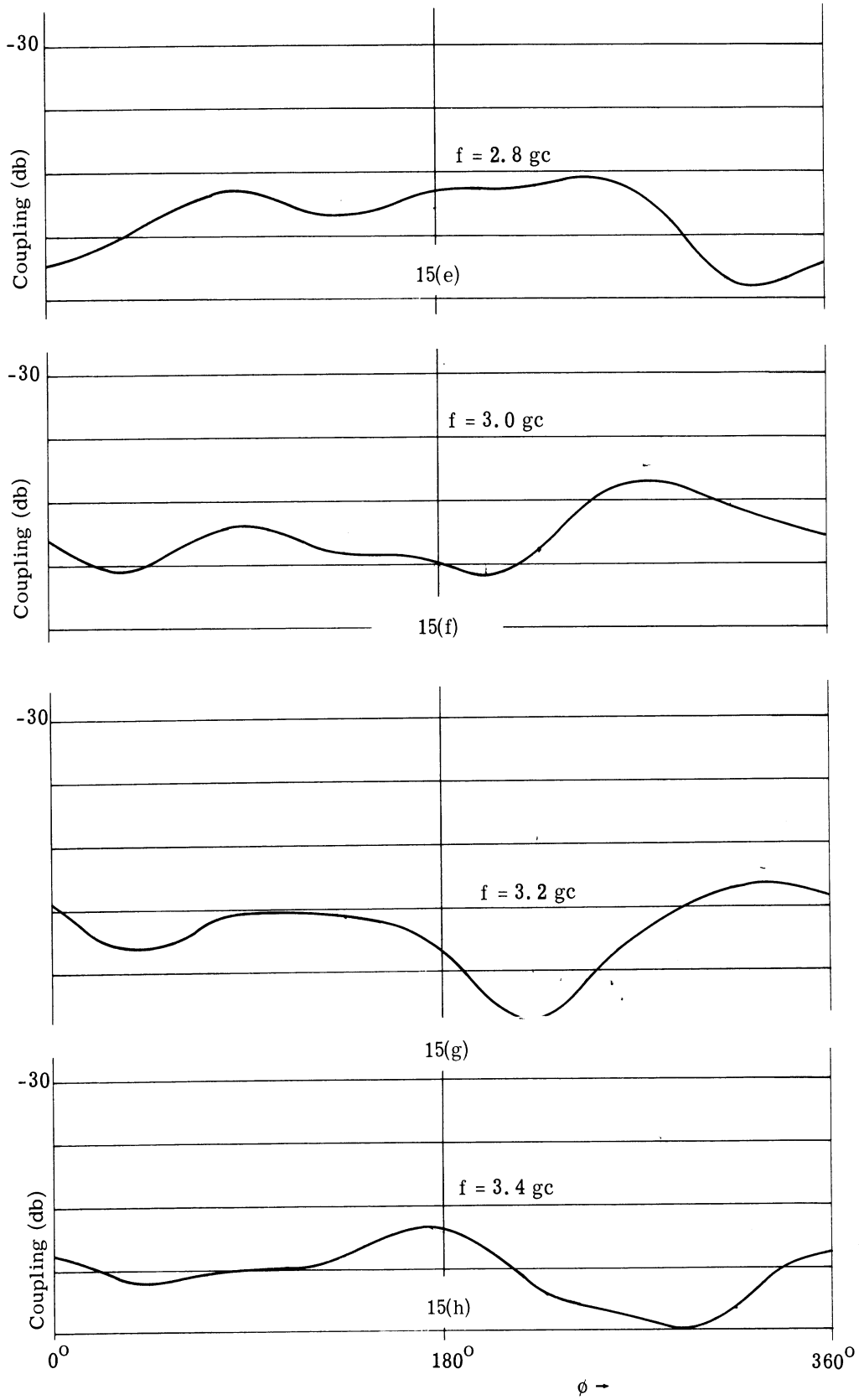

Fig. 15 (Cont.). Coupling patterns for Square Spiral "1L" normalized.

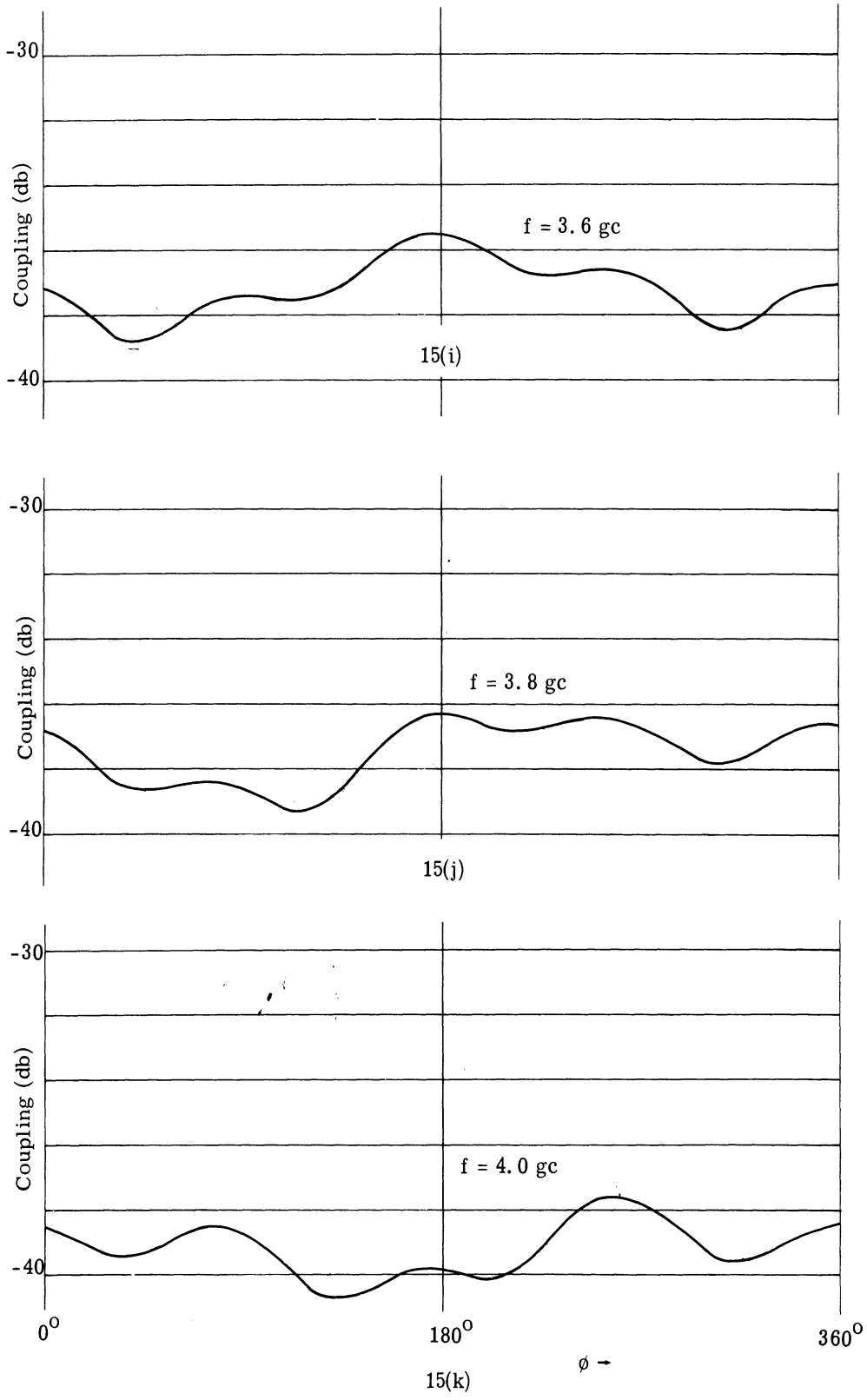

Fig. 15 (Cont.). Coupling patterns for Square Spiral "1L" normalized.

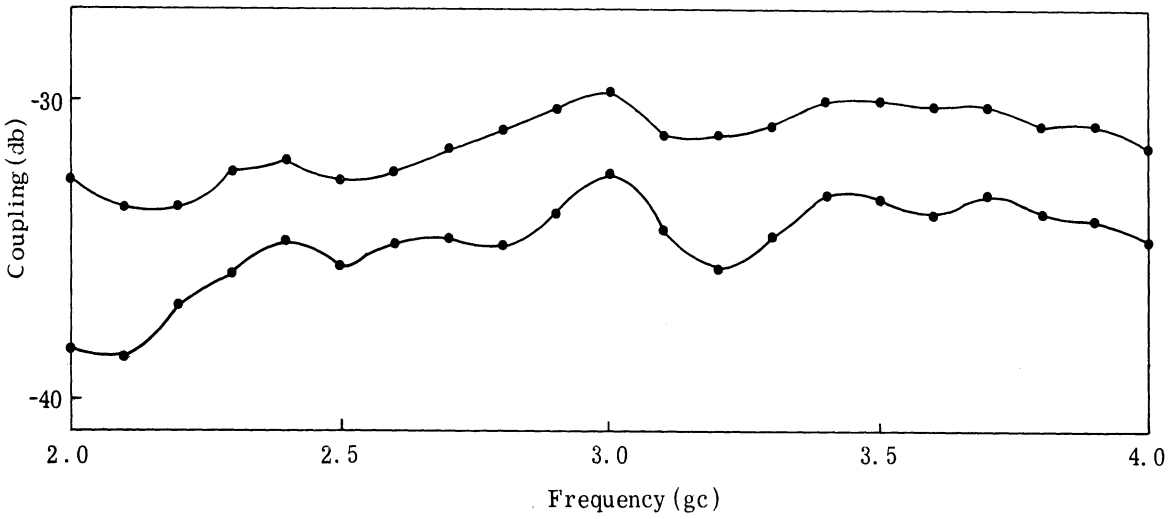

Fig. 16. Total variation of coupling vs. frequency, square spiral "1L".

3.2.4 Fabricated Spiral. In order to control the phase of the feed currents, a laboratory spiral was constructed having the balun outside the cavity. For matching purposes, a dielectric-filled cavity was utilized, the spiral being fed by a tapered two-wire line. The cavity depth is 0.663 inches, a quarter wavelength at the geometric mean frequency in the medium whose dielectric constant is 2.48. The spiral is circular, Archimedean, and has eight turns. Further details are given in Figs. 7 and 17.

When the feed currents are balanced ($\beta = 0$), the coupling pattern has 180° symmetry; that is, $C(\phi) = C(\phi + \pi)$ (see Figs. 18 and 19). The same is true when the feed currents are in-phase. In both cases, the antenna has mechanical and electrical 180° symmetry. Small amounts of in-phase currents have an appreciable effect on the current distribution, and cause an electrical asymmetry. Experiments show that when the current phases are within 10° of balance, the direct radiation from the two-wire line is not significant, although it increases as frequency increases (Fig. 19). Even better balance stability is found with the printed circuit balun in the AGA spirals, since the fields are tightly concentrated between the strip-line conductors. If the phases vary by 90° or more from balance, the direct radiation becomes significant, and the feed structure approaches a monopole. When this happens, the radiation from the feed structure becomes comparable to that of the spiral itself, and the coupling level will increase. The coupling levels and variations observed in the

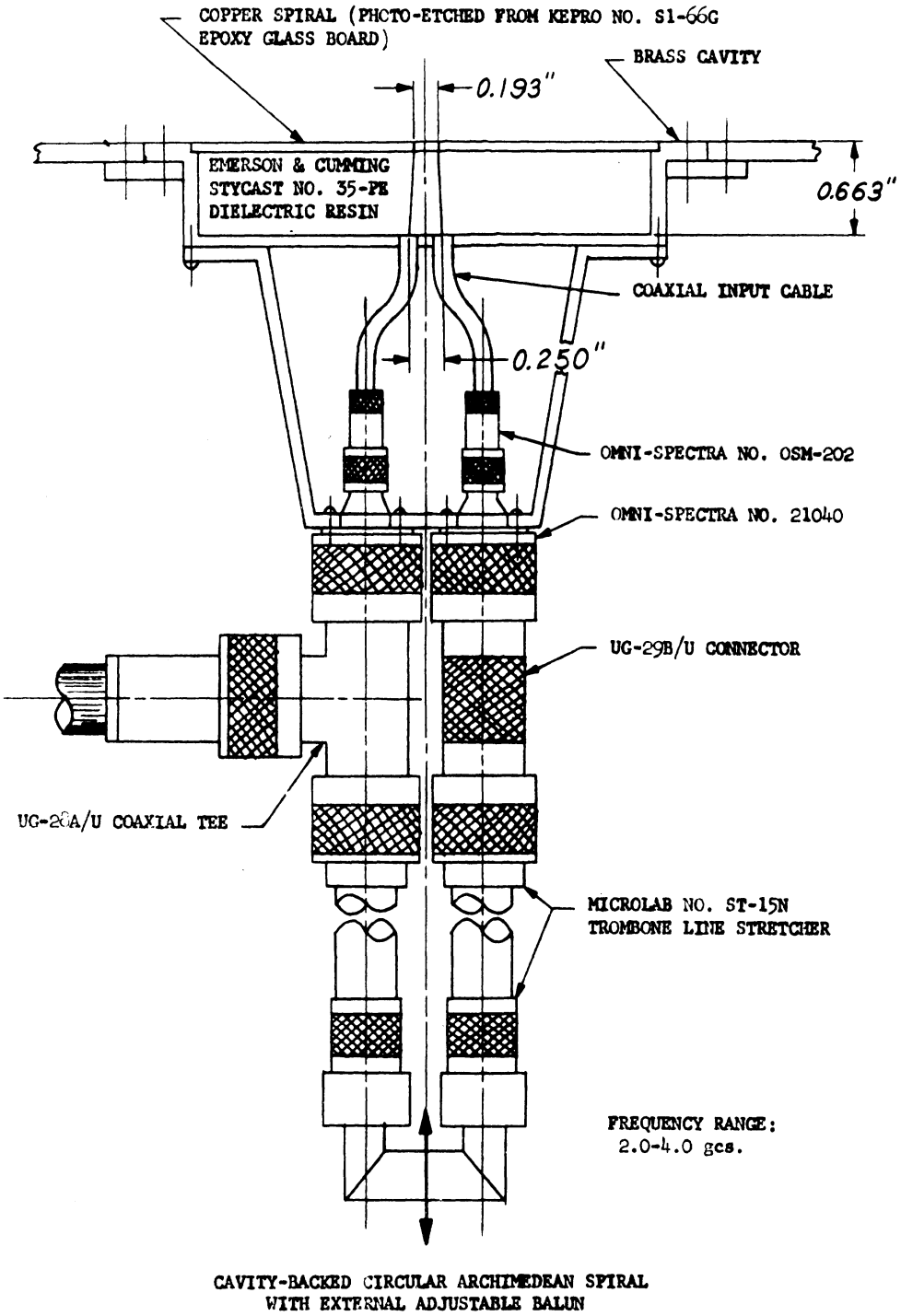

Fig. 17. Construction and feed details of fabricated spiral "WR".

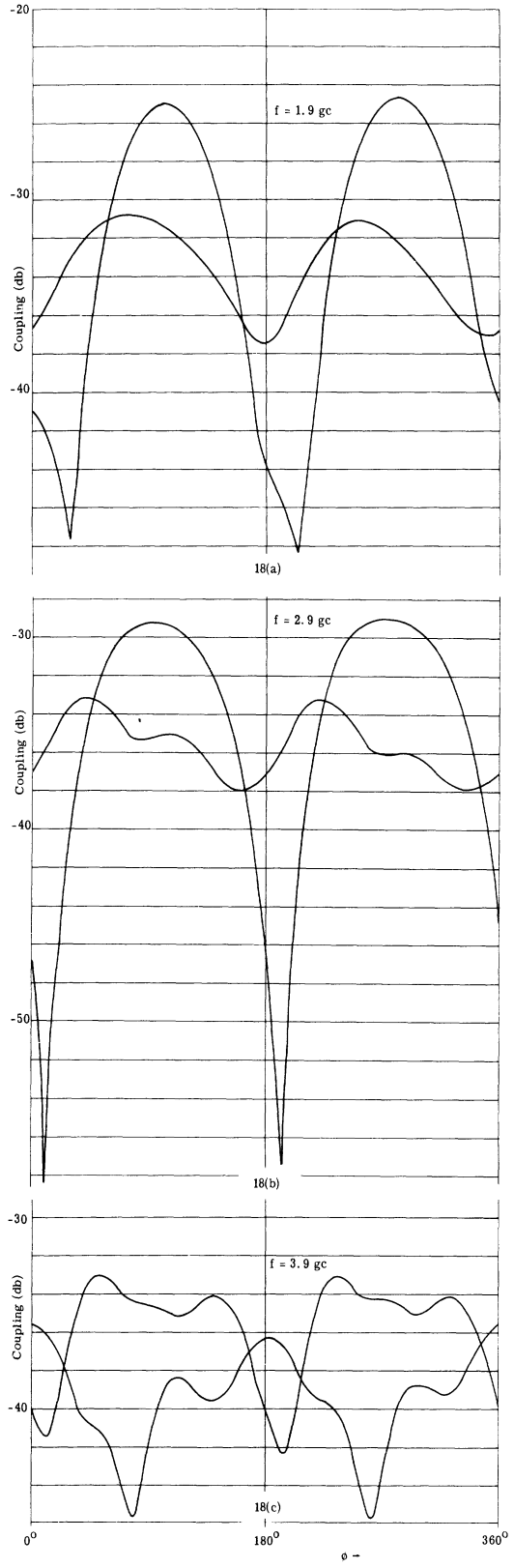

Fig. 18. Coupling patterns for Fabricated Spiral "WR".

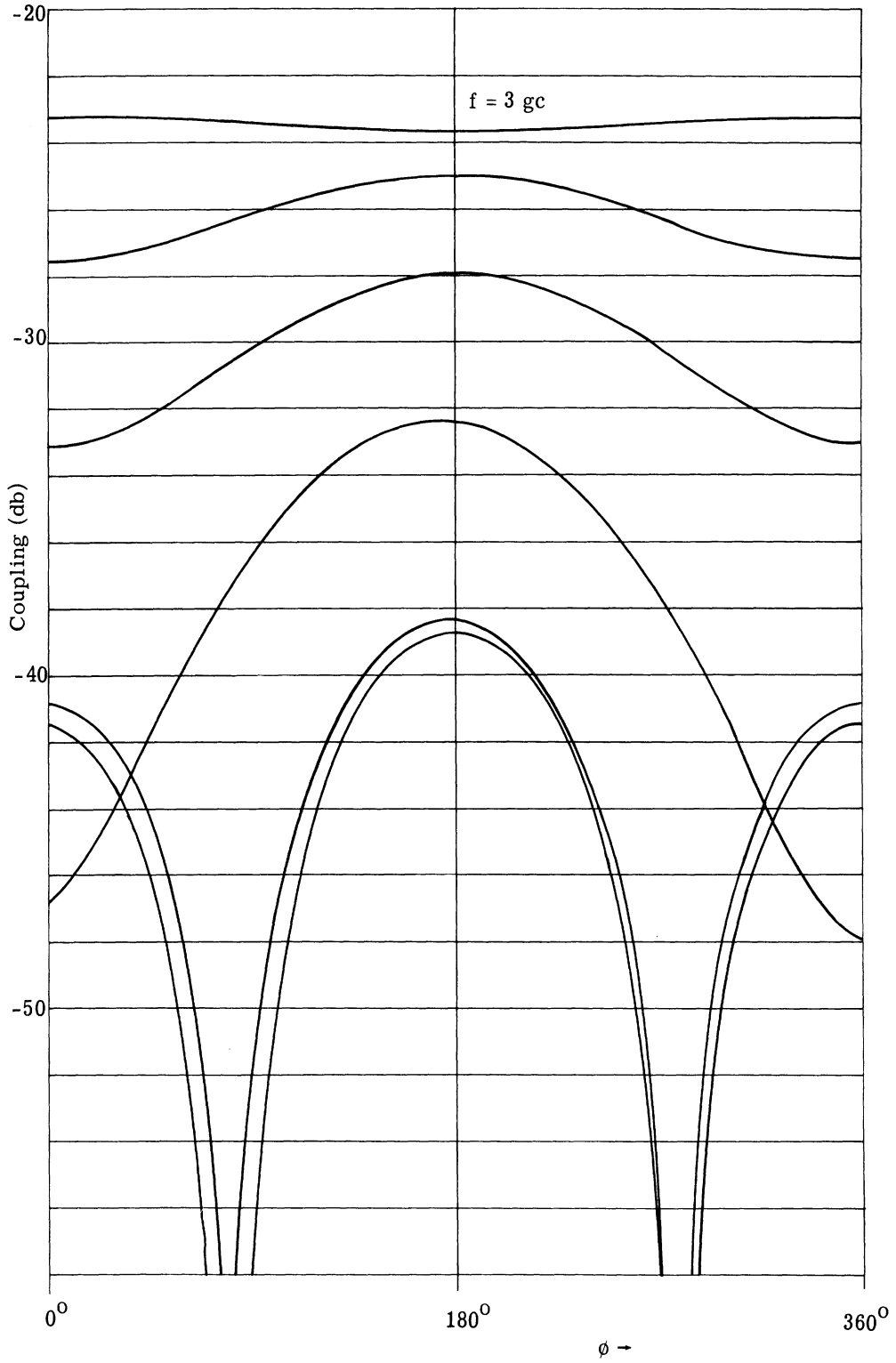

Fig. 19. Coupling pattern from terminated two-wire feed line, spiral face removed.

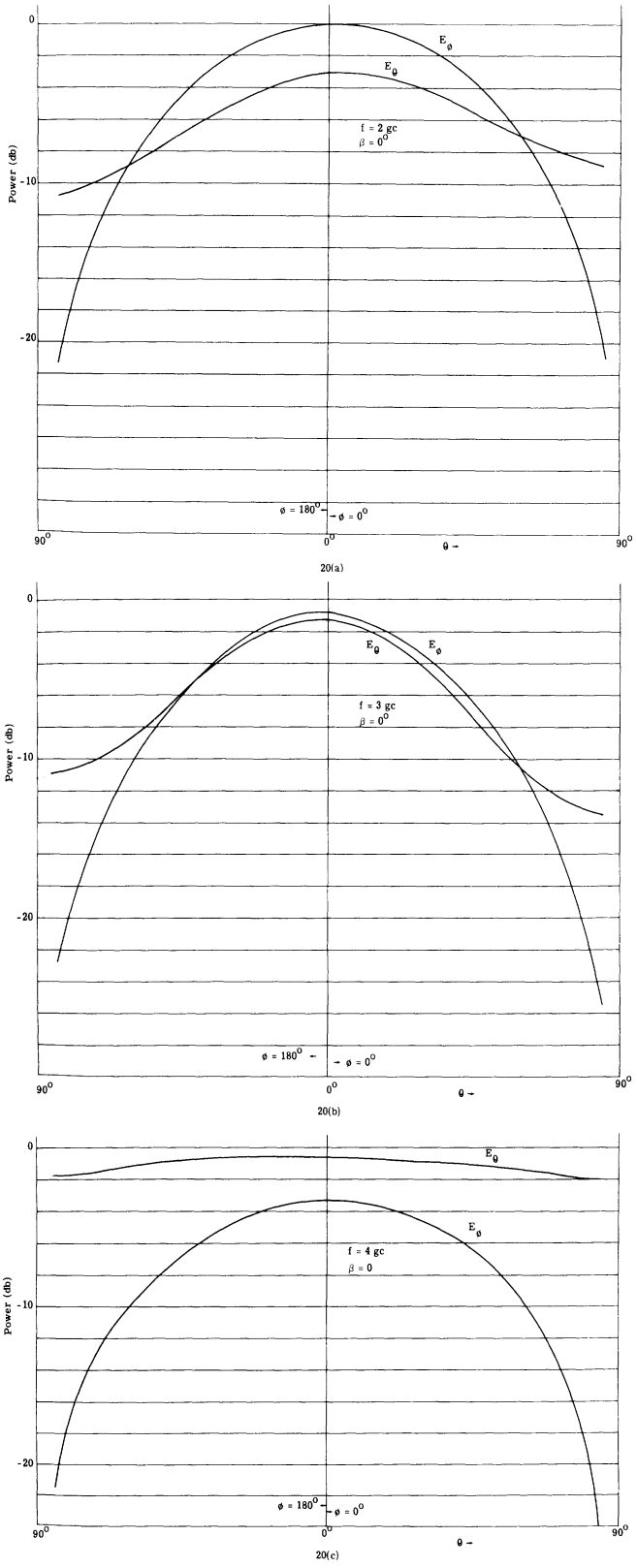

Fig. 20. Radiation patterns for Fabricated Spiral "WR".

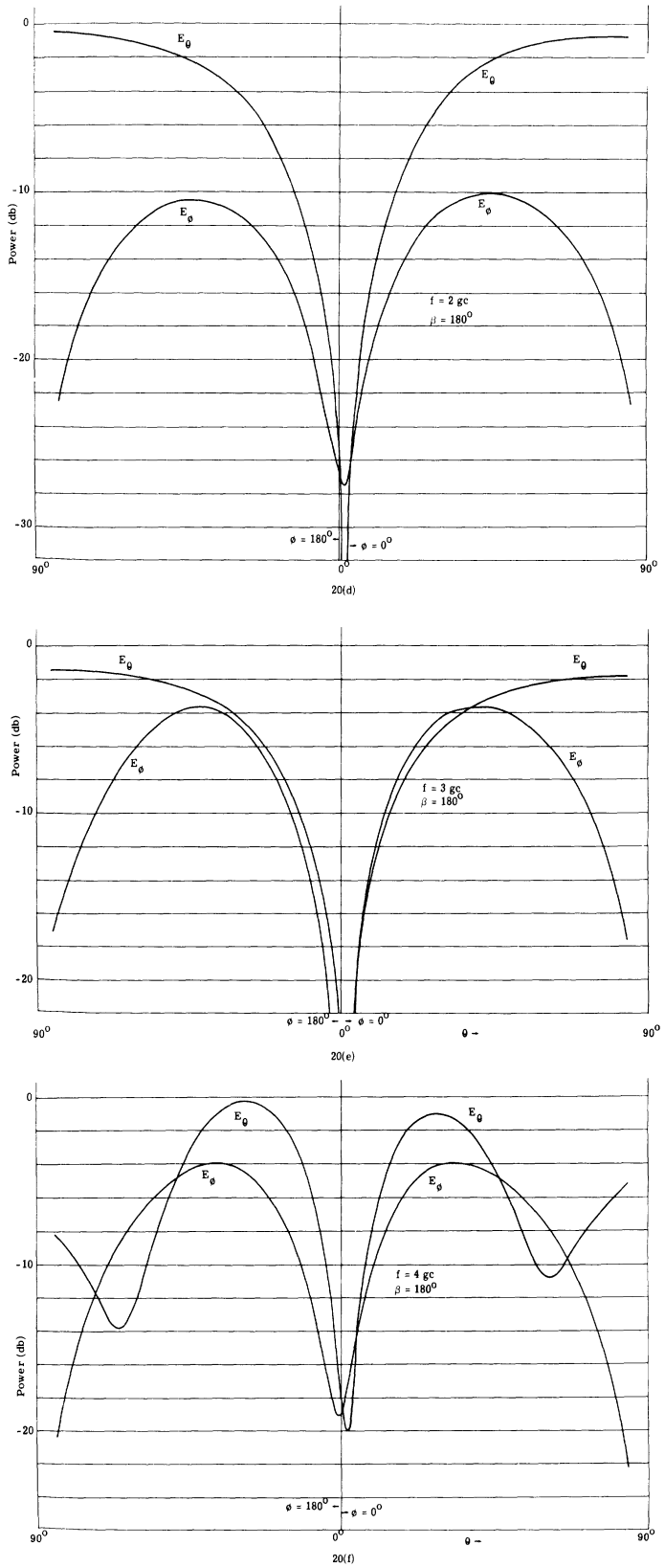

Fig. 20 (Cont.). Radiation patterns for Fabricated Spiral "WR".

commercial spirals are of the same nature and magnitude as those for the fabricated spiral, but differ in detail, since the feed structure and number and size of turns differ.

Patterns for the fabricated spiral are shown in Fig. 20. The extreme broadening of the pattern for frequencies near 4 gc is due to the high effective dielectric constant. Observed coupling levels are consistent with the patterns taken.

In the figures involving the fabricated spiral, the quantity β represents the phase angle between the two arms of the spiral; $\beta = 0$ corresponds to the usual out-of-phase feed, and $\beta = 180^{o}$ corresponds to the second-mode excitation condition, or in-phase. Intermediate phases are achieved by adjusting the balun, shown in Fig. 17. Experimentally, the lengths of the balun were calculated by assuming length and phase-shift to be proportional. Although introducing some error, this assumption is adequate for the purposes of the experiment.

3.2.5 Theoretical Study of the Square Spiral Antenna. A theoretical analysis of the fields from a square spiral antenna is presented in Appendix C. In this analysis it is assumed that current waves travel out from the center terminals of the antenna with a wave propagation constant β which is constant. In addition, it is assumed that the current does not experience reflection at the spiral corners and that it is attenuated in the "radiation region" of the antenna.

The equations resulting from this analysis were programmed for the IBM 7090 computer and radiation patterns were calculated. These patterns were found to check quite well in many respects with those obtained experimentally. Both theoretical and experimental coupling patterns have maxima at positions radially out from the corners of the antenna.

3.2.6 Comparison of Computed Patterns with Experimental Results for Square Spirals. The equations from Appendix C for the electric fields of the square spiral antenna were used to try to predict the fields from the square photo-etched spiral. This spiral has twenty turns and a spacing of .01 in. It is designed to operate between 2 gc and 4 gc. This antenna assembly was mounted in a 12 ft. by 12 ft. ground plane when the measurements were taken. (See Section 3.2.3.) Since the width of the wires and the spacing between wires are equal, the antenna and the ground plane can be considered as being the complement of a square spiral in free space. The free space spiral has the same geometry as the spiral formed by the spaces between wires on the spiral. Equations for predicting the fields of the

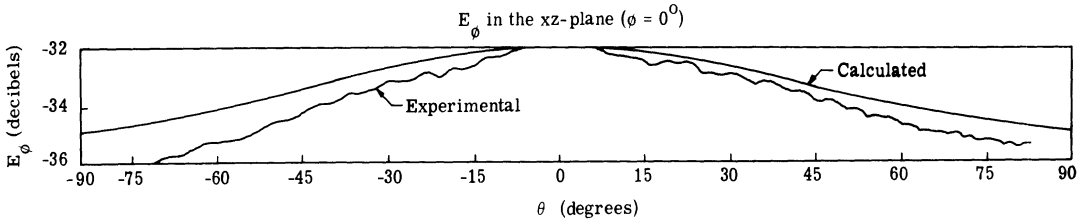

Fig. 21. Experimental and theoretical radiation patterns, square spiral.

ADL spiral in a ground plane are then found by interchanging E_ϕ and E_θ in the equations for the complementary free-space spiral.

It should be noted that the radiation from any spiral is affected by the cavity and the photo-etched balun in the feed system. These effects are not considered in the derivation of the field equations and hence do not appear in the computed patterns. Both theoretical and experimental patterns are shown in Fig. 21. The absolute levels of the theoretical curves are arbitrary since they depend on the current at the terminals, which is not known exactly. Note that in Fig. 21 the experimental pattern has higher directivity than the computed pattern. This is due to the fact that the cavity radiates more power directly outward than in directions near the ground plane.

In Fig. 22 there are definite maxima at locations near the spiral corners in both the experimental and computed patterns. Note, however, that the experimental pattern does not contain a great degree of symmetry for field points 180 degrees apart. This deviation from the theory is primarily due to the imbalance in the feed caused by the balun, and by direct radiation from the balun.

An attempt to simulate this imbalance was made by calculating a pattern for the case of unbalanced currents at the feed terminals. Since no information was available concerning the amount of imbalance the balun caused, a guess was made. A six-degree error in the phase and a two-to-one ratio in the amplitudes of the terminal currents were assumed. The resulting field pattern is shown at the top of Fig. 22. The curve suggests that if the actual imbalance in the feed were known, then closer correlation with experimental results could be realized.

The pattern for the component of electric field in the plane of the spiral (Fig. 23) is symmetric with respect to the origin; that is, the magnitudes of the electric fields at points

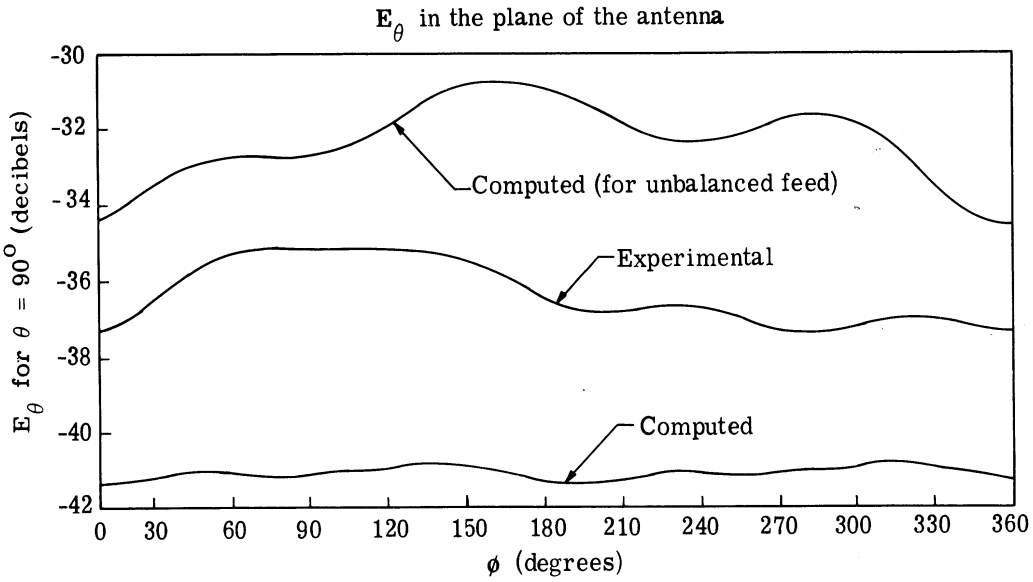

Fig. 22. Experimental and theoretical coupling patterns, square spiral.

180 degrees apart are equal. This result was predicted since diametrically opposite points on the spiral (points reflected through the origin) carry identical currents. Computer results also revealed a 360-degree phase shift for E_ϕ as ϕ is varied from zero to 2π radians.

3.3 Horn Coupling: Theoretical Considerations of Aperture

3.3.1 General Aperture. If the geometry shown in Fig. 24 is used, the far-field expressions of an arbitrarily shaped aperture source in a ground plane are

$$
\begin{aligned}
E_r &= 0 \\
E_\theta &= \frac{k}{2\pi j} \frac{e^{-jkR}}{R \sin\theta} \int_A \bar{E}(\bar{\rho}) \cdot \hat{R}\, e^{jk\bar{\rho} \cdot R}\, dA \\
E_\phi &= \frac{jk}{2\pi} \frac{e^{-jkR}}{R} \cos\theta \int_A \bar{E}(\bar{\rho}) \cdot \hat{\phi}\, e^{jk\bar{\rho} \cdot \hat{R}}\, dA \qquad (3.6) \\
H_r &= 0 \\
H_\theta &= \sqrt{\frac{\epsilon}{\mu}}\, E_\phi \\
H_\phi &= \sqrt{\frac{\epsilon}{\mu}}\, E_\theta
\end{aligned}
$$

Here the integration is over the whole area A of the aperture, and the circumflex (Λ) indi-

(a) E_{ϕ} in the xz Plane

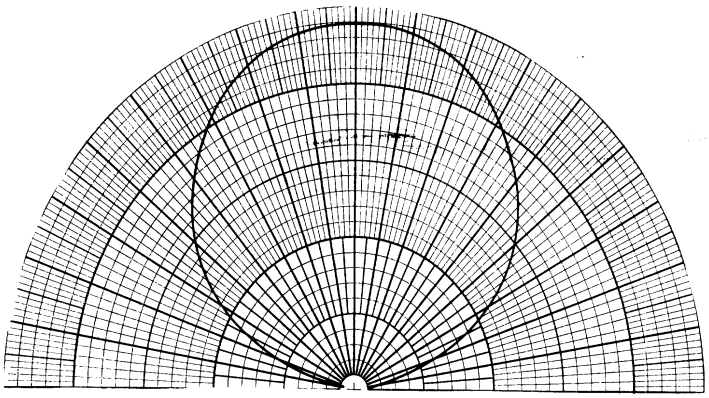

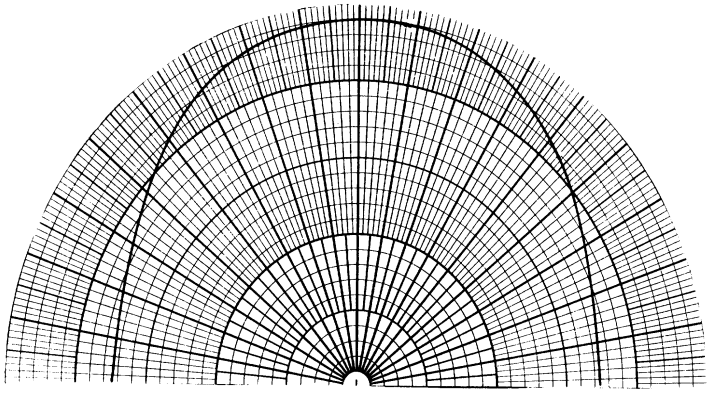

(b) E_{θ} in the xz Plane

(c) E_{θ} in the Plane of the Spiral (xy Plane)

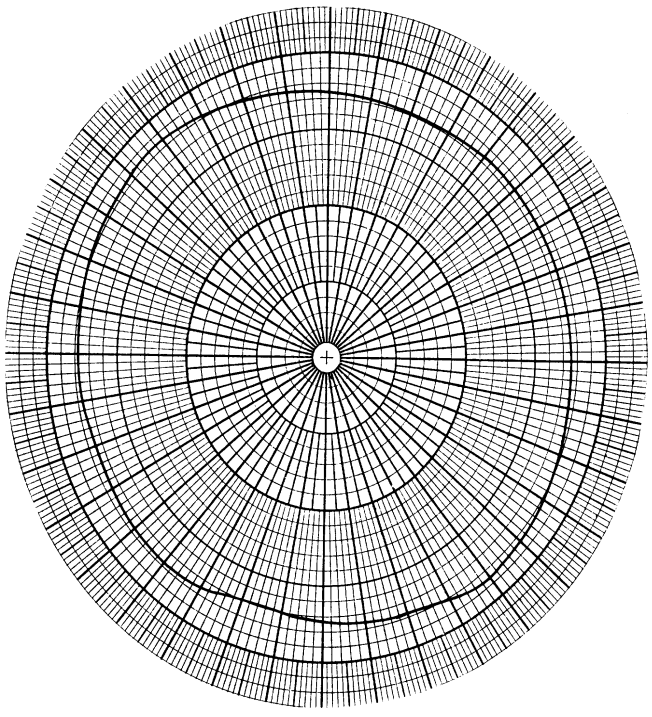

Fig. 23. Predicted patterns of square spiral.

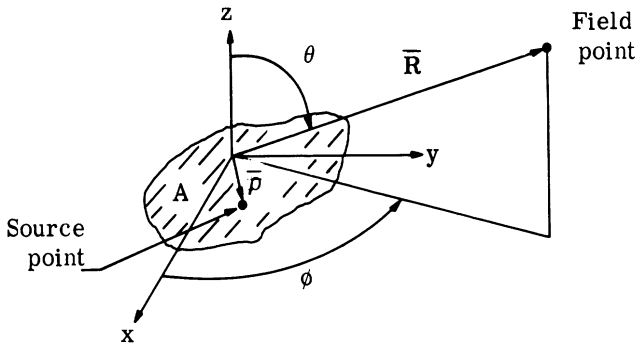

Fig. 24. Geometry of general ground plane aperture.

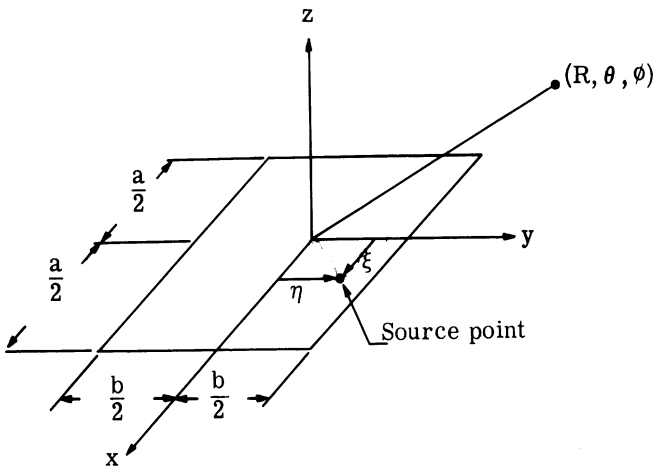

Fig. 25. Geometry of rectangular aperture.

cates a unit vector.

These formulas were developed here in an internal memo, but a more direct method is given by Harrington (Ref. 12). They can be derived from

$$\bar{E}(\bar{R}) = -\nabla \times \iint_{\text{plane}} \frac{e^{-jkr}}{2\pi r} \bar{E}(\bar{\rho}) \times \hat{z}\, dA$$

where r is the distance from the source point to the field point, by using the far-field approximation

$$r \approx R - \bar{\rho} \cdot \hat{R} .$$

3.3.2 Rectangular Aperture. In the case of a rectangular aperture such as a flush-mounted horn, these expressions simplify. In general, a horn is fed by a waveguide which is excited in the TE_{10} mode; thus, the aperture field is linearly polarized, e.g., $\bar{E}(\bar{\rho}) = E(\bar{\rho})\hat{\eta}$. The geometry of Fig. 25 shows that

$$E_\theta = \frac{k}{2\pi j} \frac{e^{-jkR}}{R} E_o \sin\phi\, g(\theta,\phi)$$

$$E_\phi = \frac{jk}{2\pi} \frac{e^{-jkR}}{R} E_o \cos\theta \cos\phi\, g(\theta,\phi) \qquad (3.7)$$

where

$$g(\theta,\phi) = \int_{-a/2}^{a/2} d\zeta \int_{-b/2}^{b/2} f(\zeta,\eta)\, e^{jk \sin\theta(\zeta\cos\phi + \eta\sin\phi)}\, d\eta \qquad (3.8)$$

where

E_0 = maximum value of the aperture electric field, and

$f(\zeta,\eta)$ = distribution of the aperture electric field.

This expression, has been given much attention, summarized by Silver (Ref. 5), so that the results there can be directly applied to the flush-mounted horn. The two factors to be considered in the aperture are the field distribution and the phase distribution. A summary of the results is now presented.

For a first approximation, the phase variation can be ignored. Near $\theta = 0$ (along the main beam), this assumption will give good results. As the aperture becomes larger in terms of wavelengths, the fields away from the main beam become more highly affected by phase variations. Thus, the coupling between a horn and another antenna in a ground plane is sensitive to phase variations. The presence of this effect necessitates a detailed knowledge of the aperture fields. Phase variations can be calculated for horns by consideration of the flare angle.

First of all, most horns have aperture fields that are "separable," i.e.,

$$f(\xi, \eta) = f_{\xi}(\xi)\, f_{\eta}(\eta)$$

Then,

$$g(\theta, \phi) = \left[\int_{-a/2}^{a/2} f_{\xi}(\xi)\, e^{jk\xi \sin\theta \cos\phi}\, d\xi \right] \cdot \left[\int_{-b/2}^{b/2} f_{\eta}(\eta)\, e^{jk\eta \sin\theta \sin\phi}\, d\eta \right] . \tag{3.9}$$

From this, it can be seen that the problem reduces to one of evaluating the integrals

$$G_u(u) = \frac{a}{2} \int_{-1}^{1} e^{jux} f_u(x)\, dx \tag{3.10}$$

and

$$G_v(v) = \frac{b}{2} \int_{-1}^{1} e^{jvy} f_v(y)\, dy$$

where

$$x = \frac{2\xi}{a}$$

$$y = \frac{2\eta}{b}$$

$$u = \frac{ka}{2} \sin\theta \cos\phi$$

$$v = \frac{kb}{2} \sin\theta \sin\phi \tag{3.11}$$

$$g(\theta, \phi) = G_u(u)\, G_v(v)$$

In a great number of applications, the horn is fed in such a way that the magnitude of the electric field is independent of η. The magnitude of the ζ-distribution in a small horn (e.g., an open-ended wave guide) is roughly that of the TE_{10} mode, $\cos\frac{\pi\zeta}{\alpha}$. As the horn is increased in size, higher-order TE_{n0} modes can come into play. In the case of the common pyramidal horn, the transition from waveguide modes to propagating modes takes place smoothly enough so that higher-order modes are not significant. In a box horn, however, the odd-numbered TE_{n0} modes are excited, and the distributions of the aperture field become flattened in the center of the horn, tapering to zero at the sides. This latter effect can be approximately represented by a trapezoidal distribution.

3.3.3 Constant-Phase Aperture. Phase variations are momentarily ignored, and the following three distributions are considered:

(1) Constant, representing a limiting case.

(2) Cosine, the standard distribution.

(3) Trapezoidal, in-between distributions (1) and (2).

It will be shown that a constant distribution gives the sharpest main beam and the highest sidelobes, and a cosine distribution gives a broader beam and reduced sidelobes. (This is often referred to as the "array taper effect.") The trapezoidal distribution falls in between, and its shape is dictated by the horn and feed configuration and size.

(1) For the constant distribution: $f_u(x) = 1$, $f_v(y) = 1$.

$$G_u(u) = a\,\frac{\sin u}{u}$$
$$G_v(v) = b\,\frac{\sin v}{v} \qquad (3.12)$$

(2) For the cosine distribution: $f_u(x) = \cos\frac{\pi}{2}x$, $f_v(y) = 1$

$$G_u(u) = \frac{2a}{\pi}\,\frac{\cos u}{1-\frac{4u^2}{\pi^2}}$$
$$G_v(v) = b\,\frac{\sin v}{v} \qquad (3.13)$$

(3) For the trapezoidal distribution: $f_u(x) = \begin{cases} \frac{1+x}{1-\alpha} & -1 \leq x \leq -\alpha \\ 1 & -\alpha \leq x \leq \alpha \\ \frac{1-x}{1-\alpha} & \alpha \leq x \leq 1 \end{cases}$, $f_v(y) = 1$

$$G_u(u) = a \frac{\cos \alpha u - \cos u}{(1-\alpha) u^2}$$

$$G_v(v) = b \frac{\sin v}{v} \qquad (3.14)$$

Since these quantities will eventually be squared, they are shown in decibel form, where zero corresponds to the case u = v = 0, the maximum of the function for these distributions. For small values of u, the trapezoidal distribution approaches the constant distribution, i.e.:

$$G_u(u) = a \frac{\cos \alpha u - \cos u}{(1-\alpha) u^2} \approx a \frac{\sin u}{u} \quad .$$

For large values of u:

$$G_u(u) \approx \frac{1}{u^2} \quad . \qquad (3.15)$$

The function $G_u(u)$ depends on the distribution $f_u(x)$ as well as "u". This is plotted for several distributions in Fig. 26, where the oscillatory terms are ignored, for reasons cited below. As an example, to obtain the fields of a pyramidal horn, one would choose the cosine distribution (2) above, find the values of $G_u(u)$ and $G_v(v)$ from Fig. 23, and use Eqs. C.2 and C.6.

The wavefront at the mouth of most horns does not have a constant phase over the aperture. The sharper the flare of the horn, the more pronounced the variation of phase. These variations tend to broaden the beam and smooth out the sidelobe pattern, and generally raise the sidelobe level somewhat. The curves of Fig. 26 will yield first-order answers which are adequate for many RFI purposes, within ±7 db. If further accuracy is desired, the horn flare and feed characteristics will have to be considered. Phase variations are discussed in Silver (Ref. 5, p. 186).

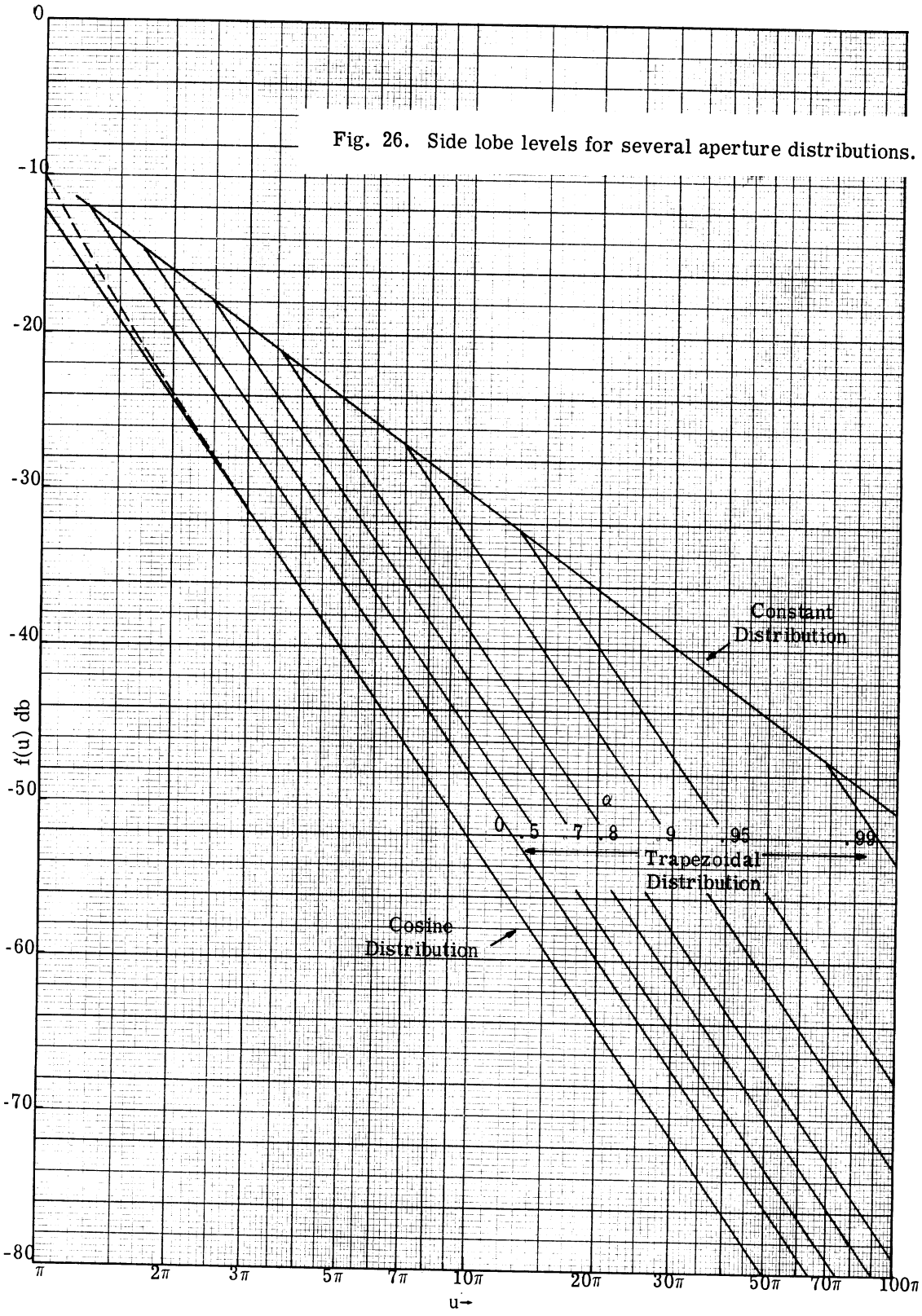

Fig. 26. Side lobe levels for several aperture distributions.

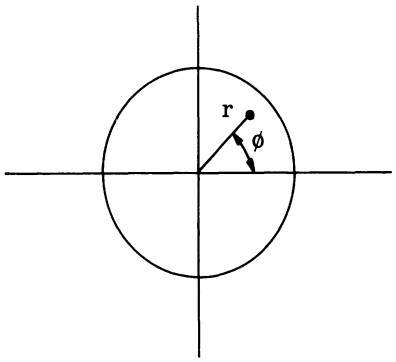

Fig. 27. Cross-section of dielectric rod.

3.4 Dielectric Rod Antennas

Introduction. Dielectric rods have been in general use for obtaining directional radiation patterns since shortly before World War II.

3.4.1 Mode of Operation. A dielectric rod antenna can be operated in several different modes depending on the type of excitation supplied by the feed, the operating frequency, the rod diameter, and the dielectric constant of the rod. The problem of electromagnetic wave propagation along a dielectric rod has been solved satisfying the boundary values imposed by the surface of an infinitely long dielectric rod (see Ref. 6). It is found in general that pure TE or TM modes can only exist on a dielectric rod if there is no dependence of the fields on the azimuth angle ϕ (see Fig. 27).

For the general solution of the wave equation one obtains hybrid modes which are designated as HE or EH, depending on whether the TE(H) or TM(E) mode is predominant, respectively.

All modes except the HE_{11} mode have a cutoff frequency. Therefore, by operating at a low enough frequency, one can always operate the antenna in a single mode, the HE_{11}. The field distribution for the HE_{11} mode is shown in Fig. 28. This distribution is quite similar to the TE_{11} mode in circular wave guide.

Figure 29 (Ref. 7, p. 482) shows the ratio of c/v, the ratio of wave propagation velocity in free space to that in the dielectric.

As shown in Fig. 29, for $\epsilon = 2.56$ (the dielectric constant of polystyrene), one can operate up to a frequency where $d/\lambda = 0.6$ before exciting higher order modes.

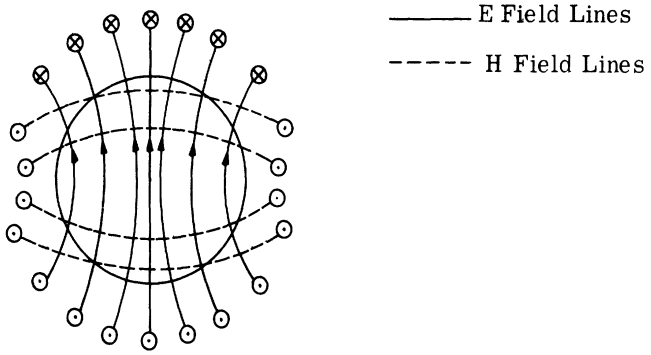

Fig. 28. HE_{11} mode for the dielectric rod.

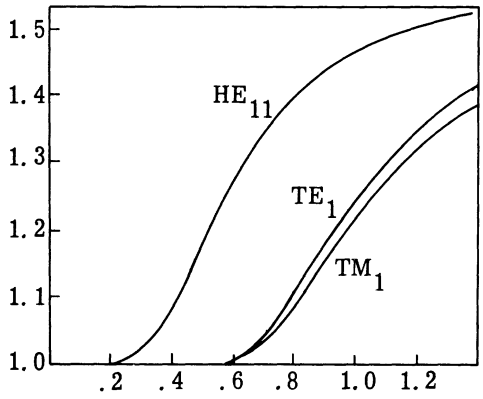

Fig. 29. Ratio of c (free space wave velocity) to v (dielectric wave velocity) for $\epsilon = 2.56$.

3.4.2 Energy Concentration. The closer the dielectric wave velocity comes to c, the less tightly the energy is coupled to the dielectric guiding structure. It is not very difficult, however, to obtain close coupling of the wave to the dielectric rod. For example, as long as $c/v \geq 1.05$, 50 percent or more of the total energy travels within a distance of 0.2λ of the rod surface. This condition is satisfied, according to Fig. 29 for $d > 0.3\lambda$.

3.4.3 Operating Mode. Since the HE_{11} mode has no cutoff, it is the lowest order mode one can excite. At any one cross section, the E-field lines excited are in phase and give rise to radiation in the form of a forward lobe. This is the pattern which has been predominantly used with dielectric rod antennas.

3.4.4 Directivity. Dielectric rods, especially ones that are untapered (and therefore have uniform phase velocity along the full length of the antenna) are limited in

their directivity to about 15 db (corresponding to a minimum half-power beamwidth of about 30^{o}). This limitation in directivity is brought about by the first sidelobe being merged into the main lobe, thus bringing about a broadening of the main lobe. The merging of the two beams occurs when one tries to make an untapered rod too long, i.e., exactly under the condition which would give increased directivity.

3.4.5 Side Lobe Levels. For untapered dielectric rod antennas, first sidelobe levels are usually less than 10 db below the main beam. This is due to the behavior a uniform current sheet exhibits when the velocity of a wave propagating along it is uniform and slightly lower than that of a wave in free space. For untapered rods, the directivity for a fixed d/λ, as a function of length will increase until one reaches the Hansen-Woodyard condition, i.e., the point at which the wave at the end of the radiator is 180^{o} out-of-phase with the direct free space wave originating from the feed end of the rod. As is well known, as one approaches the Hansen-Woodyard condition, the first sidelobe increases its level. For even more of a phase shift between the two ends of the rod, the first sidelobe increases until it becomes as large as or even larger than the desired end-fire radiation lobe.

3.4.6 Analysis of Coupling of Two Parallel Rods. A one-dimensional analysis of the coupling factor was derived for two equal length, parallel dielectric rods. The case analyzed is that of two parallel rods, either with parallel or anti-parallel wave propagation, for the case of the electric probe feeds parallel. If the feed probes were oriented at an angle ϕ with respect to each other, an additional decoupling of the fields equal to $\cos \phi$ would occur.

The following is a description of the detailed attack undertaken: First, the far-field pattern of an untapered dielectric rod can be very well represented by

$$E_{\theta} = \frac{1}{r} (\sin u)/u$$

where

$$u = \frac{L}{2} (\beta - k \cos \theta)$$

L = length of antenna

$$\beta = \frac{2\pi}{\lambda_v}$$

$$k = \frac{2\pi}{\lambda}$$

λ_v = guide wave length in dielectric rod

λ = wavelength in air

θ = angle measured from the rod axis.

To compute the emf V on the receiving rod, the following integral was set up:

$$V_{received} = A \int_0^L \overline{E}_{transmitted}(z) \cdot e^{-j\beta_r z} \overline{dz}$$

(where A is a proportionality constant).

The problem then becomes one of evaluating the above integral which turns out to be:

$$V_{received} = A \int_0^L \frac{1}{r} \frac{\sin \frac{1}{2}(\beta_t - k \cos\theta)}{\frac{L}{2}(\beta_t - k \cos\theta)} \sin\theta \, e^{-j\beta_r z} \, dz$$

where

β_t = wave number of transmitting antenna

β_r = wave number of receiving antenna

$$\sin\theta = \frac{d}{\sqrt{d^2 + z^2}}$$

$$\cos\theta = \frac{z}{\sqrt{d^2 + z^2}}$$

The above integral only takes into account the far-field pattern of the transmitting antenna.

In order to simplify the evaluation of the above integral, it was broken up into one wavelength long segments, with an expansion taken around the center of these segments (i.e., at the points z = i - 1/2, i integer):

$$V_{received} = \sum_{i=1}^{N} \frac{e^{-j2\pi R_{o_i}}}{R_{o_i}}$$

$$\int_{-1/2}^{1/2} \frac{\sin\left[\pi L_o \left(C_1 - (\cos\theta_i + \xi/R_{o_i})\right)\right]}{\pi L_o \; C_1 - (\cos\theta_i + \xi/R_{o_i})} \cdot \sin\theta_i$$

$$\cdot \; e^{-j\pi L_o \left[C_2 - (\sin\theta_i + \xi/R_{o_i})\right] \left[(i - 1/2) + \xi\right]} \; d\xi$$

N = length of receiving rod in wavelengths

$$\theta_i = \tan^{-1}\left[\frac{d_o}{(i - 1/2)}\right]$$

with

$$R_{o_i} = \sqrt{d_o^{\,2} + (i - 1/2)^2}$$

$$L_o = L/\lambda$$

$$d_o = d/\lambda$$

This integral becomes, approximately:

$$V_{\text{received}} = j \sum_{i=1}^{N} P_i \int_{-1/2}^{1/2} \left(1 + \frac{\xi}{A_{i_1} R_{o_i}}\right)$$

$$\left\{ e^{-j\pi L_o A_{i_1}} e^{-j\pi L_o \xi \left[A_{i_2} + \frac{(i-3/2)}{R_{o_i}}\right]} - e^{j\pi L_o A_{i_1}} e^{-j\pi L_o \xi \left[A_{i_2} + \frac{(i+1/2)}{R_{o_i}}\right]} \right\} d\xi$$

with

$$A_{i_1} = C_1 - \cos\theta_i$$

$$A_{i_2} = C_2 - \sin\theta_i$$

C_1 = c/v for transmitting antenna

C_2 = c/v for receiving antenna

$$P_i = \frac{e^{-j2\pi R_{o_i}} e^{-j\pi L_o (i - 1/2) A_{i_1}}}{2\pi L_o A_{i_1} R_{o_i}} \sin\theta_i$$

Now set:

$$I_1(a) = \int_{-1/2}^{1/2} e^{jax}\,dx = \frac{2}{a}\sin a/2$$

$$I_2(a) = j\int_{-1/2}^{1/2} xe^{jax}\,dx = \frac{1}{a}\left[\cos a/2 - \frac{2}{a}\sin a/2\right]$$

Then the final expression becomes:

$$V_{received} = \sum_{i=1}^{N} P_i \left\{ j\, e^{-j\pi L_o A_{i_1}} I_1\left[\pi L_o\left(A_{i_2} + \frac{i-3/2}{R_{o_i}}\right)\right]\right.$$

$$- j\, e^{j\pi L_o A_{i_1}} I_1\left[\pi L_o\left(A_{i_2} + \frac{i+1/2}{R_{o_i}}\right)\right]$$

$$- \frac{e^{-j\pi L_o A_{i_1}}}{A_{i_1} R_{o_i}} I_2\left[\pi L_o\left(A_{i_2} + \frac{i-3/2}{R_{o_i}}\right)\right]$$

$$\left. + \frac{e^{j\pi L_o A_{i_1}}}{A_{i_1} R_{o_i}} I_2\left[\pi L_o\left(A_{i_2} + \frac{i+1/2}{R_{o_i}}\right)\right]\right\}$$

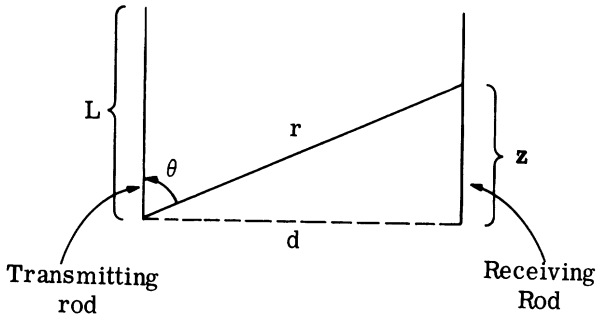

Fig. 30. Coupling geometry for two rods.

3.4.7 Radiation Patterns. Two radiation patterns are shown in Fig. 31 for the case of a two-wavelength long radiator and a six-wavelength long radiator. The ratio c/v is 1.25 and 1.08, respectively. These particular ratios were chosen because they represent the Hansen-Woodyard condition of increased gain. Physically, in the Hansen-Woodyard wave propagating in the dielectric is equal to that of the free space wave plus 180°, i.e., $\beta L = kL + \pi$. In both cases, the main beam is narrower and the sidelobe levels are higher than they would be for the ordinary endfire condition (which, incidentally, can be realized only approximately with a dielectric rod radiator, since it requires v = c). The beamwidth between 3-db points is 44° for $L = 2\lambda$ and 24° for $L = 6\lambda$. The highest sidelobe levels in the two cases are -9 db for $L = 2\lambda$, and -11 db for $L = 6\lambda$.

3.4.8 Coupling Factor. Figure 32 presents the coupling factor for two rods of equal length for two cases. The two rods in each set have the same dielectric wave velocity. For each set of radiators, two cases are shown: The lower coupling level curve (drawn in solid lines) stands for the normal case in which both rods would radiate in the same direction if energized. The higher coupling curve (drawn in dotted lines) shows the coupling if one of the rods would be reversed. This latter case of course, would not be of interest in practical arrays. The curves of coupling factor (in db) versus rod-to-rod distance generally show the expected dependence. For the case of $L = 2\lambda$, the coupling for the normal case oscillates gently about the 6 db per octave line. For d less than 4λ, the coupling increases more rapidly than the 6-db line, as is to be expected just from the geometry of the situation. At $d = 3.3\lambda$, for example, the tip of the receiving rod is being illuminated by the maximum of the first sidelobe of the transmitting rod. According to this, one would expect an increase in the power coupled for spacings around 3.3λ.

For the 6λ rods, the oscillatory variations about the 6-db line are seen to be quite pronounced. This prediction is quite reasonable in view of the many lobed sidelobe structure of the transmitting antenna. In order to indicate what kind of variations in coupling versus spacing one might intuitively expect, it is useful to determine the spacings at which the peaks of the first and the next to the last sidelobe are intercepting the tip of the receiving antenna. From Fig. 31, these are seen to occur at $\theta = 34^{\circ}$ and $\theta = 81^{\circ}$, respectively. The spacing for just intercepting the maximum of the first sidelobe is $d = 4.05\lambda$,

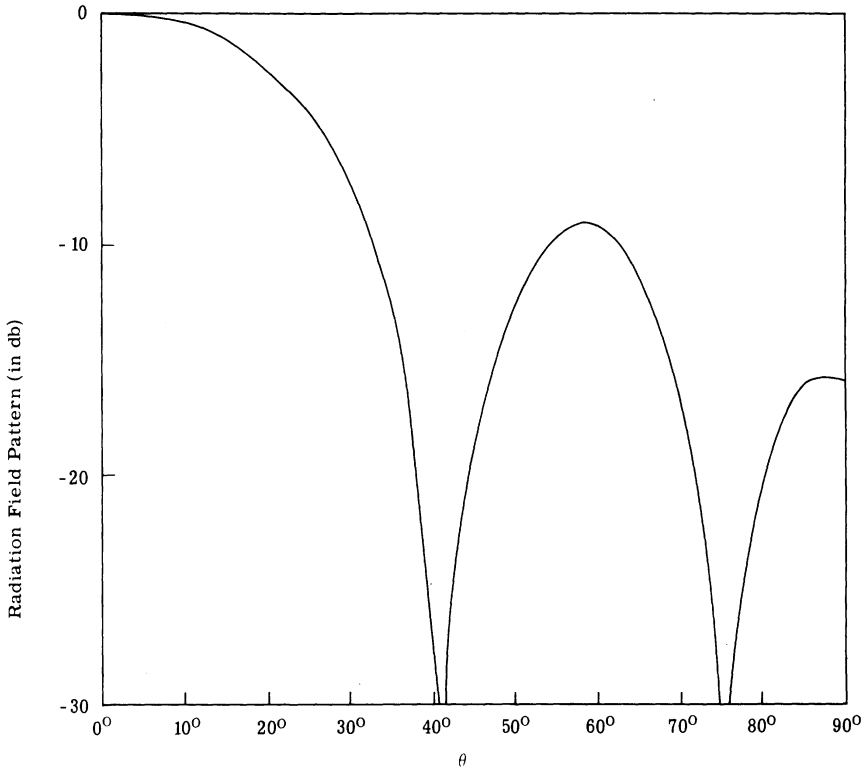

(a)

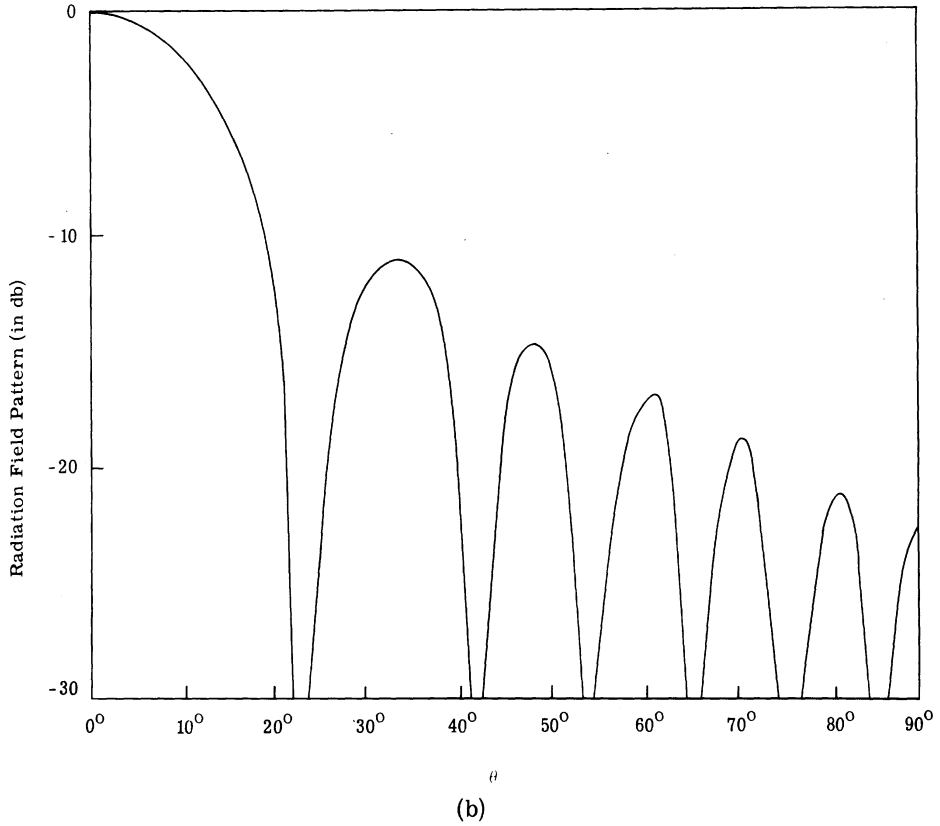

(b)

Fig. 31. Radiation patterns for dielectric rods.
(a) Rod length L = 2λ, c/v = 1.25.
(b) Rod length L = 6λ, c/v = 1.08.

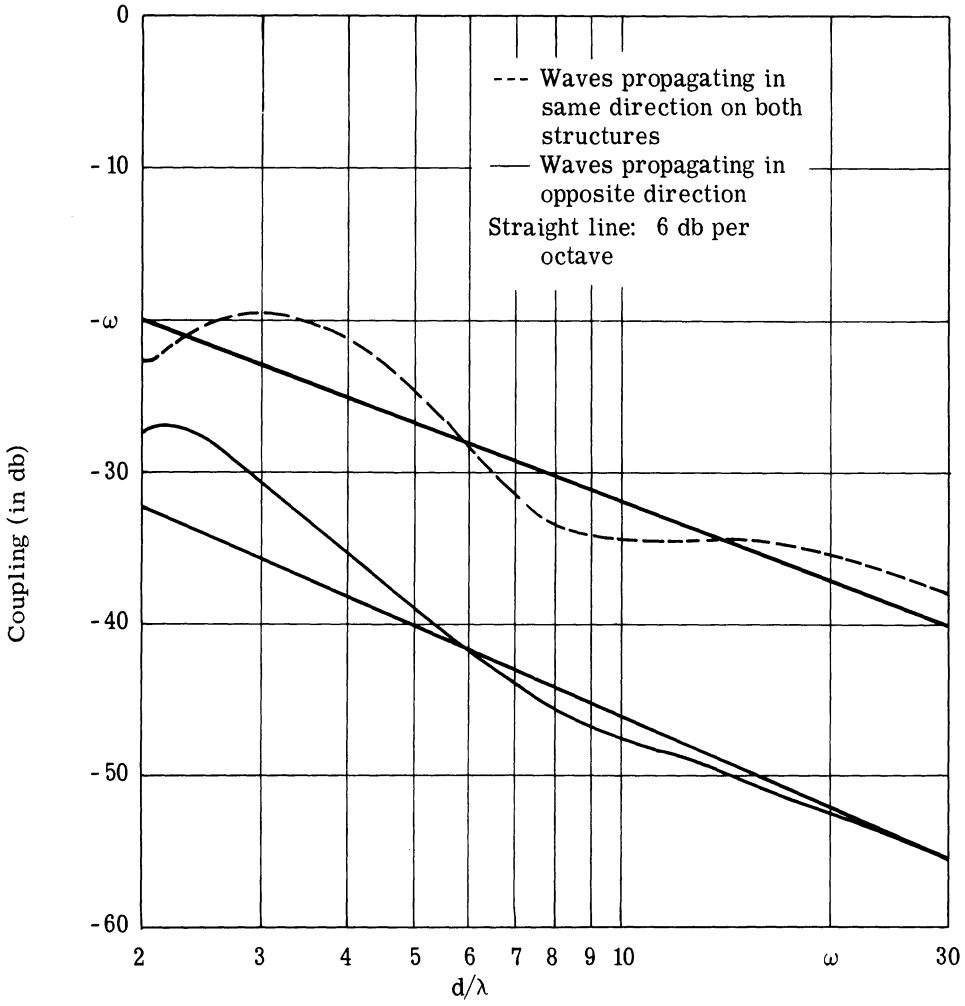

Fig. 32(a). Coupling versus spacing for two dielectric rods of equal length. Rod length L = 2λ, c/v = 1.25.

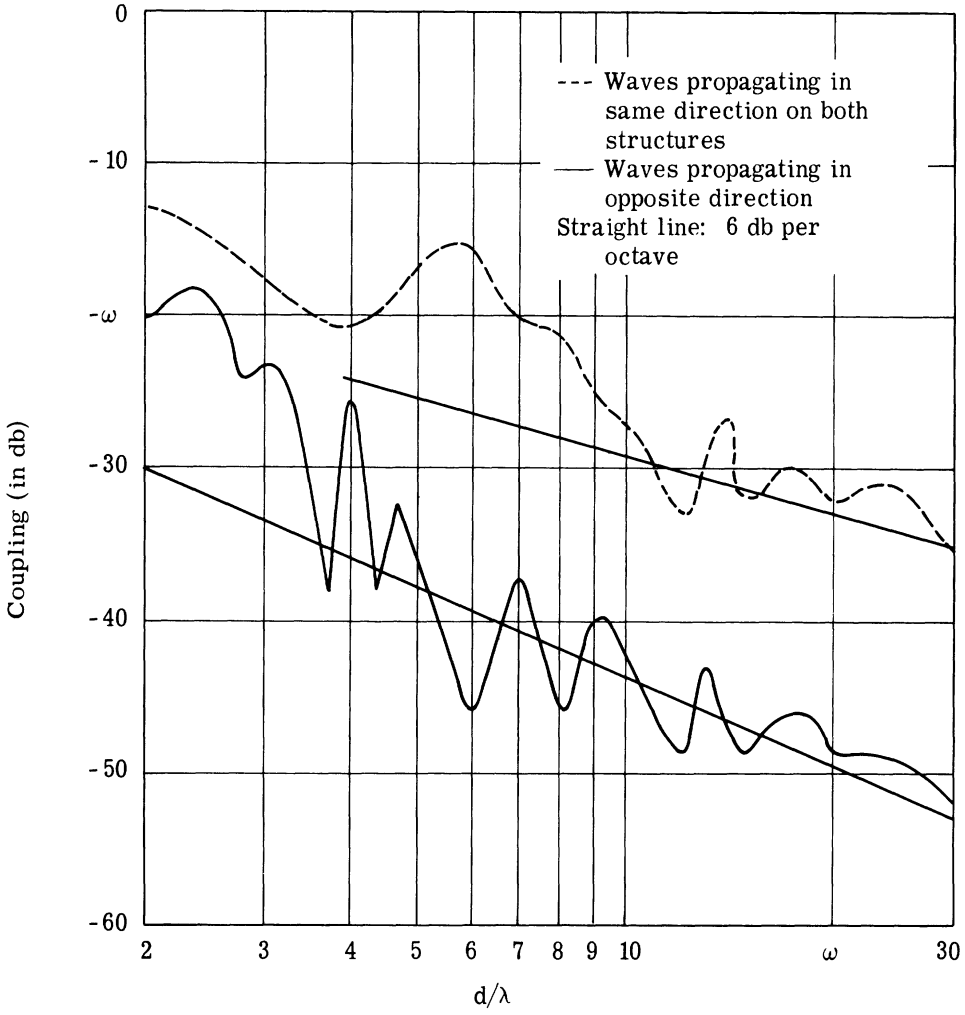

Fig. 32(b). Coupling versus spacing for two dielectric rods of equal length. Rod length L = 6λ, c/v = 1.08.

the spacing corresponding to the interception of the next-to-the-last sidelobe maximum is $d = 38\lambda$. At spacings in the neighborhood of 4λ considerable variations in the coupling factor occur, mainly as a result of contributions due to the first sidelobe. As the spacing increases, the interference effect of the sidelobes can be observed. The deviations from the 6-db line become smaller and smaller for larger spacings due to two factors. First of all, the amplitude of the sidelobe levels is decreasing as the angle θ is increasing. Secondly, the number of sidelobes intercepted by the receiving antenna decreases as the distance d between rods increases.

A final warning should be given about generalizing the results presented to other cases. Since both the radiation pattern and the integral producing the coupling are strongly dependent on **L**, β_t and β_r, the final result is very sensitive to variations in any of the parameters.

4. SPIRAL ANTENNA DATA TAKEN AT HARMONIC FREQUENCIES

Data were taken on both square and circular spirals at harmonics of the normal operating frequencies. The most significant data are included in this report. All the measurements were taken in the large anechoic chamber with the spirals mounted in a 12 ft. x 12 ft. ground plane.

Two patterns of the fabricated spiral "W.R." as described in Section 3.2.4 with the arms fed out-of-phase ($\beta = 0^{o}$) are shown in Fig. 33. Note especially that in Fig. 33(b), the effect of the current phase variations is to introduce beam-cock. Many patterns were taken on the fabricated "W.R." spiral with both in-phase ($\beta = 180^{o}$) and out-of-phase ($\beta = 0^{o}$) currents, but the two curves shown are illustrative.

Some representative patterns of the square spiral "1L" are given in Fig. 35. The patterns indicate not only the presence of higher order current distribution at harmonic frequencies, but the lack of symmetry indicates that the balun does not feed equal out-of-phase currents to the arms of the spiral above the design band (2 - 4 gc).

Figure 34 gives some representative patterns of the circular spiral "A". The minimum of E_{θ} near $\theta = 0$ at 5 gc indicates the presence of some third harmonic current distribution. As in Fig. 35, the patterns tend to become less symmetric at the higher frequencies, due to the effect of the balun.

Coupling patterns in the ground plane were taken for both the square spiral "1L" and the circular spiral "A" at frequencies between 8 and 10 gc. These patterns are not included here, but in general they can be described as follows:

The coupling patterns for the circular spiral have from three to five maxima irregularly spaced. The ratio of absolute maximum to absolute minimum coupling varies from 15 to 25 db.

The coupling patterns for the square spiral have from five to seven maxima irregularly spaced. The ratio of absolute maximum to absolute minimum is greater than that for the circular spiral, since there are either one or three very deep nulls in many of the patterns.

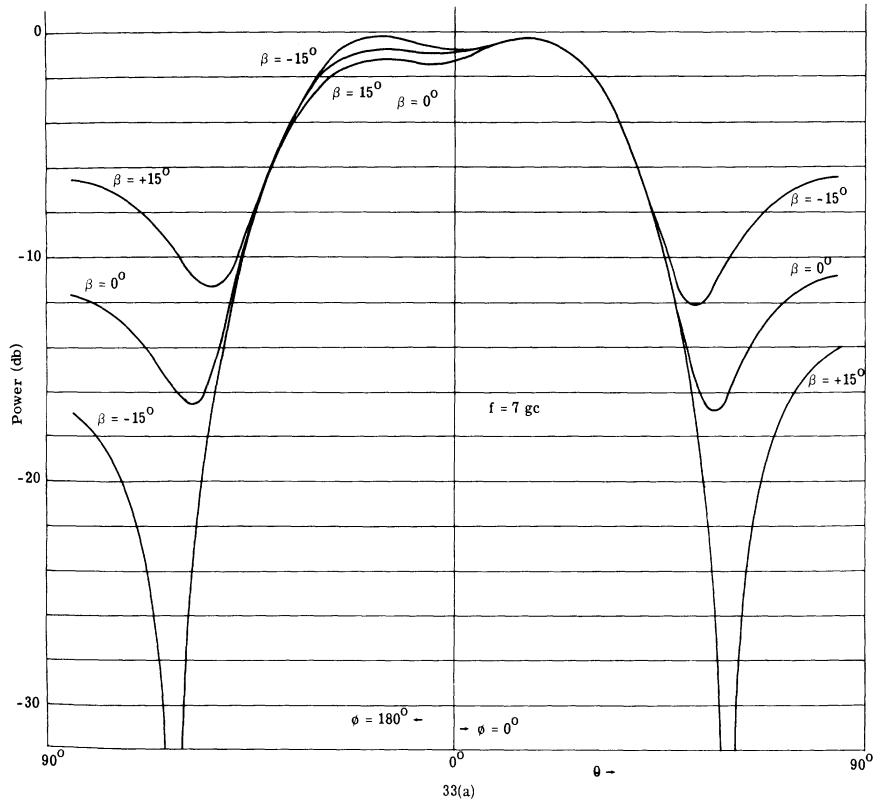

33(a)

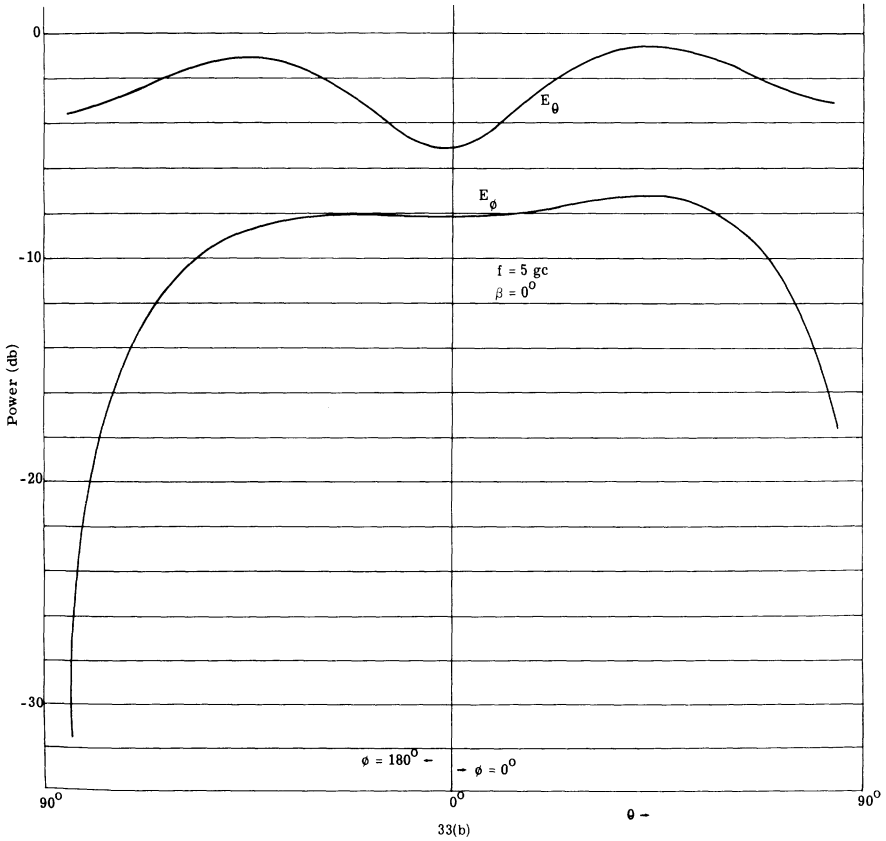

33(b)

Fig. 33. Harmonic radiation patterns for Fabricated Spiral "WR".

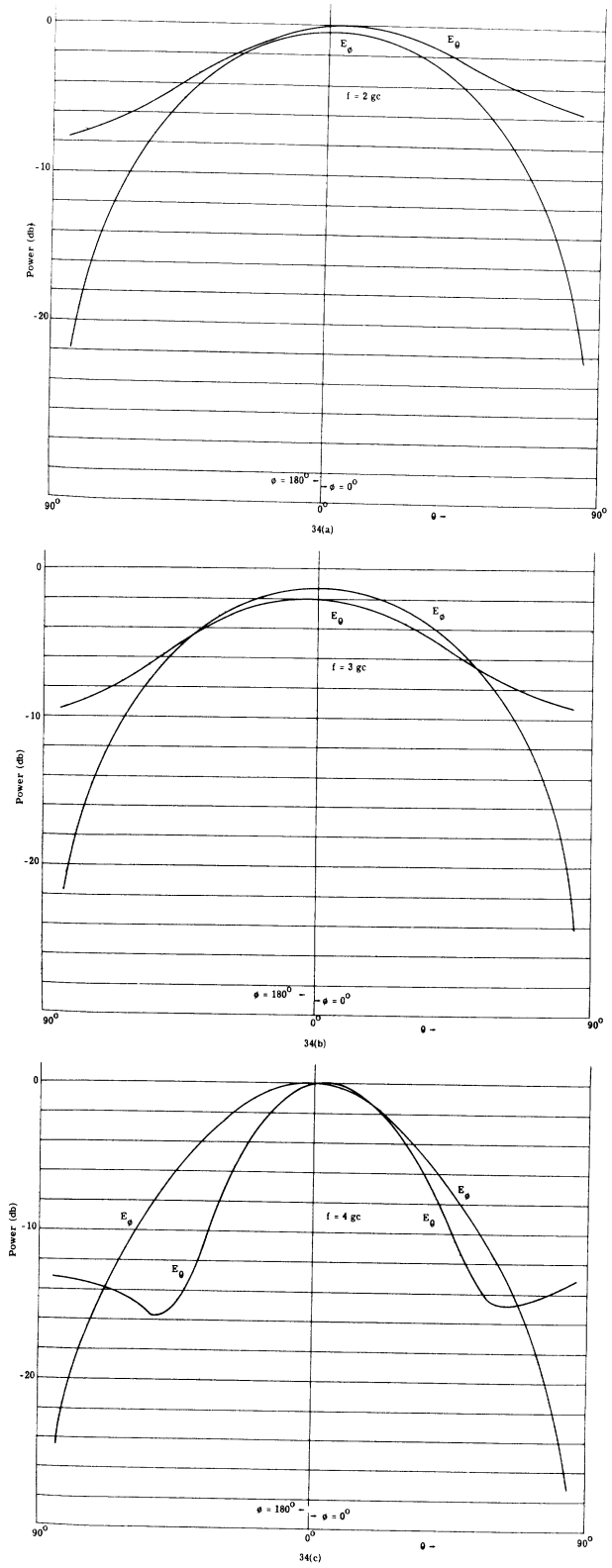

Fig. 34. Harmonic radiation patterns for Circular Spiral "A".

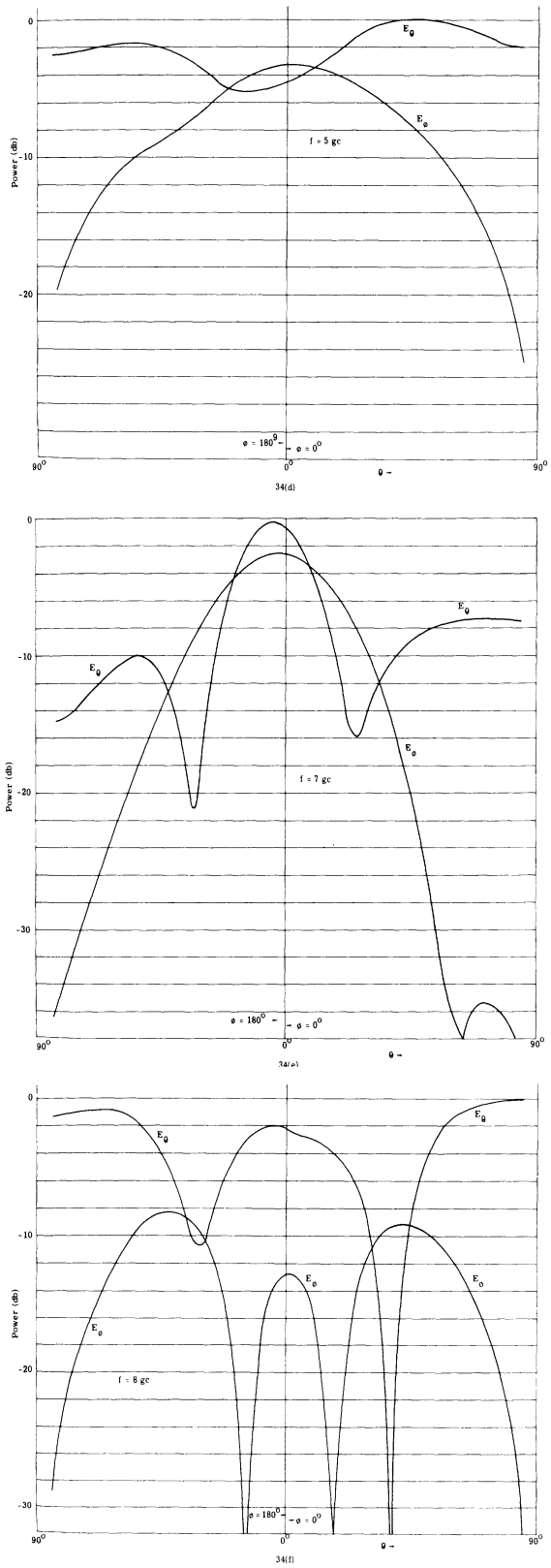

Fig. 34 (Cont.). Harmonic radiation patterns for Circular Spiral "A".

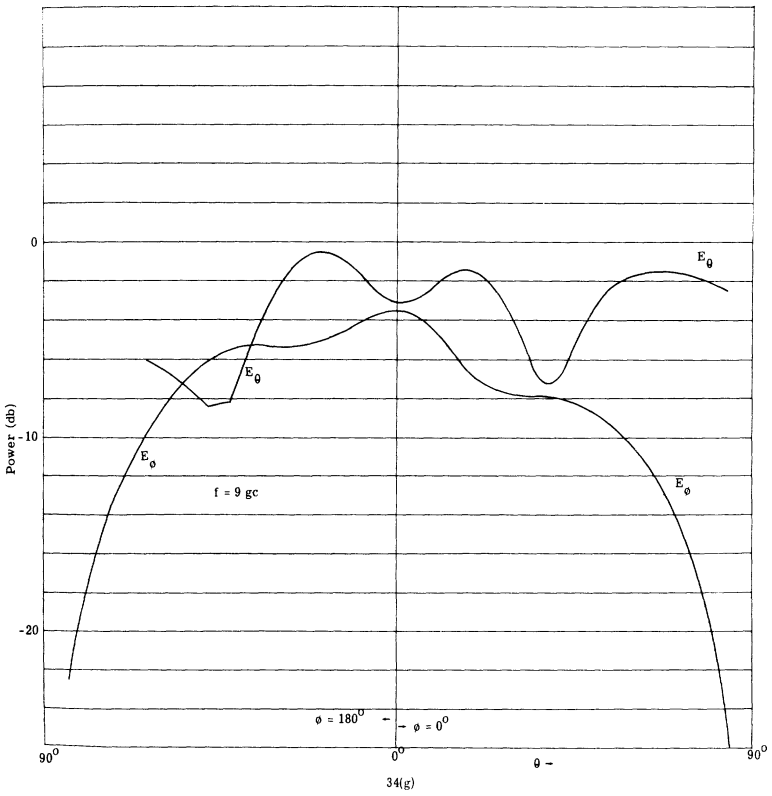

34(g)

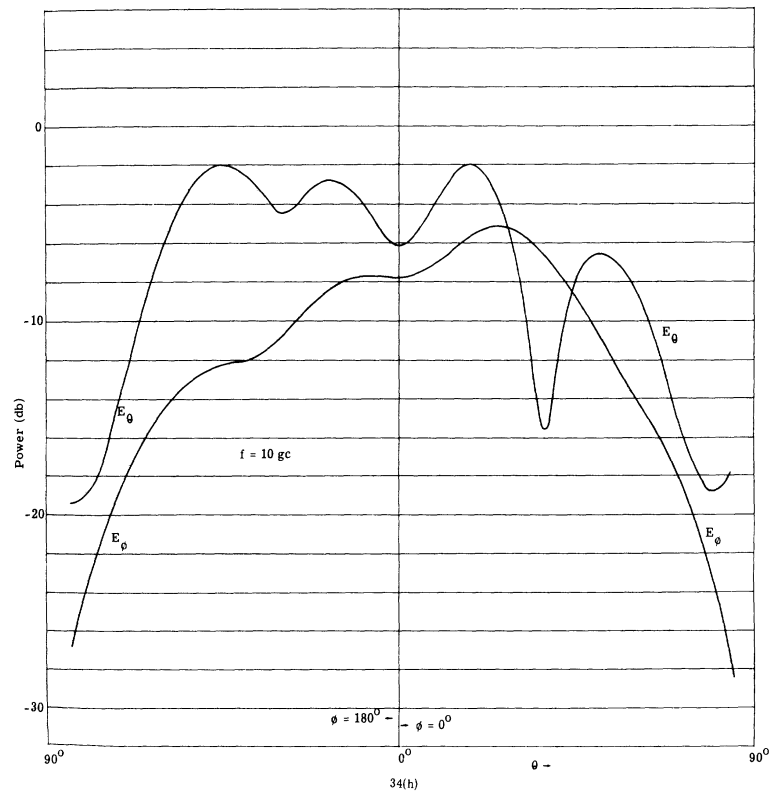

34(h)

Fig. 34 (Cont.) Harmonic radiation patterns for Circular Spiral "A".

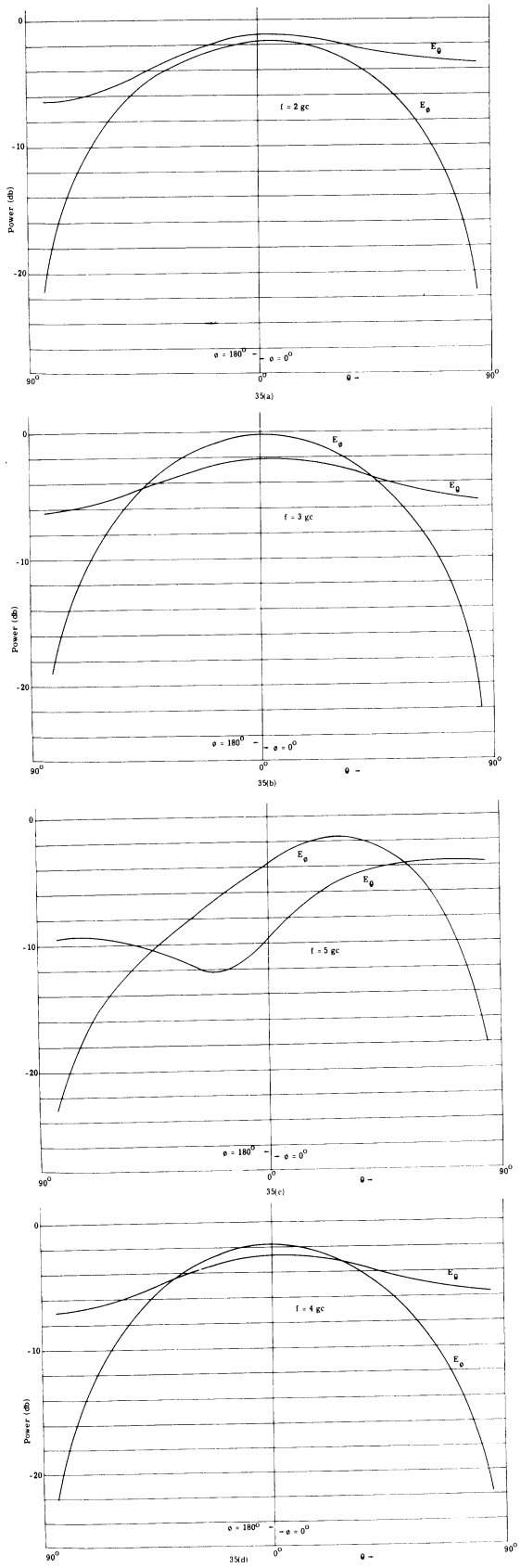

Fig. 35. Harmonic radiation patterns for Square Spiral "1L".

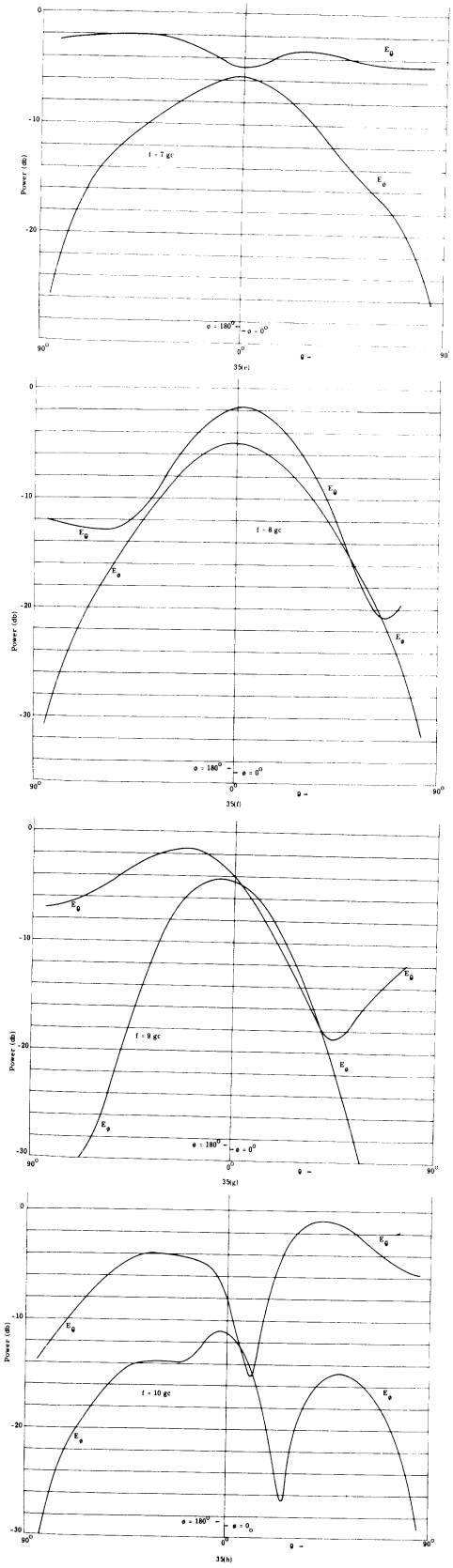

Fig. 35 (Cont.). Harmonic radiation patterns for Square Spiral "1L".

5. EFFECTS OF SKIN CURVATURE ON COUPLING

Under certain conditions which are met in a number of aerospace configurations, the effect of a curved conducting skin on the coupling between two antennas along the skin can be calculated knowing the flat-plane coupling between the same antennas and the geometry of the skin. These conditions are:

1. The diameter of the skin is greater than about two wavelengths.
2. The curvature in the region of the antenna is small.
3. The Fresnel-zone boundary is smaller than the radius of curvature.

These restrictions can be relaxed and still yield good results.

The problem was formulated in cylindrical coordinates but is valid for spherical geometries, or any geometry where the radius of curvature along the ray path between the two antennas is constant. The chief reference on this work is by Hasserjian and Ishimaru (Ref. 8). Their approach can be extended to treat other than thin resonant slots, indicated in Ref. 9 along with an outline of their method.

Procedure for Calculating Curvature Effect

Under the conditions listed above, the coupling between antennas T and R (see Fig. 36) on a cylinder of radius "a" can be calculated by multiplying the flat-plate coupling by the factor f(y), where

$$y = \frac{ka\phi^2}{\sqrt{kr_s}}$$

$r_s = \sqrt{z^2 + a^2\phi^2}$ = distance from T to R along the surface

f(y) is given below, and in Fig. 37.

The flat-surface coupling is the coupling of T and R separated by r_s along a conducting plane.

It is first necessary to calculate y. Several alternative forms are given below for convenience.

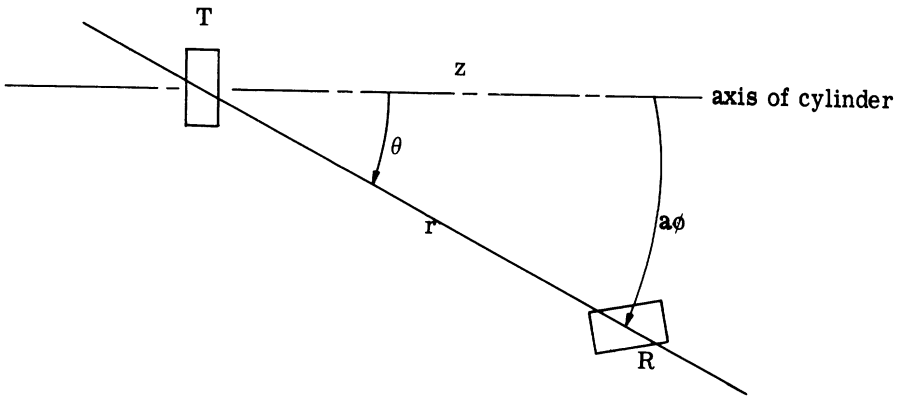

Fig. 36. Geometry of two slots on a cylinder.

Cylinder:

$$y = \begin{cases} \dfrac{(kr_s)^{3/2}\sin^2\theta}{ka} = \dfrac{2.507\, r_s^{3/2}\sin^2\theta}{2\sqrt{\lambda}} \\ \dfrac{ka\,\phi^2\,(\text{radians})}{kr_s} = \dfrac{2.507\, a\,\phi^2\,(\text{radians})}{\lambda\, r_s} \end{cases}$$

$$r_s = \begin{cases} z^2 + (a\phi)^2 \\ \dfrac{a\phi}{\sin\theta} \\ \dfrac{z}{\cos\theta} \end{cases}$$

Sphere:

$$y = \sqrt{ka}\;\phi^{3/2}\,(\text{radians})$$

$$r_s = a\phi$$

where ϕ is the angle between the antennas on a plane defined by the two antennas and the center of the sphere.

f(y) is analytically expressed by

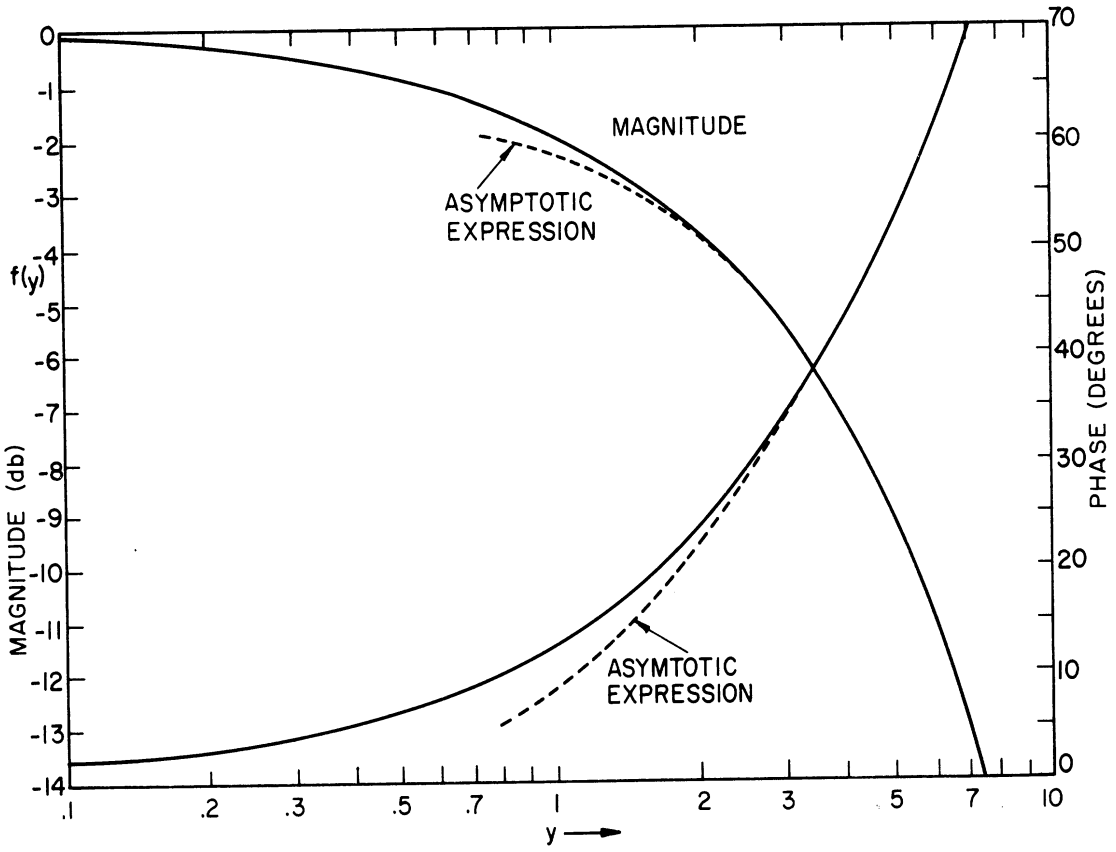

Fig. 37(a). Curvature factor f(y) vs. y (low range).

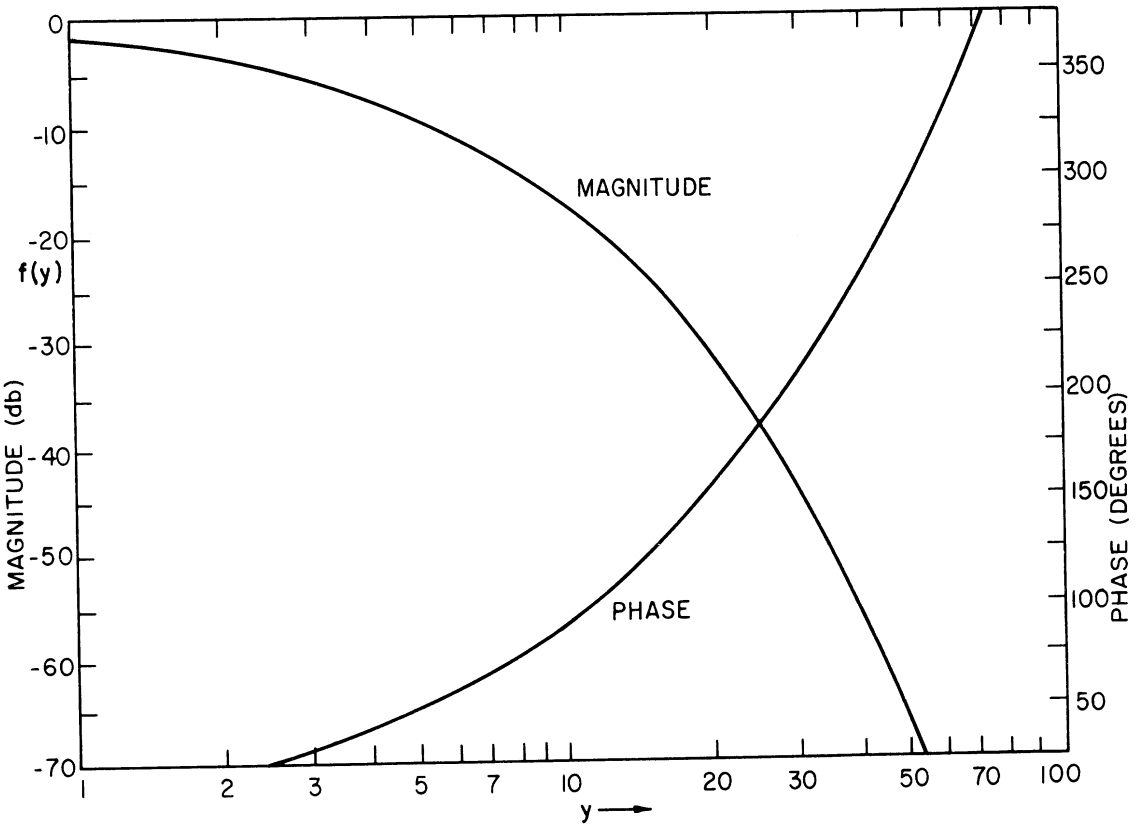

Fig. 37(b). Curvature factor f(y) vs. y (high range).

$$f(y) = \begin{cases} 1 - e^{j\pi/4}\sqrt{\frac{\pi}{2}}\,\frac{y}{4} + \frac{7j\,y^2}{120}\,\sqrt{\frac{\pi}{2}}\,e^{j\pi/4}\,\frac{y^3}{1024} \cdots, & \phi \text{ small} \\ e^{-j\pi/4}\sqrt{\pi}\left(\frac{y}{\sqrt{2}}\right)\sum_{m=1}^{\infty}\frac{\exp\left[-j\left(\frac{y}{\sqrt{2}}\right)^{2/3} t_m\right]}{t_m}, & \phi \text{ not small} \end{cases}$$

where

$$t_1 = 1.019^{-j\pi/3}$$

$$t_2 = 3.248\, e^{-j\pi/3}$$

$$t_3 = 4.820\, e^{-j\pi/3}$$

$$t_4 = 6.163\, e^{-j\pi/3}$$

$$t_5 = 7.372\, e^{-j\pi/3}$$

For large values of y, only the first term need be considered, and the asymptotic approximation holds:

$$|f(y)| \simeq 1.550\, y^{1/3}\, e^{-.7005\, y^{2/3}}$$

$$|f(y)|_{db} = 8.686\left[\frac{1}{3}\log_e y + .4380 - .7005\, y^{2/3}\right] \text{ db}$$

$$= 20\left[\frac{1}{3}\log_{10} y + .1902 - .3042\, y^{2/3}\right] \text{ db}$$

and the phase lag over the flat plate value is given by

$$\text{Phase}\,[f(y)] = .4045\, y^{2/3} - .2618 \text{ radians}$$

$$= 23.18\, y^{2/3} - 15. \text{ degrees} .$$

The curves for f(y) are shown in Fig. 37.

The error introduced by using this expression is less than 0.5 percent in the magnitude for $y \geq 2$, and in the phase for $y \geq 4$. The latter terms of the series rapidly become more negligible as y increases.

To a first approximation, then, it is necessary to reduce the coupling found by

"flattening" the cylinder into a plane by the curvature factor $|f(y)|$. As the curvature goes to zero, y approaches zero and $|f(y)|$ approaches unity.

Whenever more than one ray path may contribute significantly to the coupling, modification of the above procedure is necessary. While in theory there are an infinite number of paths corresponding to multiple encirclements of the cylinder, for the region of interest ($a \geq 2\lambda$) all except the two paths where $\phi < 360^{o}$ yield terms on the order of 70 db below the latter. Thus the modification need only be extended to treat two ray paths. The waves will interfere or reinforce according to the relative phase. In no case will the reinforcement be greater than 6 db over one path alone.

APPENDIX A

RELATION BETWEEN COUPLING AND MUTUAL IMPEDANCE

Consider the general linear two-port network depicted in Fig. 38.

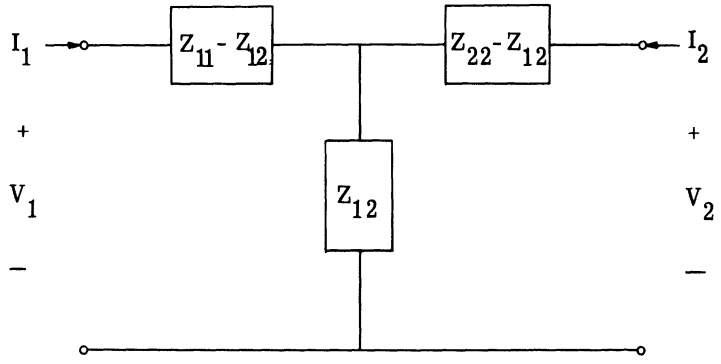

Fig. 38. Two-port network.

The network equations are:

$$V_1 = Z_{11} I_1 + Z_{12} I_2$$
$$V_2 = Z_{21} I_1 + Z_{22} I_2 \ . \qquad \text{(A. 1)}$$

Since antenna pairs are generally linear and reciprocal,

$$Z_{12} = Z_{21} \quad \text{(mutual impedance)} \ . \qquad \text{(A. 2)}$$

Furthermore, for far-field coupling, we see that

$$|Z_{12}| << |Z_{11}|$$
$$|Z_{12}| << |Z_{22}| \ .$$

The power transmitted is:

$$W_t = I_1^2 \, \mathrm{Re}\,(Z_{11}) \, .$$

The power received by a matched load is:

$$W_r = I_2^2 \, \mathrm{Re}\,(Z_{22}) = \frac{I_1^2 \, |Z_{12}|^2}{4 \, \mathrm{Re}\,(Z_{22})} \, .$$

Thus the far-field coupling is:

$$C = \frac{W_r}{W_t} = \frac{|Z_{12}|^2}{4 \, R_{11} \, R_{22}} \tag{A.3}$$

where

$$R_{11} = \mathrm{Re}\,(Z_{11})$$
$$R_{22} = \mathrm{Re}\,(Z_{22}) \, .$$

Mutual impedance is obtained from an open-circuit measurement, whereas coupling is obtained from a tuned measurement.

$$Z_{12} = \left. \frac{V_2}{I_1} \right|_{\substack{\text{receiver} \\ \text{open-circuited}}} \tag{A.4}$$

The loading that occurs in near-field situations will alter the relation given by Eq. A.4.

APPENDIX B

SLOT COUPLING THEORY

In terms of a complete orthonormal set of transverse vector mode functions, the transverse field in the waveguide region may be represented as

$$\begin{aligned} \bar{E}(x,y) &= V_1(z)\,\bar{e}_1(x,y) + \sum_i{}' V_i(z)\,\bar{e}_i(x,y) \\ \bar{H}(x,y) &= I_1(z)\,\bar{h}_1(x,y) + \sum_i{}' I_i(z)\,\bar{h}_i(x,y)\ . \end{aligned} \tag{B.1}$$

The subscript 1 identifies the dominant TE_{10}-mode in rectangular guide; the summation is to be taken over all modes except the dominant one. Both $\bar{e}_i$ and $\bar{h}_i$ are chosen so as to satisfy orthogonality requirements:

$$\begin{aligned} \int\int (\bar{e}_i \cdot \bar{e}_j)\, dS &= \delta_{ij} \\ \int\int (\bar{h}_i \cdot \bar{h}_j)\, dS &= \delta_{ij}\ , \end{aligned} \tag{B.2}$$

the surface integrals being extended over the guide cross-section. This orthonormality property leads to:

$$\begin{aligned} V_i(z) &= \int\int \bar{E} \cdot \bar{e}_i\, dA \\ I_i(z) &= \int\int \bar{H} \cdot \bar{h}_i\, dA\ . \end{aligned} \tag{B.3}$$

For the geometry shown in Fig. 39, the dominant amplitude in guide B (receiving guide) is given by (see Ref. 10)

$$\begin{aligned} I_1 = &\int_R\int \int_T\int \bar{h}_i(\bar{\rho}_r) \cdot \bar{\bar{Y}}(\bar{R}_t,\bar{\rho}_t) \cdot [\hat{n} \times \bar{E}_t(\bar{\rho}_t)]\, dA_t\, dA_r \\ &+ \int_R\int \int_R\int \bar{h}_i(\bar{\rho}_r) \cdot \bar{\bar{Y}}(\bar{R}_r,\bar{\rho}_r) \cdot [\hat{n} \times \bar{E}_r(\bar{\rho}_r)]\, dA_r\, dA_r \end{aligned} \tag{B.4}$$

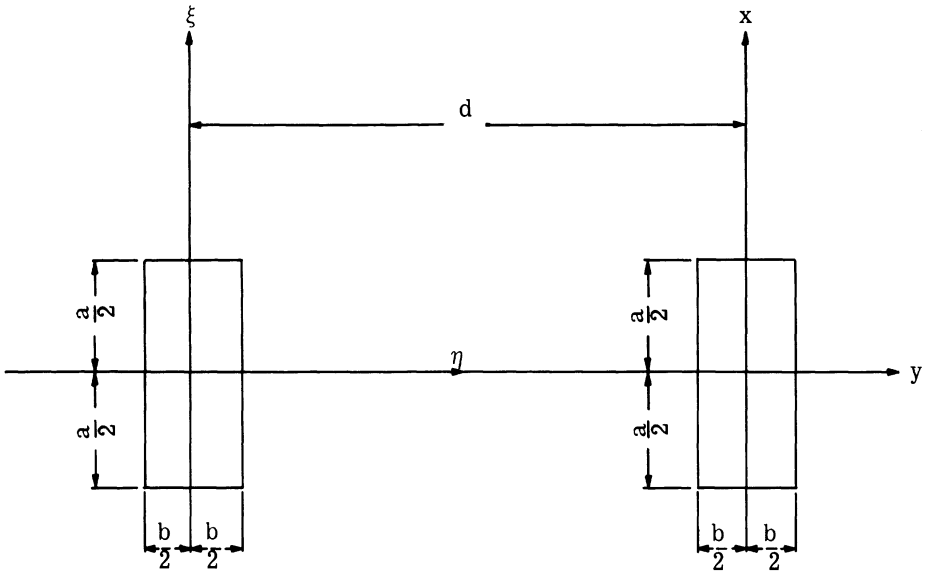

Fig. 39. Coupling geometry for two close slots.

where $\hat{n}$ is a unit vector normal to the plane.

$\bar{\rho}_t$ and $\bar{\rho}_r$ are the source coordinates at the apertures A and B, respectively.

$$\bar{\bar{Y}}(\bar{R}_t, \bar{\rho}_t) = \frac{j\omega\epsilon}{2\pi}\left(\bar{\bar{I}} + \frac{\nabla\nabla}{k^2}\right)\frac{e^{-jk|\bar{r}_t|}}{|\bar{r}_t|}$$

$$\bar{\bar{Y}}(\bar{R}_r, \bar{\rho}_r) = \frac{j\omega\epsilon}{2\pi}\left(\bar{\bar{I}} + \frac{\nabla\nabla}{k^2}\right)\frac{e^{-jk|\bar{r}_r|}}{|\bar{r}_r|} \qquad \text{(B. 5)}$$

$\bar{r}_t$ and $\bar{r}_r$ are the same field point in terms of coordinate systems (ξ, η, ζ) and (x, y, z), respectively. In the first approximation, the scattering-term [the second term in Eq. B. 4] is ignored. This approximation amounts to the assumption that the electric field on R is not disturbed by the introduction of the slot in the perfectly conducting plane. It is further assumed that

$$\bar{E}_T(\bar{\rho}_T) = \hat{\eta}\, E_o \cos\frac{\pi\xi}{a}, \quad -\frac{a}{2} < \xi < \frac{a}{2} .$$

Broadside Coupling of Two Identical Waveguides (see Fig. 39)

The method of computing the coupling between two rectangular slots is outlined here.

$$I_1 = \sqrt{\frac{2}{ab}}\ \frac{E_o}{2\pi j\omega\mu}\ \int_{-a/2}^{a/2} dx \int_{-b/2}^{b/2} dy \int_{-a/2}^{a/2} d\xi' \int_{-b/2}^{b/2} \left\{ \left[\cos\frac{\pi x}{a} \cos\frac{\pi \xi'}{a} \right] \right.$$

$$\left. \left(k^2 + \frac{\partial^2}{\partial z^2} \right) \frac{e^{-jk\sqrt{(\xi-\xi')^2 + (\eta-\eta')^2}}}{\sqrt{(\xi-\xi')^2 + (\eta-\eta')^2}} \right\} d\eta'$$

By setting

$$\xi = x$$

$$\eta = y + d$$

and after performing some algebraic operations, one obtains (Ref. 10)

$$I_1 = \sqrt{\frac{2}{ab}}\ \frac{E_o}{2\pi j\omega\mu}\ k^2 \left(\frac{a}{\pi}\right)^3 K_1$$

where

$$K_1 = \int_{\frac{\pi(d-b)}{a}}^{\frac{\pi(d+b)}{a}} du \left[\frac{\pi b}{a} - \left| u - \frac{\pi d}{a} \right| \right] \int_0^{\pi} \left[\left(1 - \frac{\pi^2}{k^2a^2}\right) (\pi - v) \cos v \right.$$

$$\left. + \left(1 + \frac{\pi^2}{k^2a^2}\right) \sin v \right] \frac{e^{-j\frac{ka}{\pi}\sqrt{u^2+v^2}}}{\sqrt{u^2+v^2}}\ dv$$

$$= \alpha_1 + j\beta_1 \ .$$

The values of $K_1 = \alpha_1 + j\beta_1$ for different d have been evaluated on the IBM 7090 computer.

The total power received at the receiving guide R is

$$W_r = \frac{1}{2}\ \frac{|I_1|^2}{Y_{10}} = \sqrt{\frac{\epsilon}{\mu}}\ E_o^2\ \frac{k^2a^2}{4\pi^8} \left(\frac{a}{b}\right)^2 (ab)\ |K_1|^2 \cdot \frac{1}{\sqrt{1 - \left(\frac{\pi}{ka}\right)^2}} \ .$$

The power transmitted from the slot T was derived in Ref. 11 and can be written as

$$W_t = \mathrm{Re}\left\{ \frac{E_o^2}{\pi j \omega \mu} k^2 \left(\frac{a}{\pi}\right)^3 (\gamma_1 - j\delta_1) \right\}$$

$$= \frac{ka^3}{\pi^4} E_o^2 \sqrt{\frac{\epsilon}{\mu}} (-\delta_1)$$

where

$$\gamma_1 + j\delta_1 = \int_0^{\frac{\pi b}{a}} \left(\frac{\pi b}{a} - \mu\right) du \int_0^{\pi} \left\{ \left(1 - \frac{\pi^2}{k^2 a^2}\right) (\pi - v) \cos v \right\}$$

$$+ \left\{ \left(1 + \frac{\pi^2}{k^2 a^2}\right) \sin v \right\} \frac{e^{-j \frac{ka}{\pi} \sqrt{u^2 + v^2}}}{\sqrt{u^2 + v^2}} \, dv \, .$$

This integral is evaluated for a wavelength of 1.283", a = 0.9" and b = 0.4". The results are

$$\gamma_1 = 1.424598$$

$$\delta_1 = 2.697506$$

The coupling C is expressed by

$$C = \frac{W_r}{W_t}$$

or

$$C = \frac{ka}{4\pi^4} \left(\frac{a}{b}\right) \frac{1}{(-\delta_1)\sqrt{1 - \frac{\pi^2}{k^2 a^2}}} |K_1|^2 \, .$$

APPENDIX C

DERIVATION OF SQUARE SPIRAL FIELDS

In this section the radiation fields of the square spiral antenna are derived. The antenna is assumed to be made up of a series of linear wire elements arranged in a configuration similar to that of the square spiral (see Fig. 40). Each wire carries a traveling wave of current. The phase of each current is the same as the phase of the corresponding current on the spiral. The magnitude of the current on each wire element is held constant, and attenuation, due to radiation, is depicted by reducing the current magnitude on successive wire elements in each leg of the spiral. If one assumes a constant magnitude current on each wire element, the vector potential may be calculated.

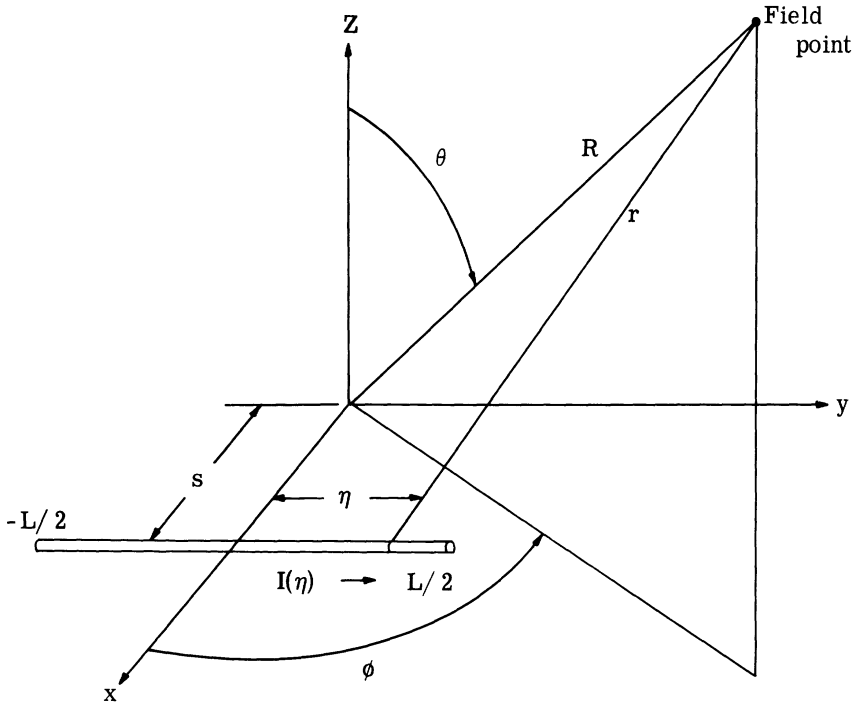

Fig. 40. Geometry for square spiral analysis.

The vector potential due to a traveling wave of current on a linear wire element displaced a distance s from the origin is found as follows. For a y-directed wire (Fig. 39), the vector potential at a large distance r from the wire is given by

$$A_y = \frac{1}{4\pi R} \int_{-1/2}^{1/2} I(\eta)\, e^{-jkr}\, d\eta' \,. \tag{C.1}$$

If R is large compared to a wavelength, r is given approximately by

$$r = R - \eta \sin\phi \sin\theta - s \cos\phi \sin\theta \,.$$

The current is assumed to have the form

$$I(\eta) = I_o\, e^{-j\beta(\eta + \ell)} \tag{C.2}$$

where the factor $-j\beta\ell$ will be used later to adjust the relative phase between currents on different wires.

Equation C. 1 now becomes

$$A_y = \frac{e^{-jkR}}{4\pi R} \int_{-\frac{L}{2}}^{\frac{L}{2}} I_o\, e^{-j\beta(\eta+\ell)}\, e^{jk(\eta \sin\phi \sin\theta + s\cos\phi \sin\theta)}\, d\eta$$

or

$$A_y = \frac{I_o\, e^{-j(kR + \beta\ell - ks\cos\phi \sin\theta)}}{4\pi R} \int_{-\frac{L}{2}}^{\frac{L}{2}} e^{j(k \sin\theta \sin\phi - \beta)\eta}\, d\eta \,.$$

After integrating and combining the two resulting exponentials into a sine term, one obtains

$$A_y = \frac{I_o\, e^{-j(kR + \beta\ell - ks\cos\phi \sin\theta)}}{2\pi R[\beta - k \sin\theta \sin\phi]} \sin\frac{L}{2}[\beta - k \sin\theta \sin\phi] \tag{C.3}$$

where

s = the distance the element is displaced from the origin

L = the length of the element

β = propagation constant for current wave

k = propagation constant for waves in space (air).

In a similar manner, the vector potential due to a traveling wave of current on an x-directed wire is given by

$$A_x = \frac{I_o\, e^{-j(kR + \beta\ell - ks\cos\phi\sin\theta)}}{2\pi R[\beta - k\sin\theta\cos\phi]} \sin\frac{L}{2}[\beta - k\sin\theta\cos\phi] \,. \qquad (C.4)$$

In order to apply these results to the case of the square spiral, an approximation to the square spiral geometry must be made. It may be seen, in Fig. 41(b), that the geometry of the square spiral can be divided into four triangular regions and one small square region by drawing four lines which pass through the corners of the wires. If the four triangular regions are now translated so that the vertices of the triangles (points a_1, a_2, a_3, and a_4) are positioned at the same point "a" in space, the geometry of Fig. 41(b) results.

Note that this translation has eliminated the small square region at the center of the spiral. The relative translation between diametrically opposite triangles is equal to the length of the diagonal of this small square region. Since the diagonal length is equal to the spacing between the spiral wires, the translation will be small if the wires are spaced very closely together.

The geometry in Fig. 41(b) is more easily analyzed since each wire element is geometrically symmetric with respect to the axis it crosses. The current on each element in Fig. 41(b) will be assumed to be the same as on the corresponding element in Fig. 41(a).

The total vector potential for the spiral antenna may now be found by summing the contributions due to each wire element. Equations C.3 and C.4 will be altered for use in these summations.

Performance of these summations requires consideration of the direction of propagation of the current wave on each wire element. In Fig. 41(b), the current waves on

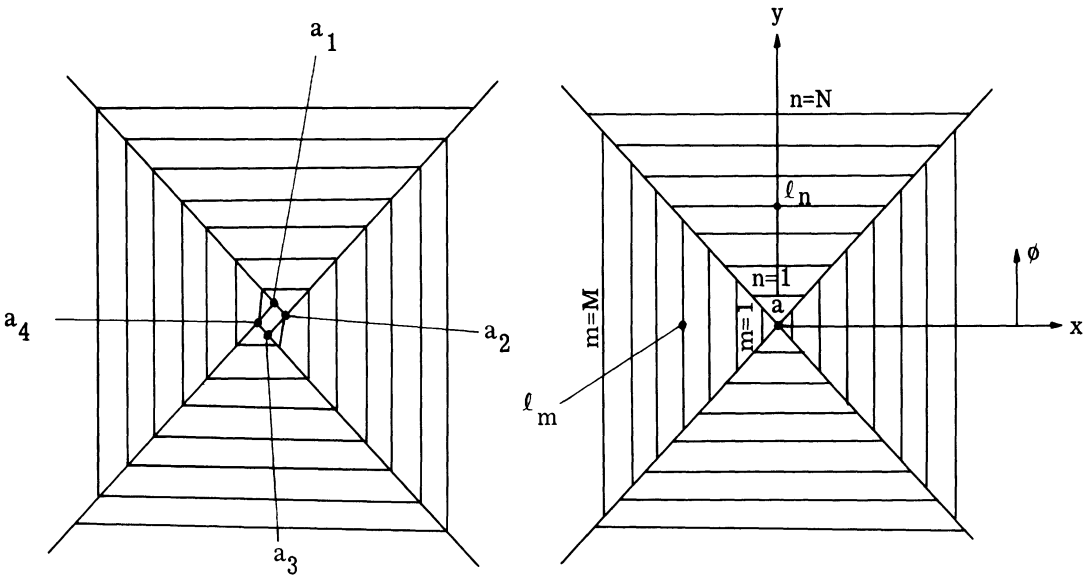

Fig. 41. Square spiral configuration.

the y-directed elements crossing the positive x-axis travel in the negative y-direction (downward). However, the waves on the elements crossing the negative x-axis travel in the positive y-direction (upward). This difference in the directions of wave propagation on y-directed elements may be considered in the y-component of the total vector potential by changing the sign of β (except in the exponential term) in Eq. C.3 when it is used for components crossing the negative x-axis. Similar considerations must be made in Eq. C.4.

The relative phase between currents on all elements must also be considered in performing the summation, hence, the factor $-j\beta\ell$. This factor may be used to adjust the phase of the current at the center of the wire element being considered. It is easily seen from Eq. C.2 that if the phase of the current at the center of the wire ($\eta = 0$) is correctly chosen, then the phase of the current at other positions along the wire ($|\eta| > 0$) will also be correct. The factor $-j\beta\ell$ will give the correct phase at the center of each wire element if ℓ is defined as the length of the spiral leg from its beginning at the center of the spiral out to the center of the element being considered. With ℓ defined in this manner, the current at the center of the m^{th} y-directed wire element is given by

$$I_m = (-1)^{m+1} |I_m| e^{-j\beta\ell_m} ,$$

where m = 1 designates the first y-directed wire element to the right (or left) of the origin and m = M designates the y-directed element farthest to the right (or left) of the origin (see Fig. 41(b). The factor $(-1)^{m+1}$ accounts for the out-of-phase feed at the center of the spiral. Similarly, for x-directed elements, the current at the center of the n^{th} element is

$$I_n = (-1)^{n+1} |I_n| e^{-j\beta\ell_n}$$

The only remaining alteration of Eqs. C.3 and C.4 needed to make them applicable to the spiral antenna is to change the sign of "s" (element displacement from origin) for elements crossing negative axes.

With the above alterations of Eqs. C.3 and C.4 taken into account, expressions for the total vector potentials in the x and y directions, respectively, may be formulated and are given by:

$$A_x = \sum_{n=1}^{N} (-1)^{n+1} \frac{I_n e^{-j(kR + \beta\ell_n - ks_n \sin\theta \sin\phi)}}{2\pi R(\beta - k \sin\theta \cos\phi)} \sin\frac{L_n}{2}(\beta - k \sin\theta \cos\phi)$$

$$+ \sum_{n=1}^{N} (-1)^{n+1} \frac{I_n e^{-j(kR + \beta\ell_n - ks_n \sin\theta \sin\phi)}}{2\pi R(\beta + k \sin\theta \cos\phi)} \sin\frac{L_n}{2}(\beta + k \sin\theta \cos\phi) \quad \text{(C.5)}$$

and

$$A_y = -\sum_{m=1}^{M} (-1)^{m+1} \frac{I_m e^{-j(kR + \beta\ell_m - ks_m \cos\phi \sin\theta)}}{2\pi R(\beta + k \sin\theta \sin\phi)} \sin\frac{L_m}{2}(\beta + k \sin\theta \sin\phi)$$

$$- \sum_{m=1}^{M} (-1)^{m+1} \frac{I_m e^{-j(kR + \beta\ell_m - ks_m \sin\theta \sin\phi)}}{2\pi R(\beta - k \sin\theta \sin\phi)} \sin\frac{L_m}{2}(\beta - k \sin\theta \sin\phi) \quad \text{(C.6)}$$

where

I_m = magnitude of the current on the m^{th} element,

s_m = displacement of the m^{th} element from the origin,

L_m = length of the m^{th} element.

The total vector potential due to all currents on the spiral is then given by

$$\bar{A} = A_x \hat{x} + A_y \hat{y} \ . \tag{C.7}$$

$\bar{A}$ may be expressed in terms of spherical coordinates as follows:

$$\bar{A} = A_\theta \hat{\theta} + A_\phi \hat{\phi}$$

where

$$A_\theta = A_x \cos\phi \cos\theta + A_y \sin\phi \sin\theta \tag{C.8}$$

$$A_\phi = -A_x \sin\phi + A_y \cos\phi \ . \tag{C.9}$$

The electric fields are then given by:

$$E_\theta = -j\omega\mu A_\theta \tag{C.10}$$

$$E_\phi = -j\omega\mu A_\phi \ . \tag{C.11}$$

Performing the indicated operations produces the following expressions for E_θ and E_ϕ:

$$\begin{aligned} E_\theta = \frac{-j\omega\mu e^{-jkR}}{2\pi R} \Bigg[& \cos\phi\cos\theta \sum_{n=1}^{N} (-1)^{n+1} \frac{I_n e^{-j(\beta\ell_n - ks_n \sin\phi \sin\theta)}}{(\beta - k\sin\theta\cos\phi)} \sin\frac{L_n}{2}(\beta - k\sin\theta\cos\phi) \\ & + \cos\phi\cos\theta \sum_{n=1}^{N} (-1)^{n+1} \frac{I_n e^{-j(\beta\ell_n + ks_n \sin\theta \sin\phi)}}{(\beta + k\sin\theta\cos\phi)} \sin\frac{L_n}{2}(\beta + k\sin\theta\cos\phi) \\ & + \sin\phi\cos\theta \sum_{m=1}^{M} (-1)^{m+1} \frac{I_m e^{-j(\beta\ell_m - ks_m \cos\phi \sin\theta)}}{(\beta + k\sin\theta\sin\phi)} \sin\frac{L_m}{2}(\beta + k\sin\theta\sin\phi) \\ & + \sin\phi\cos\theta \sum_{m=1}^{M} (-1)^{m+1} \frac{I_m e^{-j(\beta\ell_m + ks_m \cos\phi \sin\theta)}}{(\beta - k\sin\theta\sin\phi)} \sin\frac{L_m}{2}(\beta - k\sin\theta\sin\phi) \Bigg] \end{aligned} \tag{C.12}$$

$$E_\phi = \frac{j\omega\mu e^{-jkR}}{2\pi R}\left[\sin\phi \sum_{n=1}^{N}(-1)^{n+1}\frac{I_n e^{-j(\beta\ell_n - ks_n \sin\phi\sin\theta)}}{(\beta - k\sin\theta\cos\phi)}\sin\frac{L_n}{2}(\beta - k\sin\theta\cos\phi)\right.$$

$$+ \sin\phi \sum_{n=1}^{N}(-1)^{n+1}\frac{I_n e^{-j(\beta\ell_n + ks_n \sin\theta\sin\phi)}}{(\beta + k\sin\theta\cos\phi)}\sin\frac{L_n}{2}(\beta + k\sin\theta\cos\phi)$$

$$+ \cos\phi \sum_{m=1}^{M}(-1)^{m+1}\frac{I_m e^{-j(\beta\ell_m - ks_m \cos\phi\sin\theta)}}{(\beta + k\sin\theta\sin\phi)}\sin\frac{L_m}{2}(\beta + k\sin\theta\sin\phi)$$

$$\left.+ \cos\phi \sum_{m=1}^{M}(-1)^{m+1}\frac{I_m e^{-j(\beta\ell_m + ks_m \cos\phi\sin\theta)}}{(\beta - k\sin\theta\sin\phi)}\sin\frac{L_m}{2}(\beta - k\sin\theta\sin\phi)\right] \quad \text{(C. 13)}$$

It should be noted that throughout this analysis no restriction has been placed on the magnitude of the current on the spiral (I_n and I_m) except that it must be constant over the length of any individual wire element. Magnitude adjustments may be made between successive wire elements, however, and these adjustments may follow a certain mathematical relationship. A logical choice for this relationship would be a current magnitude which attenuates only slightly until the "radiation region" of the spiral is reached, and thereafter, attenuates at a greater rate. The expression

$$I_m = \frac{I_o}{1 + e^{-a(\ell - \ell_m)}}$$

has these characteristics and was used in computing field patterns.

REFERENCES

1. W. G. James and D. R. J. White, "Digital Computer Simulation for Prediction and Analysis of Electromagnetic Interference," IRE Trans. on Comm. Sys., June 1961, pp. 148-159.

2. J. J. Wolfe and R. Bawer, "Printed-Circuit Spiral Antennas," Electronics, April 1961.

3. J. A. Kaiser, "The Archimedean Two-Wire Spiral Antenna," IRE Trans. on Antennas and Propagation, May 1960, pp. 312-323.

4. W. L. Curtis, "Spiral Antennas," IRE Trans. on Antennas and Propagation, May 1960, pp. 298-306.

5. S. Silver, Microwave Antenna Theory and Design, McGraw-Hill, 1949, pp. 182-192.

6. D. G. Kiely, Dielectric Aerials, John Wiley and Sons, 1953.

7. R. E. Collin, Field Theory of Guided Waves, McGraw-Hill, 1960.

8. G. Hasserjian and A. Ishimaru, "Excitation of a Conducting Cylindrical Surface of Large Radius of Curvature," IRE Trans. on Antennas and Propagation, May 1962, pp. 264-273.

9. D. K. Adams, et. al., "Derivation of Aerospace Antenna Coupling Factor Interference Prediction Techniques," Interim Tech. Rept. No. 4, Cooley Electronics Laboratory, The University of Michigan, Ann Arbor, Mich., April 1963.

10. D. K. Adams, et al., "Derivation of Aerospace Antenna Coupling Factor Interference Prediction Techniques," Interim Tech. Rept. No. 5, Cooley Electronics Laboratory, The University of Michigan, Ann Arbor, Mich., July 1963.

11. D. K. Adams, et al., "Derivation of Aerospace Antenna Coupling Factor Interference Prediction Techniques," Interim Tech. Rept. No. 2, Cooley Electronics Laboratory, The University of Michigan, Ann Arbor, Mich., Sept. 1962.

12. R. F. Harrington, Time Harmonic Electromagnetic Fields, McGraw-Hill, 1961.

DISTRIBUTION LIST

Copies	
5	DDC, Cameron Station, Arlington, Virginia 22314
3	AFAL (AVWE), Wright-Patterson AFB, Ohio 45433
2	AFAL (SEDTE/Charles Seth), Wright-Patterson AFB, Ohio 45433
3	AFAL (AVWE/H. Bartman), Wright-Patterson AFB, Ohio 45433
1	SSD (SSTRG/Capt. R. Eaglet), AF Unit Post Office, Los Angeles, California 90045
1	RTD (RTHC/Lt. Col. A. Blue), Bolling AFB, D C 20332
1	AFEL (RAUMA/C. R. Miller), Griffiss AFB, N. Y. 13442
1	AFEL (RAUMM/Q. S. Porter), Griffiss AFB, N. Y. 13442
3	ECAC (ACD/Ben Lindeman), Annapolis, Md.
1	Hq USAF (AFRST/Maj. Jaffers), Washington, D. C. 20330
1	USAERDL (SELRA/GFI, S. Wertz), Fort Monmouth, N. J.
1	NANEP (NATC/O. D. Stewart), Patuxent River, Md.
1	NASA, Goddard Space Flight Center, Antenna Section, Code 523, Greenbelt, Md.
2	Scientific and Technical Information Facility, Attn: NASA Representative (SAK/DL), P. O. Box 5700, Bethesda, Md. 20014
1	Aero Geo Astro Corporation, Attn: Security Officer, Edsall and Lincolnia Blvd., Alexandria, Virginia
1	Andrew Alfred Consulting Engineers, Attn: Librarian (Antenna Section), 299 Atlantic Avenue, Boston 10, Massachusetts
1	Boeing Airplane Company, Attn: Technical Library, M/F Antenna Systems Staff Unit, 3801 S. Oliver, Wichita, Kansas
1	Boeing Airplane Company, Aero Space Division, Attn: Technical Library, M/F Antenna and Radomes Unit, Seattle, Washington
1	Dorne and Margolin, Inc., Attn: Technical Library (Antenna Section), New York Avenue, Westbury, L. I., N. Y. 11591
1	Hughes Aircraft Corporation, Attn: Technical Library (Antenna Section), Florence and Teal Street, Culver City, California

1	University of Illinois, Attn: Technical Library, (Dept. of Electrical Engineering), Urbana, Illinois
1	Lincoln Laboratories, Massachusetts Institute of Technology, Attn: Document Room, P. O. Box 73, Lexington 73, Massachusetts
1	Ling Temco Aircraft Corporation, Temco Aircraft Division, Attn: Librarian (Antenna Lab), Garland, Texas
1	Ramo-Wooldridge Corporation, Attn: Librarian (Antenna Lab), Canoga Park, California
1	Raytheon Company, Missile and Space Division, Attn: Technical Library (Antenna Section), P. O. Box 636, Santa Barbara, California
1	Texas Instruments, Inc., Attn: Librarian (Antenna Lab), 6000 Lemmon Avenue, Dallas 9, Texas
1	Wheeler Laboratories, Inc., Attn: Librarian (Antenna Lab), Box 561, Smithtown, New York
1	Dr. B. F. Barton, Director, Cooley Electronics Laboratory, The University of Michigan, Ann Arbor, Michigan
20	Cooley Electronics Laboratory, The University of Michigan, Ann Arbor, Michigan